

Alma Mater Studiorum – Università di Bologna

DOTTORATO DI RICERCA IN

## **Geofisica**

Ciclo XXV

**Settore Concorsuale di afferenza:** 04/A4 – GEOFISICA

**Settore Scientifico disciplinare:** GEO/10 – GEOFISICA DELLA TERRA SOLIDA

TITOLO TESI

# **Local Earthquake Tomography by trans-dimensional Monte Carlo Sampling**

**Presentata da:** Genny Giacomuzzi

**Coordinatore Dottorato**

Michele Dragoni

**Relatore**

Andrea Morelli

**Esame finale anno 2013**

# Contents

<b>Introduction</b>	<b>3</b>
<b>1 A new code for Local Earthquake tomography</b>	<b>5</b>
1.1 Local Earthquake tomography . . . . .	5
1.1.1 Toward a fully non-linear LET: state of art . . . . .	6
1.2 Principles of Rj-McMc LET . . . . .	6
1.2.1 Model parameterization . . . . .	6
1.2.2 Forward solution . . . . .	8
1.2.3 The Bayesian approach to inversion problems . . . . .	9
1.2.4 The likelihood function . . . . .	11
1.2.5 The Reversible Jump Markov chain Monte Carlo sampling . . . . .	11
1.2.6 A-priori information on model parameters . . . . .	16
1.2.7 Analysis of the PDF . . . . .	17
1.3 Looking for a suitable recipe for Rj-McMc LET . . . . .	18
1.3.1 The minimum origin-time method . . . . .	22
<b>2 Inversion of synthetic data</b>	<b>29</b>
2.0.2 Synthetic test setup . . . . .	29
2.1 Rj-McMc LET . . . . .	32
2.1.1 Misfit evolution and convergence assessment . . . . .	34
2.1.2 Analyses of marginal PDF and errors estimate accuracy . . . . .	36
2.2 Simulps LET . . . . .	41
2.2.1 Standard linearized approach to LET . . . . .	41
2.2.2 Model parameterization and starting models . . . . .	41
2.2.3 Data misfit and resolution analysis . . . . .	43
2.2.4 Best-fit $V_p$ and $V_p/V_s$ models . . . . .	46

## Contents

2.3	Comparison between Simulps and Rj-McMc results . . . . .	50
2.3.1	Data fitting . . . . .	50
2.3.2	Dependence on parametrization and regularization . . . . .	50
2.3.3	Dependence on starting model . . . . .	52
<b>3</b>	<b>Rj-McMc LET of the Alto Tiberina Fault</b>	<b>55</b>
3.1	Tectonic setting and velocity constraints . . . . .	58
3.2	Rj-McMc tomography . . . . .	60
3.2.1	Seismic data and networks . . . . .	60
3.2.2	Prior information . . . . .	62
3.2.3	RjMcMc sampling of the PDF and data misfit . . . . .	62
3.2.4	Discussion on the $V_p$ and $V_p/V_s$ mean posterior models . . .	65
3.3	Comparison with previous models . . . . .	74
<b>4</b>	<b>Rj-McMc LET at Parkfield</b>	<b>83</b>
4.1	Tectonic setting . . . . .	83
4.2	Rj-McMc tomography . . . . .	88
4.2.1	Seismic data and Networks . . . . .	88
4.2.2	Prior information . . . . .	89
4.2.3	RjMcMc sampling of the PDF and data misfit . . . . .	91
4.2.4	Discussion on the $V_p$ and $V_p/V_s$ mean posterior models . . .	93
4.2.5	Comparison with borehole data . . . . .	103
4.3	Comparison with previous models . . . . .	105
	<b>Conclusions</b>	<b>117</b>
	<b>Acknowledgments</b>	<b>119</b>
	<b>References</b>	<b>120</b>

# Introduction

Local Earthquakes Tomography (LET) is a non-linear inversion problem that allows the joint determination of earthquakes parameters and velocity structure from arrival times of waves generated by local sources.

The non-linearity of the equation that relates the arrival times to velocity and earthquakes parameters arises from the dependence of the ray-paths on both the medium velocity and earthquakes location. Since the early developments of seismic tomography, about 40 years ago, several inversion methods have been developed to solve this problem in a linearized way or by consecutive iterative linearized steps. Of course, in the past, the linear approximation was required by the huge amount of unknown parameters to be estimated if compared to the poor performance of the available computers.

In this PhD dissertation, I describe my contribution to the development of a trans-dimensional Monte Carlo algorithm focused on the LET problem. In the framework of Monte Carlo sampling, we use the Reversible Jump Markov Chain Monte Carlo method (Rj-McMc). It is a trans-dimensional Bayesian (probabilistic) approach of parameters estimation, in which the number of unknowns, and thus the model parameterization, is treated as one of the unknowns. I show that the use of an efficient Monte Carlo sampling algorithm allows overcoming major limitations of linearized tomography, opening a new perspective in seismic imaging.

In linearized tomography, the non-linear equation that relates the arrival times to the model parameters is linearized around a starting reference model. The linearization requires assuming that the sought model is closed enough to the reference starting model. The tomographic images that we obtained are thus dependent on how much the starting reference model is closed to the true. In regions where insufficient a-priori information is available, the linearized approach may produce misleading results. With a fully non-linear approach this problem is clearly overcome.

## *Introduction*

Another factor that causes a loss of information in linearized tomography is the need to regularize the inversion problem in order to deal with the non-uniqueness of the solution. Since both sources and receivers are usually un-evenly distributed in space, the data information content is heterogeneous and the model is characterized by both well and ill-constrained regions. With a model parameterization fixed a-priori, the existence of ill-constraint parameters is the source of solution non-uniqueness and requires some kind of global regularization. The consequence is that a unique “optimum” solution is obtained at the expense of the resolution of the well-constraint regions. If the parametrization is directly extracted from data, the regularization is not required.

Finally, regularization introduces a bias in the estimation of uncertainties about the model parameters. A great advantage of the Bayesian approach is that we obtain a posterior probability density distribution instead of just one “best fit” or “maximum likelihood point” model. For instance, if the marginal probability density is available, we can evaluate how much variation or dispersion there is from the mean value. This provides a powerful tool to derive absolute errors related to the estimated model parameters.

In Chapter 1 I describe the new LET tomographic code developed by Nicola Piana Agostinetti, Alberto Malinverno and me.

In Chapter 2 I highlight the performance of the new code by showing the results of some synthetic tests. More, the results obtained with the new code are compared with those obtained by using Simulps, a linearized tomographic code widely used in Local Earthquake Tomography.

In Chapter 3 and Chapter 4 the new code is applied to real data gathered in the Alto Tiberina region (Umbria-Marche, Italy) and around the Parkfield segment of the San Andreas Fault (California, USA). The two datasets have been chosen because they have already been used to produce velocity models with the Simulps tomographic code, allowing a straightforward comparison with our results. Moreover, in both the places there are boreholes that provide sonic log data to be compared with the velocity models.

# 1 A new code for Local Earthquake tomography

## 1.1 Local Earthquake tomography

Local Earthquake tomography (LET, Kissling, 1988) is a primary “passive” method of imaging the crustal structure. LET allows the joint determination of source parameters and 3D velocity structure by inverting the arrival times of P-waves and S-waves generated by local earthquakes and observed at the stations network.

Following Thurber (1993), in agreement with the ray-theory, the body-wave travel time  $T_{ij}$  from a source  $i$  to a station  $j$  can be computed by integrating the velocity field ( $v$ ) along the ray-path ( $\gamma_{ij}$ ):

$$T_{ij} = \int_{\gamma_{ij}} \frac{1}{\mathbf{v}(\mathbf{s})} ds \quad (1.1)$$

The observed arrival times ( $t_{ij}$ ) can be related to the travel times ( $T_{ij}$ ) by knowing the earthquake origin time ( $\tau_i$ ):

$$t_{ij} = \tau_i + T_{ij} \quad (1.2)$$

The unknown model parameters in the equations 1.1 and 1.2 are the velocity field ( $\mathbf{v}$ ) and the earthquakes coordinates and origin times ( $\tau_i$ ). The observed data are the arrival times  $t_{ij}$ . The LET problem is then highly non linear because of the dependence of the ray-path  $\gamma_{ij}$  on both the velocity field and the earthquake locations. Given the velocity field, the stations coordinates and the earthquakes coordinates, the ray-tracing algorithm allows solving numerically the integral in equation 1.1 and to calculate ray-paths and travel times.

### 1.1.1 Toward a fully non-linear LET: state of art

Being the LET problem highly non-linear, Monte Carlo simulations are suitable to overcome major drawbacks related to the linear approximation. The number of model parameters to be estimated in a seismic tomography investigation is huge and performing a Monte Carlo simulation may require a lot of time. Nevertheless, there are fast algorithms, such as the Markov Chain sampling (e.g., Mosegard and Tarantola 1995), which allow a smart and fast sampling of the parameter space. More, the computation resources have been highly improved in the past decades, after the implementation of the linearized LET inversion codes.

Up to date, the Markov Chain Monte Carlo sampling method (MCMC) has been successfully applied to seismic tomography by Bodin and Sambridge (2009), Bodin et al. (2012) and by Debski (2010). Bodin and Sambridge focused on the 2D problem of surface wave tomography, introducing in the more recent version of the code, the possibility to invert also for the noise in the data. More, the sampling procedure is trans-dimensional: an ensemble of Voronoi's cells whose number and positions are treated as unknown parameterizes the velocity structure. Debski (2010) represents the first application of this sampling method to a simplified LET problem. It is a simplified LET problem because the earthquake locations and origin times are not considered as unknown parameters. Moreover, the parameterization is fixed and mirrors that used in standard linearized tomography.

In the follow I describe the new algorithm, designed by Nicola Piana Agostinetti, Alberto Malinverno and me. Differently from the Debski's code, our new code solves the full LET problem and allows the appropriate model parameterization to be directly extracted from data, instead of being a-priori fixed.

## 1.2 Principles of Rj-McMc LET

### 1.2.1 Model parameterization

An important drawback of the LET is the non-uniform earthquakes distribution that causes a strong variability in the model sampling. Fine-scale resolution is potentially high in regions with dense ray coverage but rather low in other regions. Therefore,

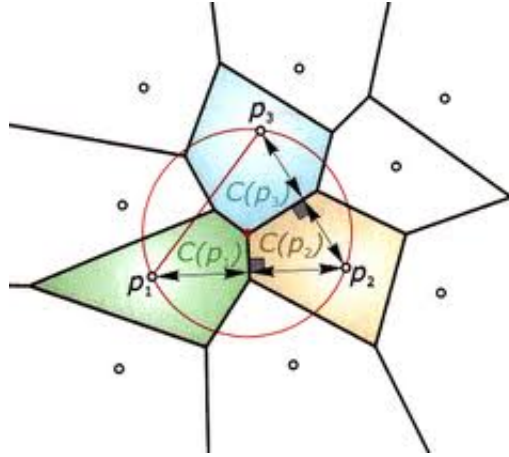


Figure 1.1: Example of Voronoi's 2D tessellation.  $p_1$ ,  $p_2$  and  $p_3$  are the nuclei of the three cells highlighted by colors. The bisectors define the cells boundaries. Each cell encloses all the points that are closer to its nucleus and has a constant velocity value.

an appropriate parameterization should account for the spatial variability in the information provided by the data.

Many available LET codes use regular grids fixed in advance because of the computational efficiency. Seismic velocity is then inverted in correspondence to each of the grid nodes. The drawback of this method is that an appropriate choice of the inter-nodal spacing is essential because it yields the compromise between model resolution and model uncertainties. The wider is the grid spacing, the lower will be the model resolution and smaller the model uncertainties. By reducing the grid-spacing, the model resolution is potentially higher but the data uncertainties led to greater uncertainties in the model parameters and the solution becomes quickly non-unique. In this situation a kind of regularization is required to solve the non-uniqueness of the solution. It is worthy to note that the regularization is global, i.e. it affects uniformly all the parameters, with the consequence that the resolution of well-constrained parameters will be partially lowered together with that of the ill-constrained parameters. More, the estimate of model parameters uncertainties is biased by the regularization. In both the strategies, i.e., by increasing the grid-spacing or by applying regularization, the outcomes are a loss of data information and a biased estimate of uncertainties of model parameters.

In order to deal with this problem, some seismologists have used irregular meshes adapted to the resolving power of data (see Sambridge and Rawlinson 2005 and references therein). Zhang and Thurber (2005) proposed the use of Voronoi' cells for LET tomography but with a parameterization fixed in advance and not directly extracted and determined by data.

Conversely, we follow the strategy by Bodin and Sambridge (2009a,b) to parameterize the 3D velocity structure by an ensemble of non-overlapping Voronoi's cells (Okabe et al., 1992) whose number and spatial locations are treated as unknown parameters. Each Voronoi's cell is defined by the position of its nucleus and it is characterized by a constant value of P-wave velocity ( $V_p$ ) and  $V_p/V_s$  ratio. Perpendicular bisectors of each pair of neighboring nuclei form the cell boundaries (Figure 1.2.1). Each of the  $N$  cells is then defined by 5 unknown model parameters: the three space coordinates and the  $V_p$  and  $V_p/V_s$  values. The algorithm described by Sambridge et al. (1995) is used for the geometrical calculation of the Voronoi's tessellation.

Summing up the earthquake parameters (the three space coordinates and the origin times of  $M$  earthquakes), the total number of model parameters to be estimated amount to  $5N + 4M + 1$ .

More, the code allows treating some earthquake as shots or blasts, i.e. events with known source parameters or with known source location but unknown origin time. This can be suitable when arrival time data derived from "active" seismic experiments, such as refraction seismology or borehole explosions, are available.

## 1.2.2 Forward solution

In our code we employ the pseudo-bending ray-tracing algorithm (Um and Thurber, 1987). The algorithm allows the computation of travel times and ray paths in a 3D heterogeneous medium, by applying the high-frequency approximation of the ray theory (Cerveny and Brown, 2003). The computation is performed in a Cartesian coordinates system with units in km. The velocity model is defined by the intersection points of 3 sets of orthogonal planes positioned at constant values of  $x,y,z$ . Then, the forward computation requires a rasterization of the Voronoi's tessellation on this regular grid. At each of the intersection points of the regular grid the  $V_p$  and

Vp/Vs values of the corresponding Voronoi's cell are associated. Then, the tri-linear interpolation is used to find the velocity value along each segment of the ray path.

### 1.2.3 The Bayesian approach to inversion problems

The Bayesian approach has been successfully applied to geophysical investigations (see Tarantola and Valette, 1982); Mosegard and Tarantol, 1995). In the Bayesian (or probabilistic) approach all information are represented by probability density functions. The solution of the LET problem is then the a posteriori probability distribution (or posterior density function PDF, Smith, 1991), which is the probability density of the model parameters ( $\mathbf{m}$ ) given the observed data ( $\mathbf{d}_{obs}$ ). The PDF, function of the unknown model parameters, is taken as the complete solution of the inversion problem. The PDF ( $p(\mathbf{m} | \mathbf{d}_{obs})$ ) can be defined by the Bayes' theorem (Bayes, 1763). Written in terms of proportionality relationship:

$$p(\mathbf{m} | \mathbf{d}_{obs}) \propto p(\mathbf{d}_{obs} | \mathbf{m})p(\mathbf{m}) \quad (1.3)$$

The probability density function  $p(\mathbf{m})$  describes the a-priori information about model parameters. This probabilistic representation of our a-prior knowledge about model parameters, that is independent from the measured data, has the advantage of include also the uncertainties. In the particular case in which the observed data provide no information about the model parameters, the posterior coincides with the prior density function. Otherwise, the PDF represents how our a-priori information about model parameters is updated by the new measured data (see Figure 1.2).

The probability density function  $p(\mathbf{d}_{obs} | \mathbf{m})$  is the likelihood function that describes the probability of observing the measured data given a particular model. It is notable that the probabilistic approach includes an appropriate treatment of the uncertainties related to the model parameters, allowing an exhaustive error analysis. Our "solution" is not just a single model, but an ensemble of models distributed according to the PDF. Conversely, with the optimization approach used in standard linearized tomography, the solution of the damped least square inversion problem is a single best-fitting likelihood model.

Once the PDF is obtained, it is straightforward to derive properties and estimators such as mean or median values of individual parameters and the associated errors.

This is achieved by constructing 1D marginal probability functions, i.e., the density function obtained by integrating out all but one parameter from the PDF. The correlation between parameters can be assessed in a similar way by constructing multidimensional marginal PDFs.

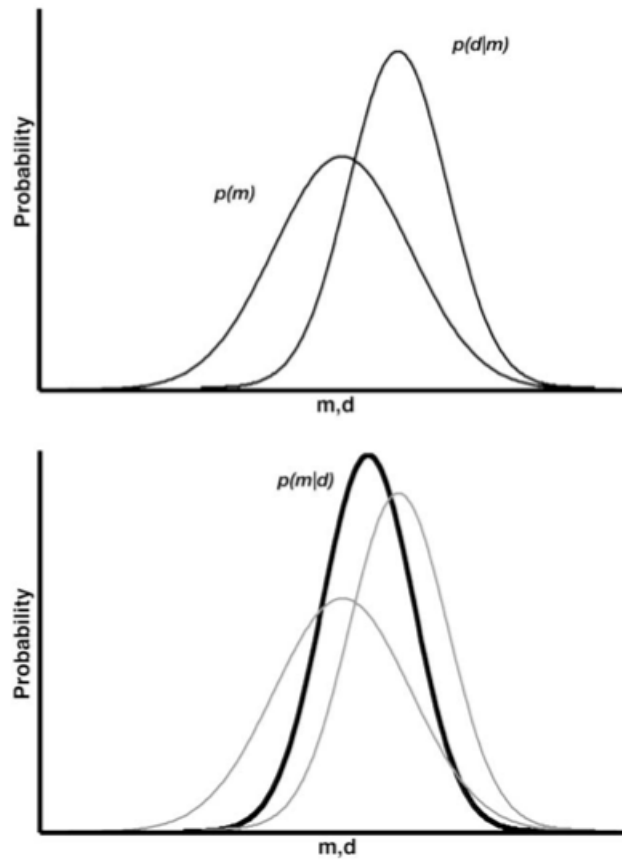


Figure 1.2: Simplified relationship between the prior  $p(\mathbf{m})$ , the likelihood  $p(\mathbf{d} | \mathbf{m})$  and the posterior  $p(\mathbf{m} | \mathbf{d})$  probability density functions. In this case the maximum probability models in the prior and in the posterior differ. The likelihood is the function that allows updating the prior to the posterior (modified from Gallagher et al., 2009).

### 1.2.4 The likelihood function

We use a likelihood based on a simple least squares misfit:

$$\phi(\mathbf{m}) = (\mathbf{d} - g(\mathbf{m}))^T \mathbf{C}_d^{-1} (\mathbf{d} - g(\mathbf{m})) \Rightarrow p(\mathbf{d}_{obs} | \mathbf{m}) = \frac{1}{2\pi^N |\mathbf{C}_d|^{1/2}} e^{-\frac{\phi(\mathbf{m})}{2}} \quad (1.4)$$

where  $g(\mathbf{m})$  is the calculated data,  $\mathbf{d}$  the observed data vector of dimension  $N$  and  $\mathbf{C}_d$  the data covariance matrix.

### 1.2.5 The Reversible Jump Markov chain Monte Carlo sampling

The PDF cannot be expressed in an analytical form and then must be evaluate at different positions in the model space. More, a global search is not possible in the case of seismic tomography because of the huge amount of parameters to be estimated. The Markov chain Monte Carlo (McMc) sampling method allows overcoming these problems. The McMc is one of the more flexible and popular sampling algorithms to generate samples of the PDF (see Sisson, 2005 for a review; Gallagher et al. 2009). It is based on a short memory random walk to produce a sequence of models from the model space. Along the random walk, the new generated model is conditional to the previous one but independent of how the previous model was arrived at. It uses a stochastic approach to efficiently and preferentially sample regions of the model space characterized by a high value of the target PDF. This method was first applied in the geophysical problems by Malinverno and Leaney, (2000; 2005).

The generation of sample of the PDF occurs in this way (see Figure 1.3):

1. The Markov chain starts from a random model sampled from the prior distribution and it is considered as the first current model ( $\mathbf{m}$ ).
2. A candidate model ( $\mathbf{m}'$ ) is drawn by perturbing the current model according to a proposal probability distribution ( $q(\mathbf{m}' | \mathbf{m})$ ) that only depends on the current model. It described the probability of having  $\mathbf{m}'$  when  $\mathbf{m}$  is fixed.

### Chart flow of a Markov chain

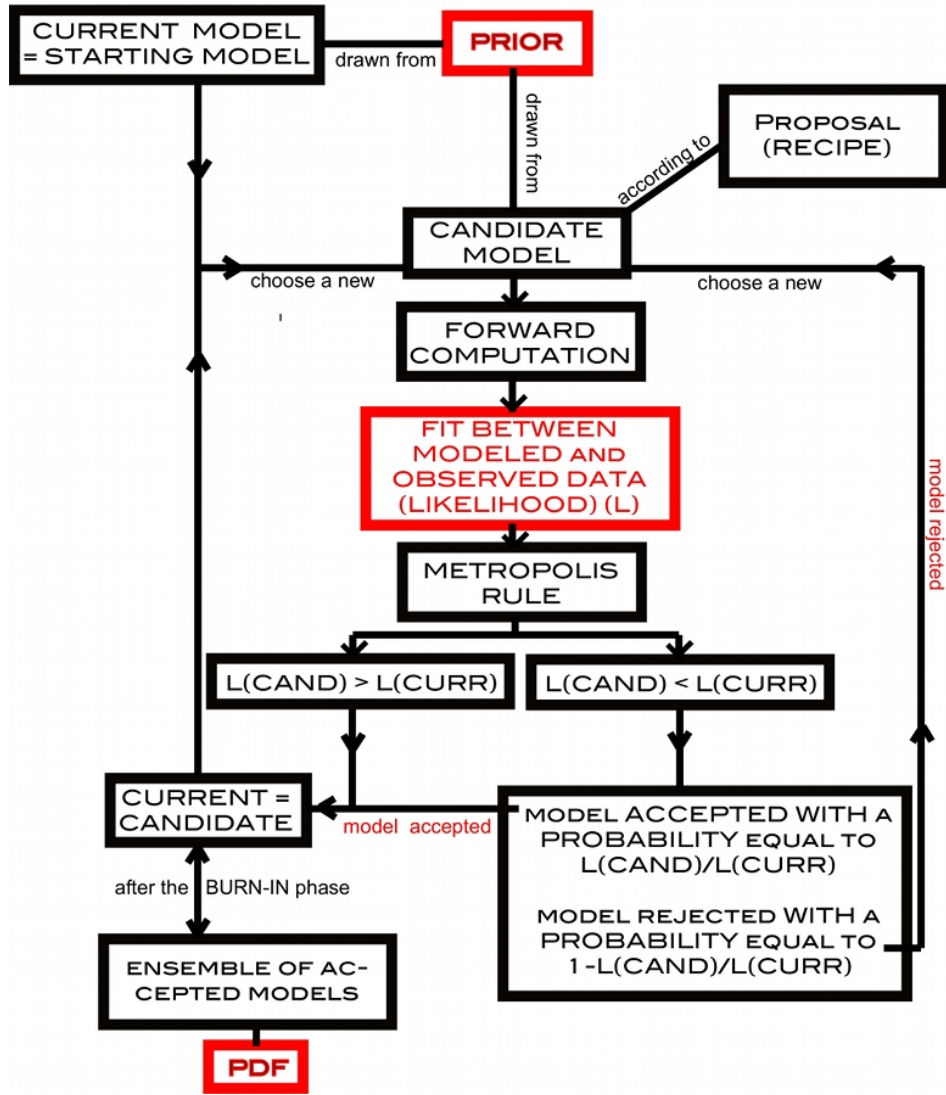


Figure 1.3: Simplified chart flow of the Markov Chain sampling

In other words, the proposal distribution states which parameter is perturbed and in which way. It is worthy to note that it is arbitrary, that is, it doesn't affect the form of the target PDF distribution at which the algorithm will converge. Nevertheless, it controls the time required by the Markov chain to reach the convergence state.

3. The arrival times are determined in the current and candidate models using the pseudo-bending ray tracing code, allowing the computation of the likelihood function given by the equation 1.4.
4. An extension of the well-known Metropolis-Hasting algorithm (Metropolis et al., 1953; Hastings, 1970; Green, 1995) is then applied in order to accept or reject the candidate model. The Metropolis-Hasting algorithm has been extended by Green (1995; 2003) to account for the transition between states (i.e. models) with a different number of dimensions. In this way, the Reversible Jump McMc sampling method (Rj-McMc) allows inferences of both model parameters and model dimensionality. The probability to accept a candidate model  $\alpha(m' | m)$  depends on the ratio between the prior density functions, the proposal density functions and the likelihood functions of the candidate and current models (Gallagher et al., 2009):

$$\alpha(\mathbf{m}' | \mathbf{m}) = \min \left[ 1, \frac{p(\mathbf{m}')}{p(\mathbf{m})} \times \frac{p(\mathbf{d}_{obs} | \mathbf{m}')}{p(\mathbf{d}_{obs} | \mathbf{m})} \times \frac{q(\mathbf{m} | \mathbf{m}')}{q(\mathbf{m}' | \mathbf{m})} \times |\mathbf{J}| \right] \quad (1.5)$$

The matrix  $J$  is the Jacobian of the transformation from  $\mathbf{m}$  to  $\mathbf{m}'$ . In our case it is equal to 1, as demonstrated by Bodin and Sambridge (2009b), and can be ignored (see also Piana Agostinetti and Malinverno, 2010). Following the sampling strategy of Mosegaard and Tarantola (1995), the proposal distribution equals the prior distribution and the acceptance probability reduces to the ratio of the likelihood functions:

$$\alpha(\mathbf{m}' | \mathbf{m}) = \min \left[ 1, \frac{p(\mathbf{d}_{obs} | \mathbf{m}')}{p(\mathbf{d}_{obs} | \mathbf{m})} \right] \quad (1.6)$$

Then, after proposing a candidate model, it is only required to compute the travel times in the candidate model and calculate the ratio of the likelihood functions. The candidate model is accepted if  $\alpha(\mathbf{m}' | \mathbf{m}) \geq r$ , with  $r$  a random number generated from a uniform distribution between 0 and 1. According to this criterion, a candidate model will be always accepted if its likelihood is higher than that of the current model and it will be accepted with the probability  $\alpha(\mathbf{m}' | \mathbf{m})$  if its likelihood is lower.

It has been demonstrated that models generated along the Markov chain according to the probability  $\alpha(\mathbf{m}' | \mathbf{m})$  will converge to the target transdimensional posterior distribution (see Green, 2003; Tierney, 1994). As noted by several authors (e.g., Bodin and Sambridge, 2009; Malinverno, 2000), the trans-dimensional acceptance probability reveals the self-regularizing property of the Bayesian approach, which always favors the simpler model when two models have roughly the same likelihood function.

5. If the candidate model is accepted, it becomes the current one and the chain moves to the next step ( $\rightarrow 6. \rightarrow 2.$ ). If the candidate model is rejected, the current model is retained and another candidate model is drawn from it ( $\rightarrow 2.$ ).
  
6. Models generated and accepted in the first part of the chain (named burn-in phase) are then not collected until the chain reaches a stationary state. Then, all the accepted and collected models can be considered as individual samples of the target PDF. The assessment of stationarity is subject of ongoing research and a general, well-accepted, rule for the Rj-McMc sampling is still lacking (e.g., Sisson, 2005). Bodin and Sambridge, (2009b) consider the stationary state to be achieved when the velocity value at a given point or the model dimension remain stationary. We prefer to look also at the misfit evolution. We start to collect samples of the PDF when the misfit becomes stationary. It is notable that at this stage, the number of models accepted because of a decrease in the data misfit is similar to the number of models accepted because of an increase in the data misfit.

**Simulated annealing burn-in** In order to shortening the burn-in phase and start to collect samples of the PDF, we use a method derived from the simulated annealing optimization scheme (Vinnik et al., 2004). The acceptance probability  $\alpha$  is greater in the first part of the chain and decays exponentially to the value of 1 used in the standard Metropolis rule. The user must set the starting “temperature” of the simulated annealing ( $T_o$ ) and the decay rate ( $K_S$ ) (Figure 1.4):

$$\alpha(\mathbf{m}' | \mathbf{m}) \propto \begin{cases} e^{-\frac{1}{2}(\phi(\mathbf{m}')-\phi(\mathbf{m}))} & \text{if } i_m > K \text{ post burn-in phase} \\ e^{-\frac{1}{2} \frac{(\phi(\mathbf{m}')-\phi(\mathbf{m}))}{fact}} & \text{if } i_m \leq K \text{ burn-in phase} \end{cases} \quad (1.7)$$

$$fact = 1 + T_o \exp \left\{ \frac{-i_m}{K_S} \right\} \quad (1.8)$$

where  $i_m$  is the number of already generated models,  $K$  is the total number of generated models for which the simulated annealing is applied.

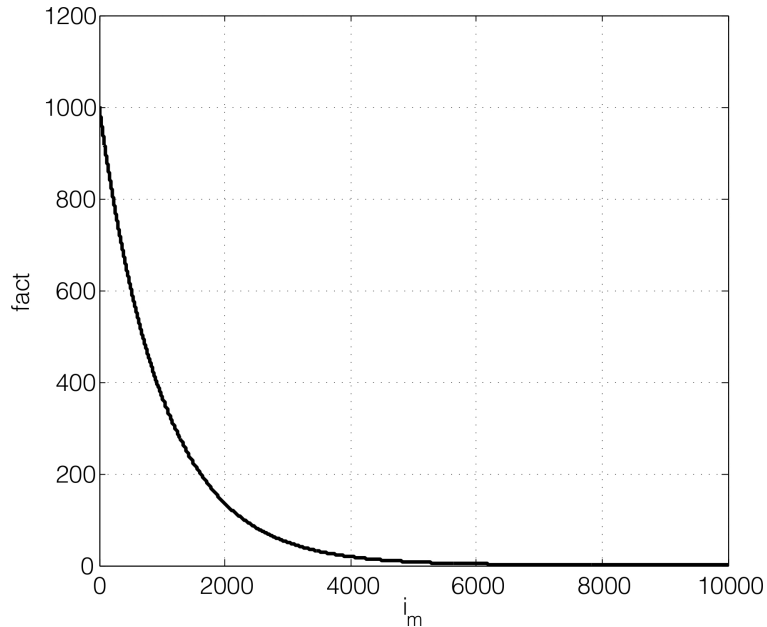


Figure 1.4: Example of decaying temperature computed with  $T_o = 1000$  and  $K_s = 1000$ .

**Multiple chains and starting models** To sample a higher region of the model space, we don't use a single Markov chains but many chains (usually 20) starting in different points of the model space. Each chain starts with a different number of Voronoi's cells (extracted from a uniform prior distribution) with different velocity and different values of earthquakes coordinates. When each chain reaches the stationary state, the collected samples are merged together. During the collection of models, each chain is thinned, that is, only every 10th or 100th models are retained.

### 1.2.6 A-priori information on model parameters

In the Bayesian approach, our a-priori knowledge about model parameters must be expressed as probability distributions. Here, I describe the prior functions related to each of the unknown model parameters used in our Rj-McMc LET code.

- Number  $n$  of Voronoi's partition: we use a uniform continuous prior distribution over the interval  $I = \{1 \leq n \leq N\}$ , with  $N$  chosen by the user.
- Position of the nuclei of the Voronoi's cells: we use a uniform prior distribution for each of the nucleus coordinates  $c_i^{nuc}$  ( $i = 1, 2, 3$ ) over the interval  $I = \{c_i^{nuc} \in R \mid 0 \leq c_i^{nuc} \leq 1\}$ . The coordinate system is then a-dimensional.
- Elastic parameters: a prior Gaussian distribution is defined for both  $V_p$  and  $V_p/V_s$  values at each node of the regular grid used for the forward computation. In this way, the prior distribution on the  $V_p$  or  $V_p/V_s$  of a Voronoi's cell corresponds to the prior distribution of the nearest node of the regular grid. With the normal distribution, the user must assign mean values ( $\bar{v}_1, \bar{v}_2$ ) and standard deviations ( $\sigma_1, \sigma_2$ ) of the distributions at each of the nodes of the regular grid.
- Events parameters: a prior 3D Gaussian distribution is defined for each event. Similar to the elastic parameters, the user must define mean and standard deviation values for each coordinate of each earthquake. A uniform prior distribution is instead associated to event origin time. The boundaries of the distribution must be set by the user.

### 1.2.7 Analysis of the PDF

Once the convergence has been achieved, the collected models represent an ensemble of models distributed according to the PDF. Due to the huge amount of estimated parameters, the analysis of the whole PDF is extremely difficult. We then analyze the 1D marginal PDF, that is, the probability distribution obtained by integrating out all but one parameter from the PDF. The numerical evaluation of the marginal PDF corresponds to a frequency distribution. For example, the mean posterior value of the parameter  $m_i$  can be estimated as:

$$\bar{m}_i = \frac{1}{N_s} \sum_j^{N_s} m_i^j \quad (1.9)$$

where  $N_s$  is the number of collected samples.

After checking that the marginal PDF is unimodal, a suitable representation of the tomographic results can be achieved by computing mean and standard deviation values of the marginal PDF for each of the parameters. Since the models don't have the same dimension, each Voronoi's tessellation is rasterized on the underground regular grid. Then, the mean Vp and Vp/Vs values, together with the associated standard deviations, can be computed at each point of the regular grid and imaged using standard tomographic horizontal or vertical cross-sections. The basic difference is that we show a velocity model that is averaged over a huge amount of models (generally some millions) and provide also tomograms of unbiased uncertainties associated to the velocity structure. Conversely, tomograms obtained from traditional linearized tomography show one single model and the uncertainties are biased by the regularization required to solve the inversion problem. The same can be said for the earthquake locations.

### 1.3 Looking for a suitable recipe for Rj-McMc LET

Along the Markov chain, the new candidate model is drawn from the current model according to the proposal distribution (Figure 1.5). It is worthy to note that the proposal distribution is arbitrary, that is, it doesn't affect the form of the target PDF distribution at which the algorithm will converge. Nevertheless, it controls the time required by the Markov chain to reach the convergence state.

As noted by many authors (e.g., Malinverno, 2002; Mosegard and Tarantola, 1995; Piana Agostinetti and Malinverno, 2010), numerical experiments are needed to choose a recipe suitable for a particular inverse problem. The search of an appropriate recipe to apply to the LET inversion problem has been carried out with a trial and error strategy that is, by looking at the different convergence rate and acceptance ratio (the ratio between the number of accepted models and the number of proposed models) when different recipes are applied.

We call "move" a specific type of transition between model  $m$  and model  $m'$  along the Markov chain. A certain probability to occur is assigned to each move. The probability of each move must be set by the user, together with the parameters and the scale factors that define how much a certain parameter is perturbed in the transition from the current to the candidate model. In the case that the current and the candidate models have the same number of dimensions, the proposal is a multi-dimension Gaussian distribution centered on the current model and with a diagonal covariance matrix  $\mathbf{C} = \text{diag}(\sigma_i^2)$ . The user must define the variances  $\sigma_i^2$  of the proposal distribution for each model parameter (typically a small fraction of the variance of the prior distribution).

To generate a candidate model  $\mathbf{m}'$  from the current model  $\mathbf{m}$ , the  $i$ th component of  $\mathbf{m}$  is perturbed by drawing a random variable  $u$  from a normal distribution  $N(0, 1)$  and setting  $\mathbf{m}' = \mathbf{m} + u\sigma_i\mathbf{e}_i$ , where  $\mathbf{e}_i$  is the unit vector in the  $i$ th direction and  $\sigma_i$  is the variance of the proposal for the  $i$ th parameter. The  $i$ th parameter can be the Vp or Vp/Vs value of a Voronoi's cell, a coordinate of an earthquake, or a coordinate of a nucleus of one of the Voronoi's cells. If many parameters are perturbed simultaneously the proposal takes the form:

$$q(\mathbf{m}' | \mathbf{m}) \propto \exp \left\{ -\frac{1}{2}(\mathbf{m} - \mathbf{m}')^T \mathbf{C}^{-1}(\mathbf{m} - \mathbf{m}') \right\} \quad (1.10)$$

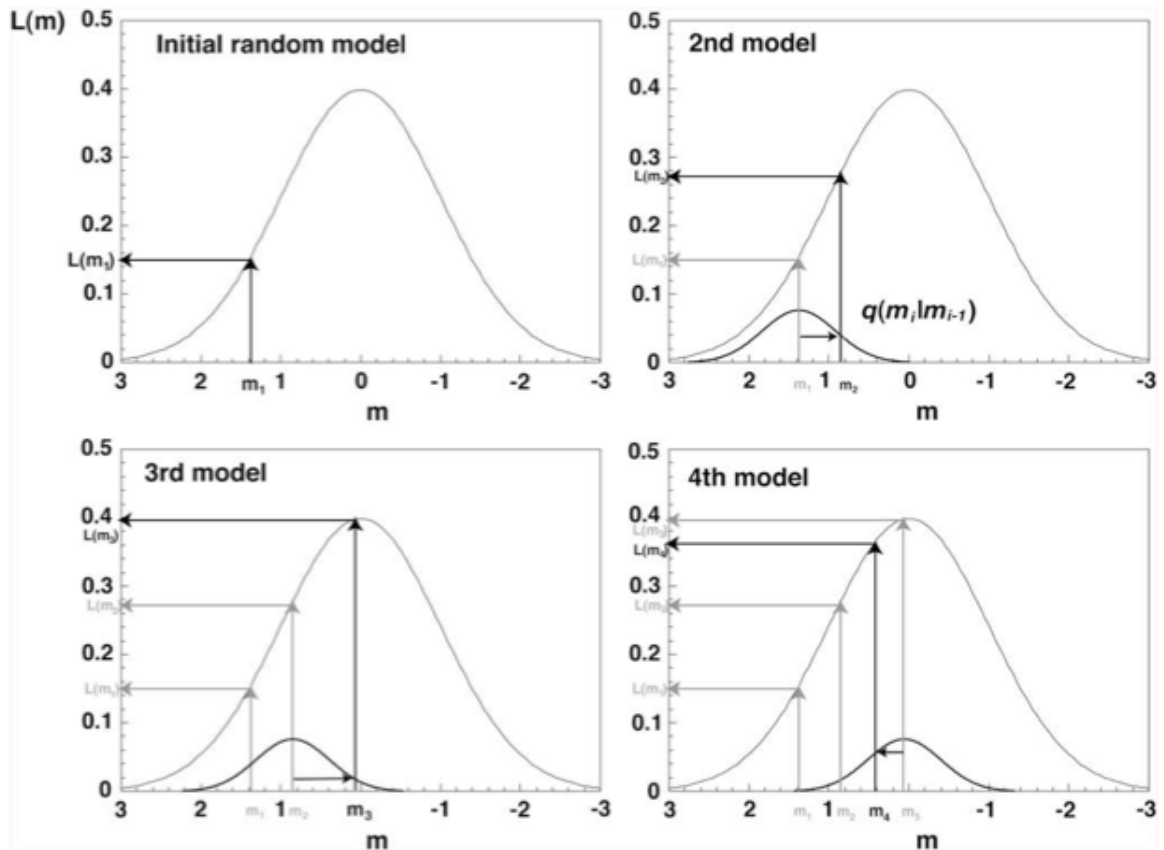


Figure 1.5: Implementation of the proposal density function. The initial random model is drawn from the prior distribution (vertical arrow) and its likelihood value can be computed ( $Lm_1$ ). The likelihood function is marked by the thin line. The candidate model is drawn from the proposal distribution  $q(m_i | m_{i-1})$ , that is a Gaussian distribution centered on  $m_{i-1}$ . The wideness of the proposal distribution is defined by the user and determines the amplitude of the move from the current model (modified from Gallagher et al., 2009).

When the transition between  $\mathbf{m}$  and  $\mathbf{m}'$  involves the creation of a new Voronoi's cell, the values of the two elastic parameters  $V_p$  and  $V_p/V_s$  are associated to the new cell by perturbing the elastic parameters that exist in the same position in the current model. Otherwise, the code allows drawing the new elastic parameters of the newly generated cell directly from the prior distribution.

The criteria according to which I chose the appropriate recipe are the following:

- The amount of perturbation of each parameter shouldn't be too strong or too weak. If a perturbation is too strong, the probability of the candidate model to be accepted will be very low because the perturbation causes a strong variation in the likelihood of the candidate model with respect to the current model. A strong move may then become extremely inefficient. Conversely, if the move is too weak, the acceptance rate will be high but the sampling of the parameters will be very slow and then computationally expensive. Note that in both the extreme cases the convergence will be strongly inhibited (Hopcroft et al., 2007). The user understand that a move is too strong or too weak looking at the acceptance ratio (the ratio between the number of accepted models and the number of proposed models for the given move). Experience has shown that the acceptance ratio should be in the range 0.25-0.5 (Mosegaard, 2006) or even less in the trans-dimensional sampling (Rosenthal, 2009, Piana Agostinetti and Malinverno, 2010).
- The probability of the moves should be as much as possible balanced in order that all parameters reach the convergence in a similar time. The probability associated to each move cannot be too low because the sampling of the parameters involved in the move will be too slow. In the case of the LET inversion problem, if the probability to perturb parameters related to the velocity structure is much higher than the probability to perturb the earthquakes hypocenters, the Rj-McMc sampling will reach a state in which the velocity structure is well sampled while the events locations are very poorly sampled. At this state, the achievement of a stationary state in the misfit evolution will be very slow, because the probability to perturb the earthquakes is still very low. More, in the case of LET problems, a well-known trade-off exists between velocity, earthquake locations and origin times. This kind of trade-off,

together with an unbalanced sampling of velocity and earthquakes parameters may guide and trap the sampling into a local minimum.

- It is preferable that a move don't involve perturbation of parameters characterized by a strong difference in affecting the likelihood function. If, for instance, I perturb both an earthquake hypocenter and the velocity of a Voronoi's cell, the perturbation of the earthquake generally has a greater effect on the predicted travel times than the perturbation of one cell. Then, the stronger perturbation hides in some way the weaker one. On the contrary, some parameters may be grouped together and updated in a block, especially when it is easy to design a proper multi-parameters proposal distribution (for example perturbing together the three spatial coordinates of the nucleus of a Voronoi's cell).

On the base of these criteria, given a current model  $\mathbf{m}$ , the generation of a new model  $\mathbf{m}'$  occurs by one of the following moves:

1. ELASTIC PARAMETER move: perturb the  $V_p$  and  $V_p/V_s$  values of one Voronoi's cell every 100 cells existing in the current model. The cells to be perturbed are randomly selected.
2. NUCLEUS move: perturb the three space coordinates of one Voronoi's cell. In this case the move involves the perturbation of three parameters.
3. BIRTH move: randomly select free points in the space and create up to 5 new Voronoi's cells. The number of newly created cells is randomly selected from a uniform distribution in between 1-5.  $V_p$  and  $V_p/V_s$  values are associated to the new cells by perturbing the elastic parameters that are present in the same locations of the current model. The position of the newly created nucleus is randomly selected using a uniform continuous distribution over the region of the model. Once a nucleus with a new position is proposed for a candidate model, the code checks if the new nucleus is too near to the nuclei that already exist in the current model. The minimum distance between two nuclei is locally defined by the inter-nodal spacing of the underground regular grid.
4. DEATH move: randomly select up to 5 Voronoi's cells and delete them.

5. EVENT epicenter move: perturb the latitude and longitude of one earthquake.
6. EVENT depth move: perturb the depth of one earthquake.

Moves 3. and 4. involve a change in model dimension. The best origin times of the earthquakes are estimated independently for each one of the candidate models. The reason will be discussed at the end of this chapter.

### 1.3.1 The minimum origin-time method

I performed many synthetic tests in order to tune the code and make it suitable for the LET inversion problem. The synthetic test described here represents an extreme case but it is also substantial for understanding how much one must be careful in designing the optimal recipe of sampling for the particular inversion problem. Further synthetic tests are shown in the next chapter.

A well-known trade-off exists in the LET inversion problem between velocity and event parameters, especially event depth and origin time. As previously noted, if the sampling of the events parameters is not well balanced against the sampling of elastic parameters, the sampling may be trapped in a local minimum of the complex-shaped misfit function. In other words, what happens is that the improvement in data-fit is achieved preferentially by changing the velocity values instead of the event locations.

To test this hypothesis, I properly designed a simple synthetic test to evaluate the effect of the trade-off between the event parameters and the elastic parameters. I created a synthetic model (Figure 1.6a), with 6 events and a simple 1D  $V_p$  structure. After adding some noise to the predicted synthetic data, I used them as input-data for the rj-McMc LET tomography.

The prior information is summarized in Figure 1.6b. At each point of the background grid, the prior distribution is a normal distribution with the mean value corresponding to the  $V_p$  at the considered depth and with standard deviation equals to 0.5 km/s. Note that, in this case, the mean values of the prior distribution of the  $V_p$  parameters are the same  $V_p$  values given in the input structure. This is not the case for the hypocentral depths that are 2.5 km deeper than in the synthetic structure. The standard deviation of the prior for the earthquakes depth amounts to 2 km.

The prior normal distribution for both the elastic parameters and the earthquake parameters are sampled in the range  $\pm 4\sigma$ .

We run 10 Markov chains, starting from random models drawn from the prior distribution. The recipe of sampling is that described in the previous section, except for the origin time that it is sampled together with the earthquake depth in MOVE n. 6. The convergence has been achieved after about 300000 models (see Figure 1.7). The following 100000 models are considered as samples of the PDF. Figure 1.7c shows the mean  $V_p$  value of the 1D marginal PDF at each node of the background grid. The recovered structure is far from similar to the input synthetic velocity structure. More, the earthquake locations are very similar to the mean values of the prior, testifying that the misfit decrease shown in Figure 1.7 is accomplished by an almost pure adjustment of the velocity parameters.

To overcome this problem, following Billings et al. (1994), we separate the sampling of the event spatial coordinates from the sampling of the origin time and compute the optimum origin time of all the events for each candidate model. In other words, independently from the type of transition between the current and candidate model (i.e., the type of MOVE), the origin time of all the events are perturbed in order to obtain the set of origin times that minimize the misfit function. All the other settings of the Rj-McMc are kept identical to the previous test.

In this way the correct estimate of the event depth and velocity structure can be easily achieved (Figure 1.7d). This happens because the independent estimate of the origin time allows the sampling to jump outside from the local minima of the misfit function. In the case that the misfit reduction has been achieved by a variation in the velocity, as in our case, if we propose a candidate model by keeping fixed the origin time and perturbing the event depth, the probability of the candidate model to be accepted will be very low even if the candidate event depth approaches its real value. Conversely, if we perturb the event depth and at the same time allow the origin time to change, the probability of the candidate model to be accepted will be higher, as such as the probability to jump outside from the misfit local minimum (see Figure 1.8).

In Figures 1.9 and 1.10, I show posterior mean and standard deviation values for two earthquakes depth and two nodes of the  $V_p$  model. The posterior values are obtained from the first 200000 accepted models, i.e. during the burn-in phase of the

parameter sampling. Therefore, these models shouldn't be considered as individual samples of the PDF but their analysis is useful to understand what happens during the sampling of the parameter space without or with the application of the method by Billings et al. (1994). In the two cases, the sampling starts in the same region of the model space (the first generated models are identical). Then, the misfit reduction in the first case is achieved by a fast increase in  $V_p$  values, instead of a deepening of the earthquake depth. Once this situation is established, there is no way for the sampling to escape the local minimum of the misfit function. It is worthy to note that the standard deviations related to the earthquakes depth are low, especially for events n. 2, highlighting the existence of a narrow local minimum. In the second case, the continuous change of the origin time allows both the velocity and earthquakes to be correctly recovered.

### 1.3 Looking for a suitable recipe for Rj-McMc LET

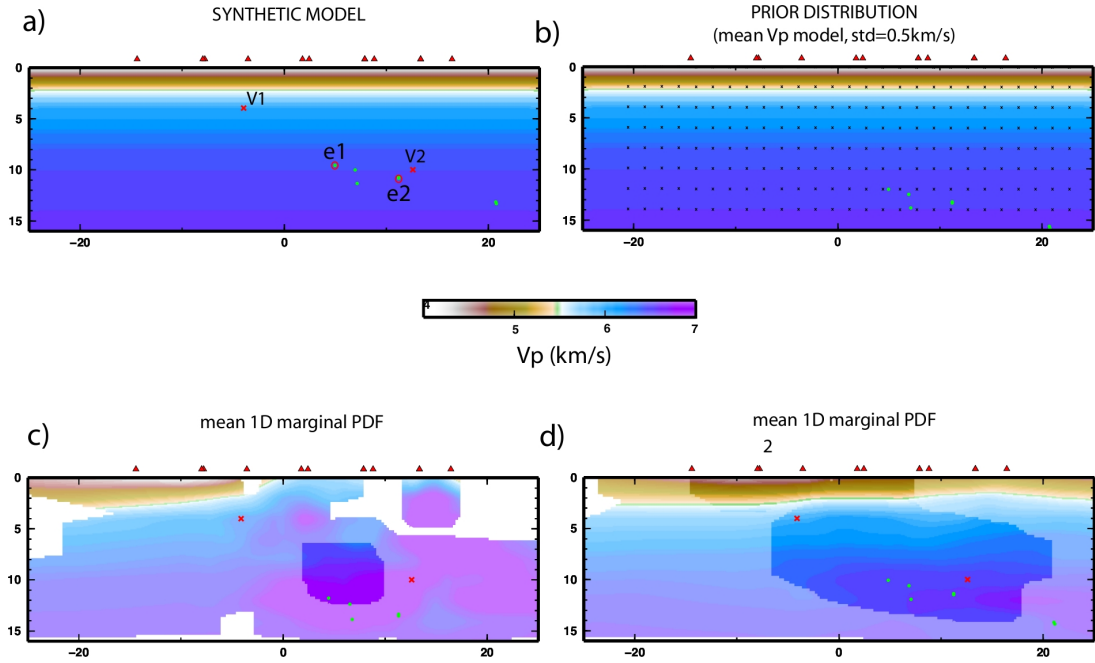


Figure 1.6: a) Synthetic Vp model shown on a vertical 2D cross-section. b) Mean values of the prior distributions for both Vp and earthquake locations. Black crosses represent the nodes of the background regular grid at which prior and posterior distributions for the elastic parameters are calculated. c-d) mean values of 1D marginal PDFs of both Vp and earthquake locations before (c) and after (d) the implementation of the optimum origin time method. Full-color areas correspond to model regions where the posterior standard deviation is less than half of the prior standard deviation. Green dots mark the location of the 6 earthquakes. Red symbols mark the parameters described in the text (red crosses mark Vp at two points of the model and red circles two earthquakes).

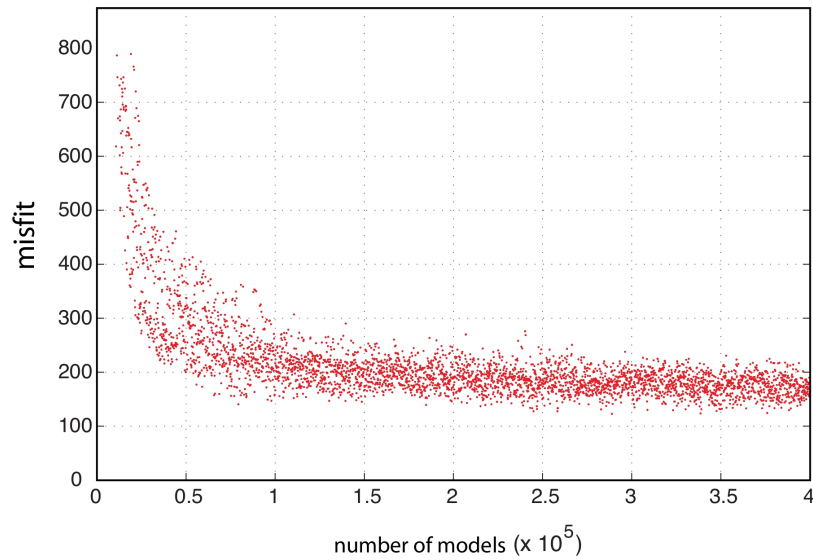


Figure 1.7: Misfit evolution along 10 Markov chains. Note that convergence has been achieved after about 300000 models (30000 mods/chain).

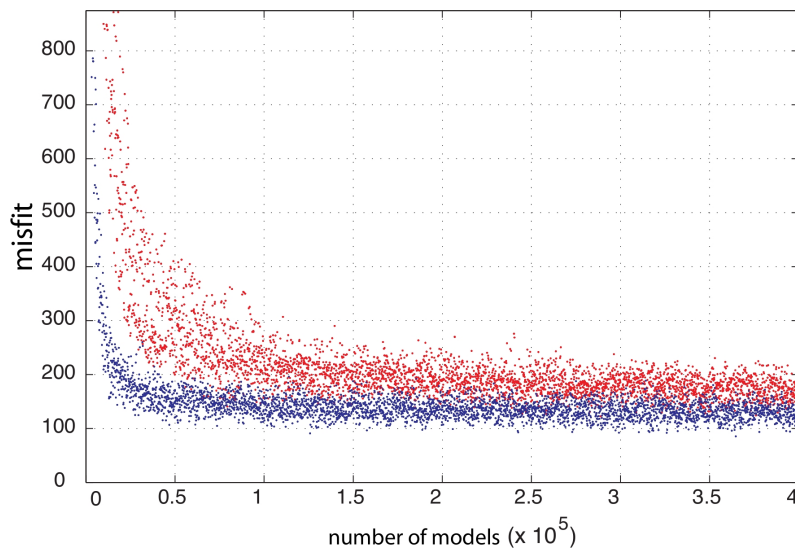


Figure 1.8: Misfit evolution along 10 Markov chains before (red) and after (blue) the application of the optimum origin time method. Note the convergence rates and misfit levels achieved in the two cases.

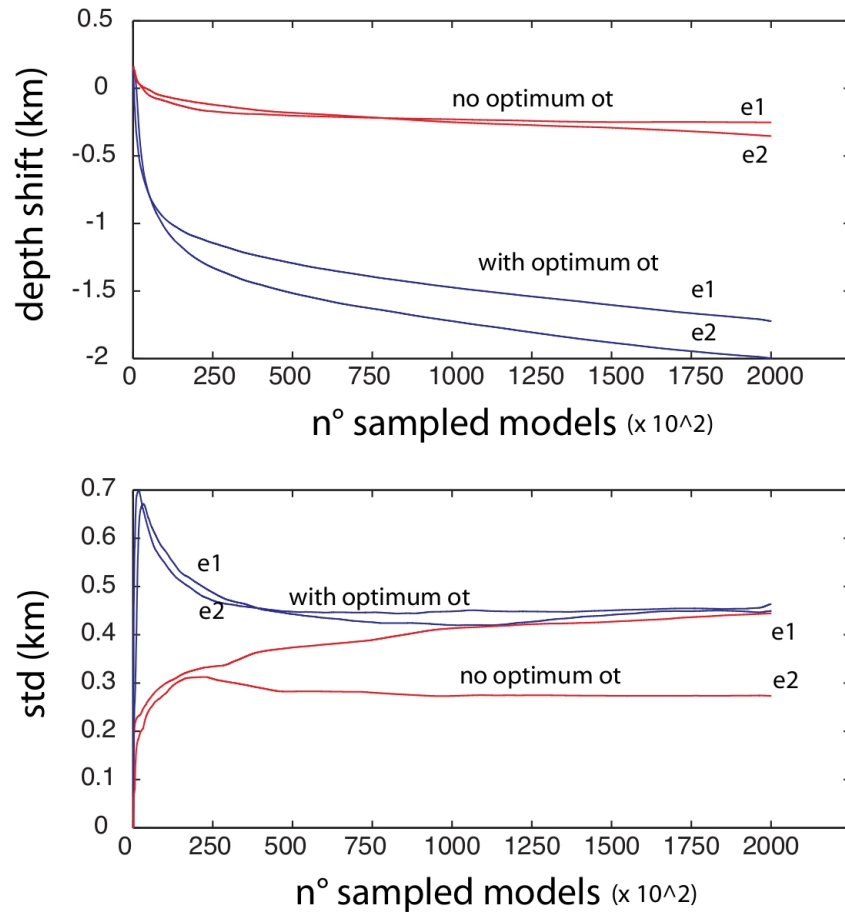


Figure 1.9: Evolution of the posterior mean (upper panel) and standard deviation (lower panel) of hypocentral depth (see encircled events in Figure 1.6). Blue and red colors correspond respectively to the results obtained with and without the application of the minimum origin time method. The depth shift indicates the shift of the earthquake depth with respect to the mean prior value. Note that the exact depth of the input model is recovered if the shift value amounts to 2.5. See text for more explanation.

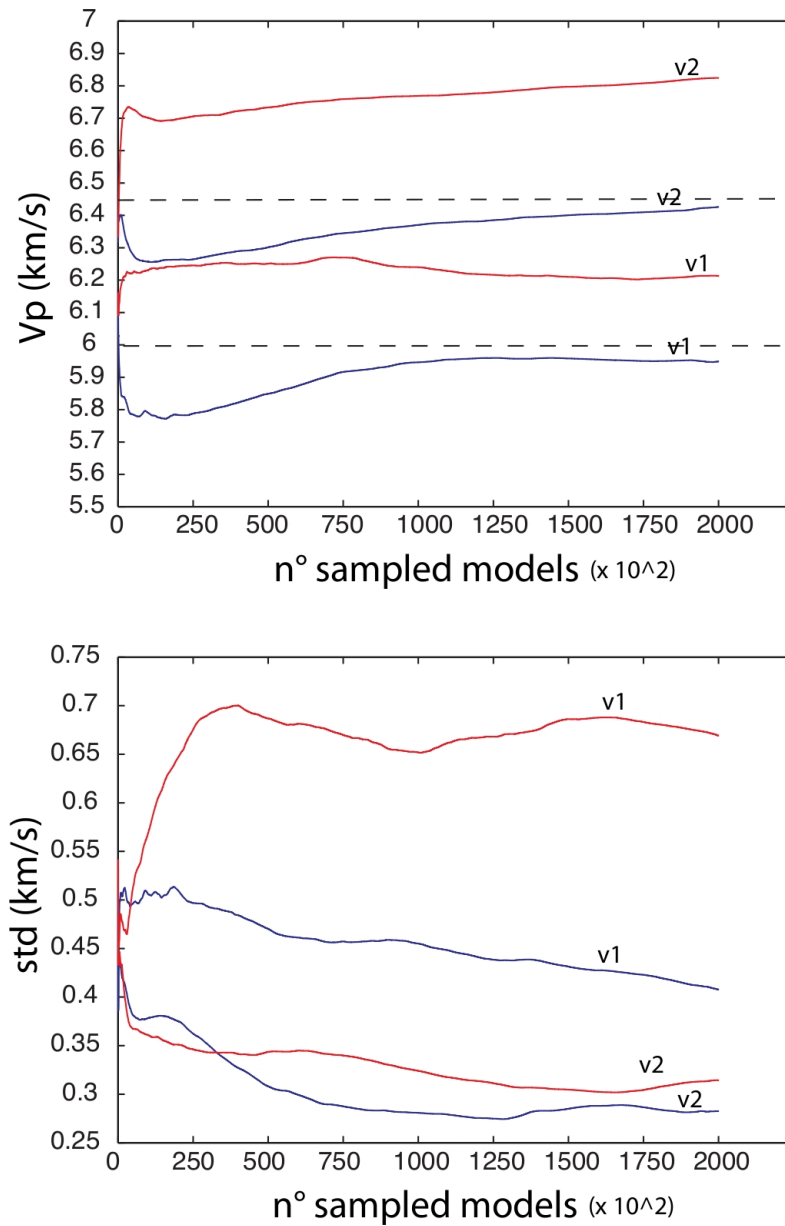


Figure 1.10: Evolution of the posterior mean (upper panel) and standard deviation (lower panel) of  $V_p$  for the two nodes marked by a red cross in Figure 1.6. Blue and red colors correspond respectively to the results obtained with and without the application of the minimum origin time method. The dashed lines indicate the corresponding values in the input velocity model. See text for more explanation.

## 2 Inversion of synthetic data

In this chapter I show the performance of the newly developed code and make a comparison with the Simulps code (Thurber, 1993; Eberhart-Phillips, 1993; Eberhart-Phillips and Reyners, 1997; 1999), which is widely used in standard linearized tomography.

### 2.0.2 Synthetic test setup

**Dataset and input velocity structure** The dataset consists of a subset of the P-wave and S-wave arrival times data gathered during an experiment in 2000-2001 in the Alto Tiberina region (Chiaraluce et al., 2007; Moretti et al., 2009). I selected 228 earthquakes recorded at 58 seismic stations (Figure 2.1), corresponding to 3405 P-phases and 3265 S-phases. I used this small dataset because it ensured the speediness of performing the synthetic tests and allows testing many different recipes of sampling of the parameter space.

The input velocity structure used to compute synthetic data is shown in Figures 2.2 and 2.3. The input structure is characterized by a 3D heterogeneous field for both the  $V_p$  and the  $V_p/V_s$ . It has been designed in order to test the capability of our code and the available data to recover high velocity bodies and a strong separation between shallow high  $V_p/V_s$  and deep low  $V_p/V_s$  regions retrieved by Moretti et al. (2009) by inverting the real data. I added to the background 1D  $V_p$  model a shallow basin-shaped anomaly with a velocity of about 20% lower than the average background model and two high  $V_p$  anomalies have velocity of 10% greater than the local average background model. The  $V_p/V_s$  model is characterized by a steep transition from  $-5\%$  to  $+5\%$  of the background  $V_p/V_s$  value (1.84).

The bseudo-bending ray-tracing algorithm by Um and Thurber (1987) is used to compute ray paths and travel times of both the P-waves and S-waves across the

## 2 Inversion of synthetic data

input models. A Gaussian noise is added to the predicted data, based on the SAC weighs (0-4) associated to the observed data (Moretti et al., 2009). These weighs correspond to standard deviations of  $0.025s$  (0),  $0.05s$  (1),  $0.1s$  (2) and  $0.3s$  (3).

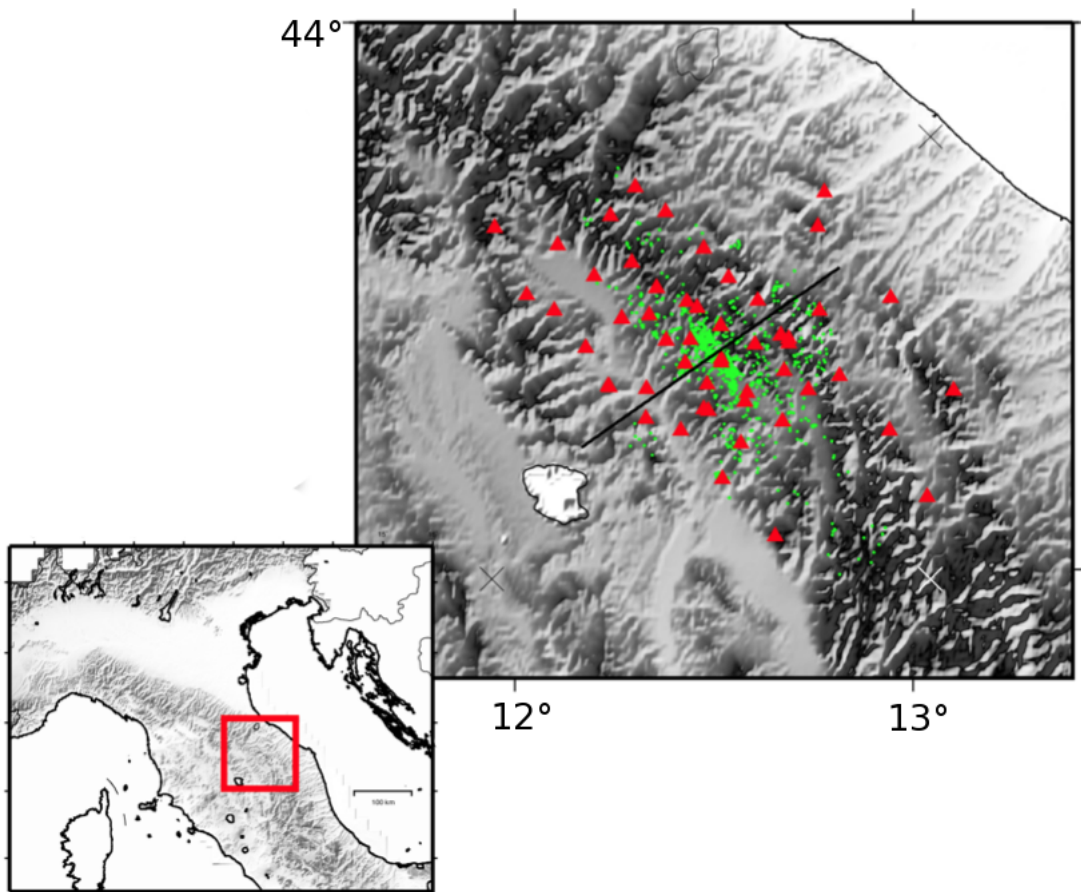


Figure 2.1: Map relief and distribution of stations (red triangles) and earthquakes (green points) used in the synthetic tests.

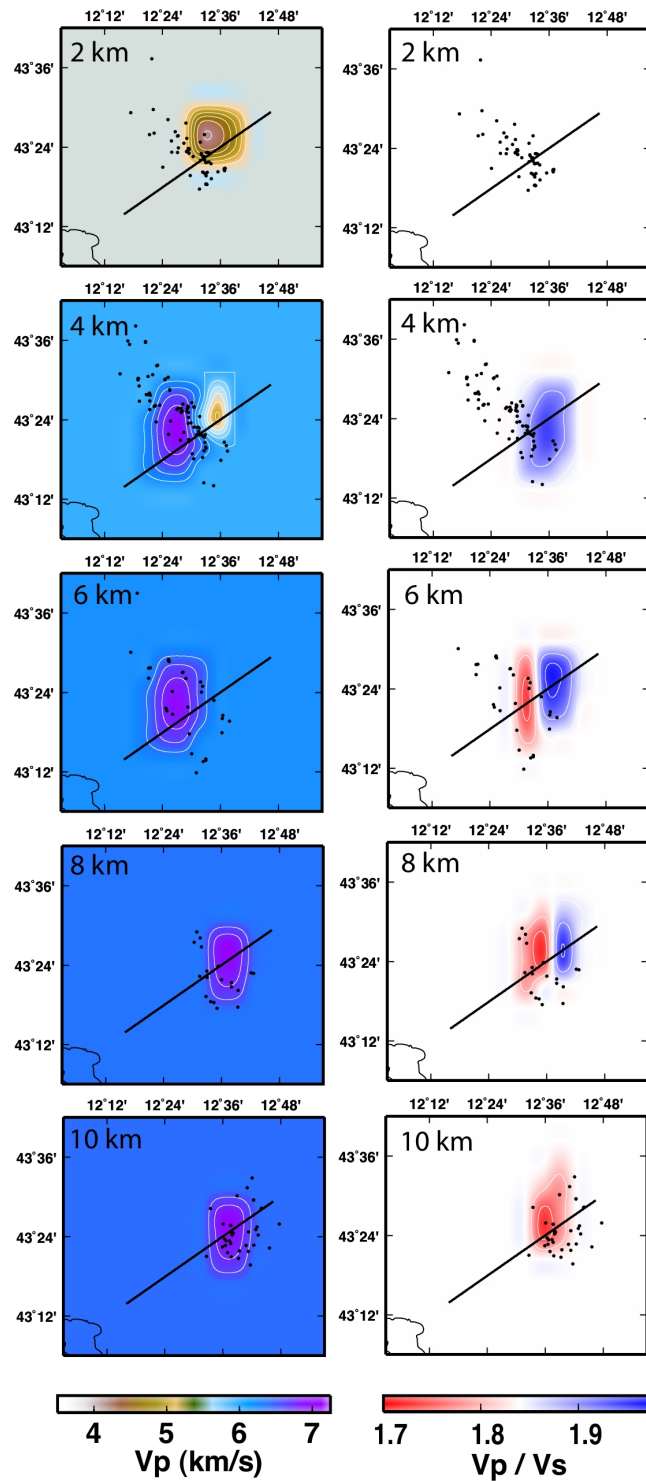


Figure 2.2: Synthetic  $V_p$  and  $V_p/V_s$  structures shown on horizontal layers at some selected depth.

## 2 Inversion of synthetic data

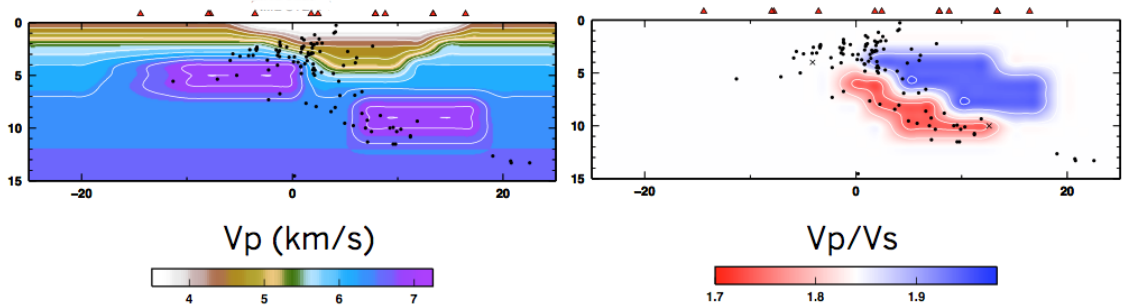


Figure 2.3: Synthetic  $V_p$  and  $V_p/V_s$  structures plotted on a vertical cross-section (see Figures 2.1 and 2.2 for the location). Black circles and red triangles mark respectively earthquakes and stations located in between 2 km from the section.

### 2.1 Rj-McMc LET

**Prior information** Two 1D Gaussian distributions have been associated to each node of the background grid (see Figure 2.4). Mean values of the  $V_p$  prior distributions are defined in order to create a 1D model. The standard deviation is equal to 0.5 km/s for each node of the grid. The prior distribution for the  $V_p/V_s$  parameter is also of Gaussian type, with mean value equal to 1.84 and standard deviation equal to 0.1.

The prior location of the earthquakes have been defined in this way: the three coordinates of each event and the origin times used to calculate the synthetic arrival times have been randomly perturbed, using Gaussian distributions with zero mean and standard deviation equal to 1.5-2.5 km and 0.25 s. These newly perturbed event parameters have been considered as mean values in the prior Gaussian distribution. The prior standard deviations are equal to 1.5 km for latitude and longitude parameters, 2.5 km for depth parameters and 0.25 s for origin time parameters.

Finally, the prior distribution for the number of Voronoi's cells is a uniform distribution in between 1 and 1000. As previously described, the prior distributions related to the spatial position of the nuclei are uniform distributions in between 0-1, because we use normalized coordinates. The real spatial extension of the LET problem, defined by the size of the background regular grid, is 90 km x 90 km x 16 km.

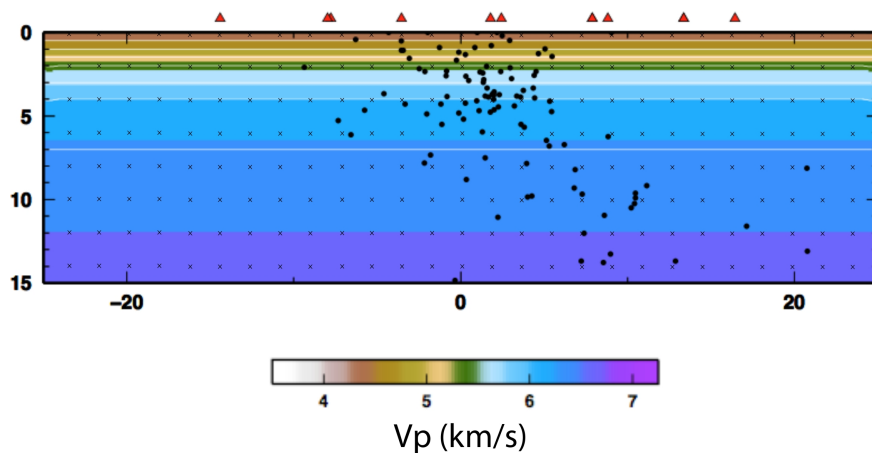


Figure 2.4: Mean values of the prior distributions for both elastic and event parameters plotted on the vertical cross-section. Black points and red triangles mark respectively the earthquakes and the stations located in between 2 km from the section. Black crosses indicate the nodes of the background regular grid. A Gaussian distribution with mean equals to the corresponding  $V_p$  and standard deviation equals to 0.5 km/s is associated to each node of the grid.

**Rj-McMc recipe of sampling** I used 20 Markov chains, each one starting from a different model drawn from the prior distribution. During the sampling of the model space, the candidate models are designed according to the moves and the proposal distributions described in the previous chapter. Several different recipes of sampling of the parameter space have been tested. The recipe that allowed a faster achievement of the convergence and a balanced sampling between elastic and earthquakes parameters is the following one:

- MOVE 1 (probability 0.25): perturbation of both the  $V_p$  and the  $V_p/V_s$  of 1 Voronoi's cell every 100 cells existing in the current model. The proposal distributions are of Gaussian type, centered on the  $V_p$  and  $V_p/V_s$  values of the current model and of standard deviation that amounts to 25% of the standard deviation of the priors.
- MOVE 2 (probability 0.20): perturbation of the spatial location of one randomly selected nucleus. Each one of the nucleus coordinates is drawn from a uniform proposal distribution in the interval  $x_i - 0.005 < x_i < x_i + 0.005$ ,

where  $x_i$  is the correspondent coordinate value in the current model. In dimensional coordinates, this means that each coordinates is moved from the current position up to about 450 m.

- MOVE 3 (probability 0.075): birth of up to 5 nuclei whose positions are randomly choose in the space. The values of  $V_p$  and  $V_p/V_s$  are extracted from the background regular grid and then perturbed in the same way described for MOVE 1.
- MOVE 4 (probability 0.075): death of up to 5 nuclei.
- MOVE 5 (probability 0.20): perturbation of the epicentral coordinates of one earthquakes according to a proposal distribution of Gaussian type, centered on the correspondent values in the current model and with standard deviations equal to 10% of the standard deviation of the priors.
- MOVE 6 (probability 0.20): perturbation of the depth of one earthquake with a proposal similar to that described for MOVE 5.

The origin times of the earthquakes are estimated for each candidate model in order to minimize the misfit between calculated and observed travel times.

### 2.1.1 Misfit evolution and convergence assessment

The simulated annealing scheme is applied to increase the acceptance rate during the first part (about 100000 models/chain) of the sampling (see Figure 2.5). Convergence has been achieved after about 200000 models/chain, as testified by both the misfit evolution and the difference in the acceptance ratios between models accepted by a decrease of the misfit and models accepted by an increase of the misfit. After the convergence, the overall acceptance ratio is equal to 0.21 and the acceptance ratio related to a misfit increase is equal to 0.09, i.e., almost the half of the total acceptance ratio. Every 20th models of the 250000 models/chain accepted during the post burn-in phase have been collected to produce the PDF. The thinning of the chain is required in order to reduce the dependence between the collected models. The misfit level reached by the chains during the post burn-in phase is in the

range 5200-6200. The estimated parameters are 912 event parameters (4 parameters for each of the 228 events) and 5 parameters ( $x$ ,  $y$ ,  $z$ ,  $V_p$ ,  $V_p/V_s$ ) for a number of Voronoi's cells in the range 200-300, depending on both the chain and the individual model. Since the total number of estimated parameters is in the range 1100-1600 and the number of data is 6670, this misfit level corresponds to a normalized  $\chi^2$  misfit measure in the range 0.93-1.22.

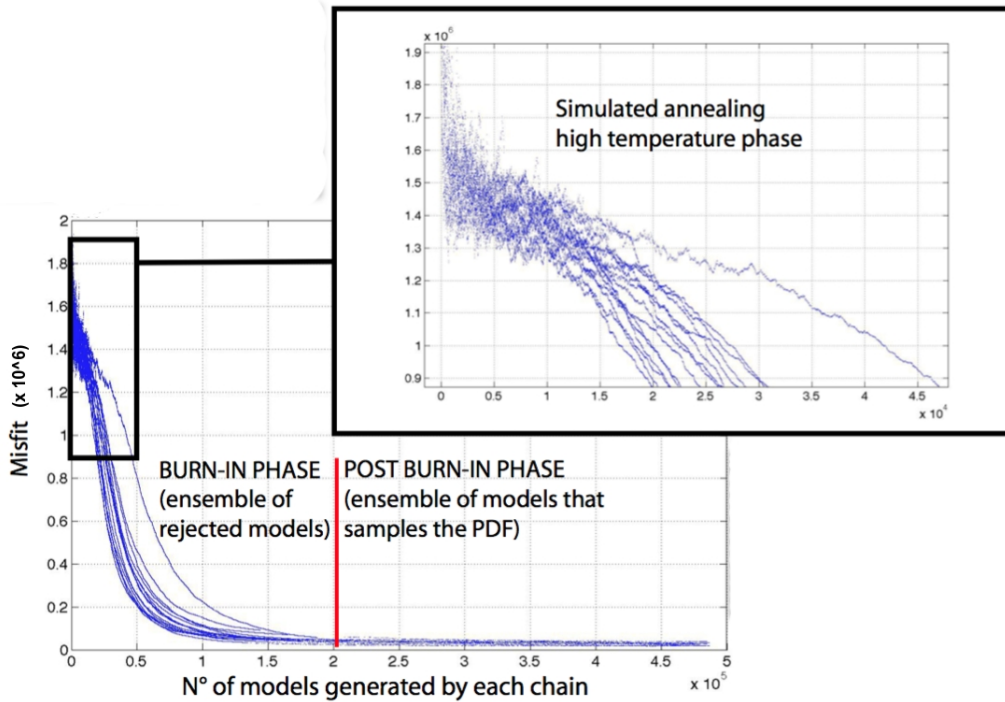


Figure 2.5: Misfit function evolution during the sampling of the parameters space. Each series of points represents the misfit related to the models accepted along one of the 20 Markov chain. The inset highlights the effects of the simulated annealing scheme, with a higher oscillating trend in the misfit due to the higher probability to accept candidate models characterized by a likelihood function value lower than that of the current model. The vertical red line divides models generated during the BURN-IN phase, that are not considered samples of the PDF, from models generated when the misfit has reached a stationary state, that are considered as distributed according to the PDF.

### 2.1.2 Analyses of marginal PDF and errors estimate accuracy

Once the PDF has been obtained, we can estimate the values of the target parameters by computing the 1D marginal PDFs, i.e. by computing the frequency distributions of the parameters and derive some estimators, such as posterior mean and standard deviation values. Figures 2.7 and 2.6 show the mean values of the 1D marginal PDFs plotted on the same vertical and horizontal sections of Figures 2.3 and 2.2. The overall velocity structure is well recovered for both the  $V_p$  and  $V_p/V_s$  and also the earthquake locations are very close to those in the input model.

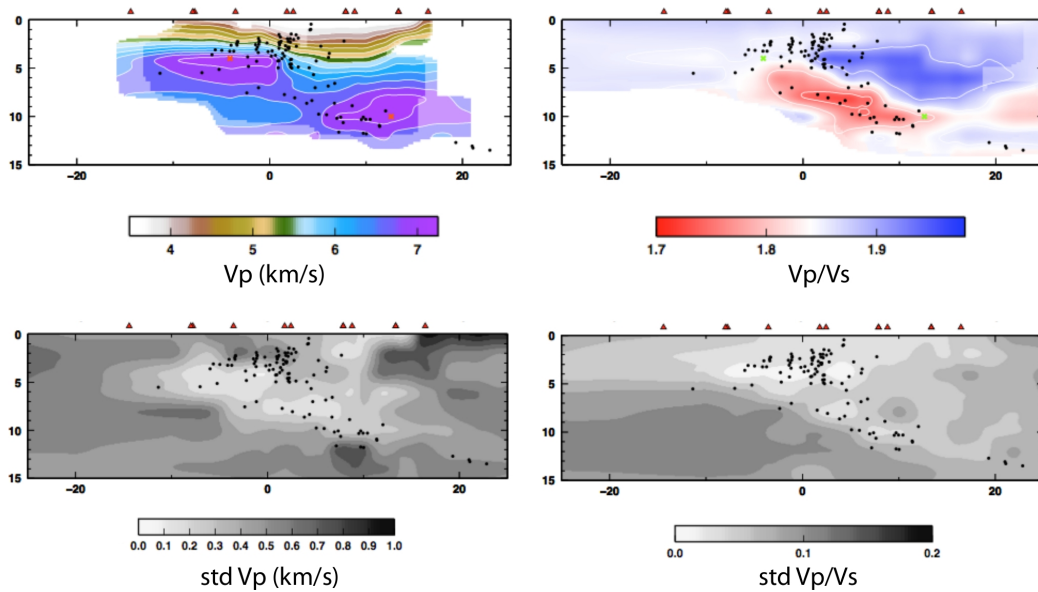


Figure 2.6: Mean posterior values (upper panels) and standard deviations (lower panels) of  $V_p$  (left panels),  $V_p/V_s$  (right panels) and earthquake hypocentral coordinates. The red and green crosses mark the location of the two nodes whose frequency distributions are image in Figure 2.8. In the upper panels the white regions correspond to not-resolved region (posterior standard deviation higher than prior standard deviation), the shaded area correspond to regions where the posterior standard deviation is less than the prior standard deviation and full color region correspond to well-resolved regions where the prior standard deviation amounts to less than half of the prior standard deviation.

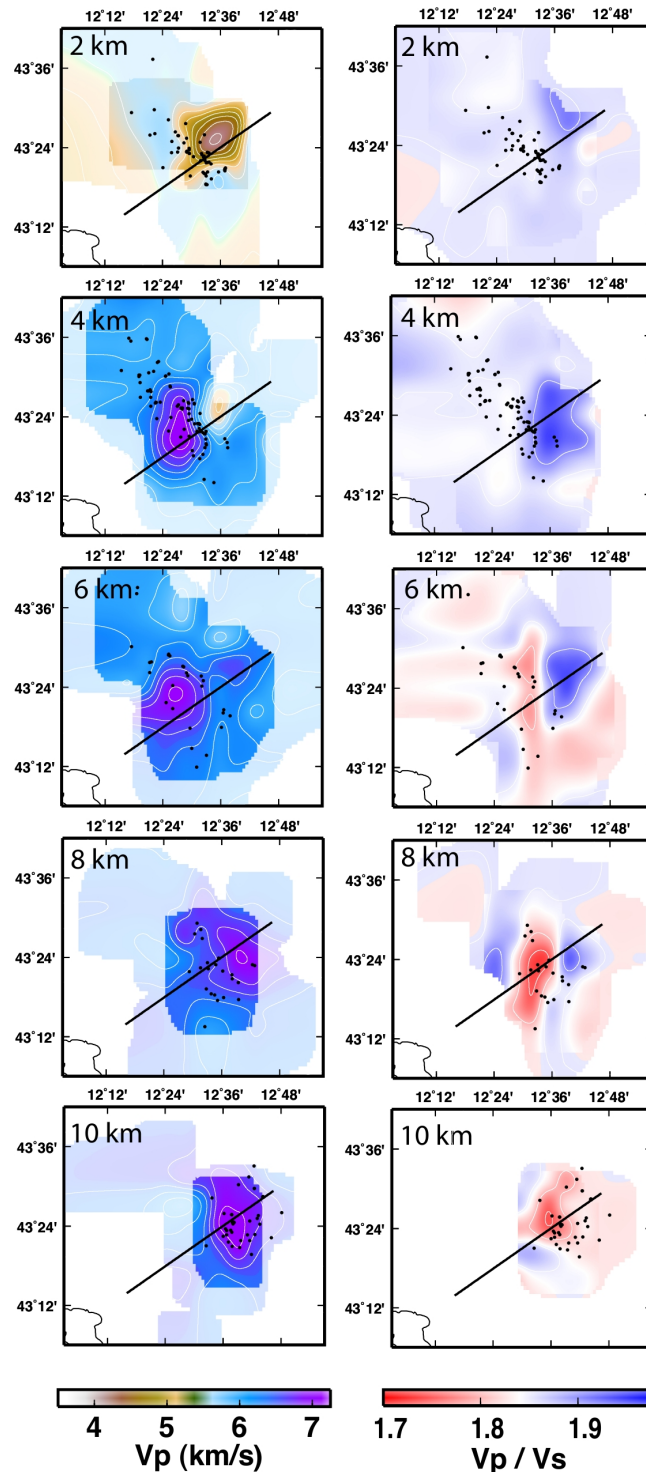


Figure 2.7: Mean posterior values of  $V_p$  (left panels) and  $V_p/V_s$  (right panels) at selected depth. The white regions correspond to not-resolved regions (posterior standard deviation higher than prior standard deviation), the shaded areas correspond to regions where the posterior standard deviation is less than the prior standard deviation and full color regions correspond to well-resolved regions, where the prior standard deviation amounts to less than half of the prior standard deviation.

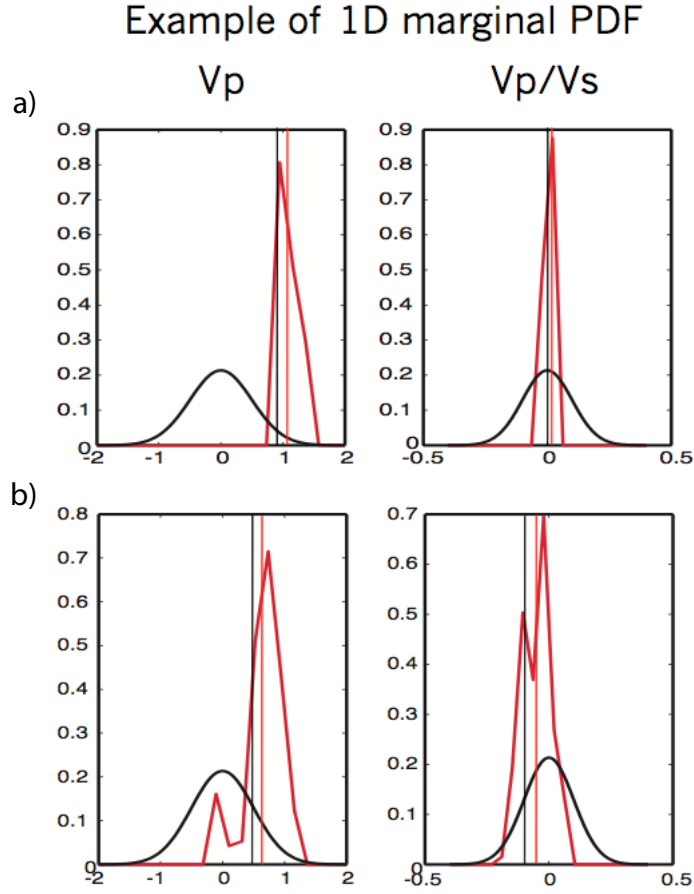


Figure 2.8: 1D marginal PDFs (red curves) of the  $V_p$  (to the left) and  $V_p/V_s$  (to the right) at two different nodes of the background regular grid. The position of the two nodes is highlighted by two crosses in Figure 2.7. The black Gaussian curves represent the prior density functions. The coordinate  $x$  represents the difference between posterior and prior values. Red vertical line mark the mean posterior values whereas black vertical lines the values in the input synthetic model (i.e. the target values). a) node 1:  $\bar{V}_p = 7.06\text{km/s}$ ,  $\sigma = 0.14\text{km/s}$  (input value =  $6.9\text{km/s}$ ),  $\bar{V}_p/\bar{V}_s = 1.85$ ,  $\sigma = 0.01$  (input value =  $1.84$ ); b) node 2:  $\bar{V}_p = 7.1\text{km/s}$ ,  $\sigma = 0.28\text{km/s}$  (input value =  $6.9\text{km/s}$ ),  $\bar{V}_p/\bar{V}_s = 1.79$ ,  $\sigma = 0.05$  (input value =  $1.74$ ).

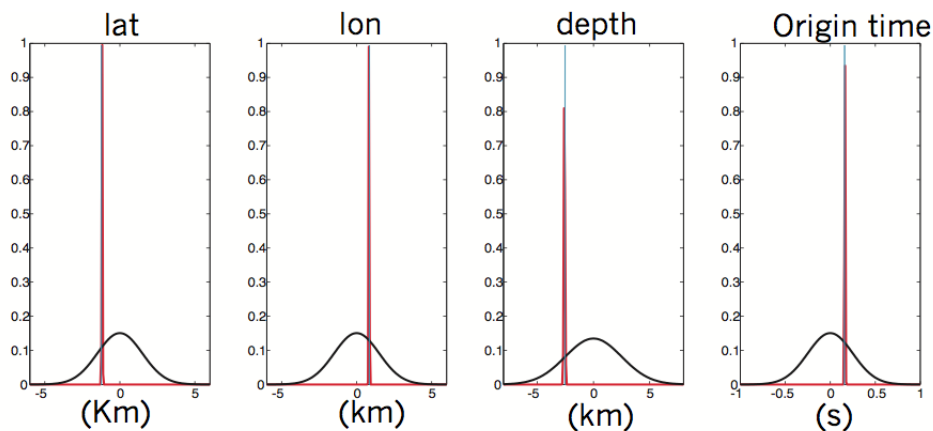


Figure 2.9: 1D marginal PDFs (red curves) on the 4 event parameters related to one earthquake. The black Gaussian lines represent the prior density functions. The coordinate  $x$  represents the difference between posterior and prior values. Red vertical line mark the mean posterior values whereas black vertical lines the values in the input synthetic model.

Figure 2.8 shows the frequency distributions of the  $V_p$  and  $V_p/V_s$  at two points of the background regular grid, together with the prior distributions.

The parameters  $V_p$  and  $V_p/V_s$  shown in the Figure 2.8a have unimodal frequency distributions. The distributions are narrow and the mean posterior values are near the maximum probability values. The mean posterior  $V_p$  and  $V_p/V_s$  are very close to that in the input model. It is worthy to note that the estimate of the  $V_p$  is good even if the value corresponds to low a very low probability region in the prior distribution (black curve centered on  $x = 0$ ). The frequency distributions are sometimes multimodals and the computation of the mean and standard deviations values may be meaningless. Nevertheless, as in the case of the parameters shown in the Figure 2.8b, the mean posterior value represents a more reliable estimate than the higher probability value. The double pick has the effect to increase the value of the standard deviation. In this case, for all the four parameters, the input values are proper recovered in the range  $\pm 1\sigma$  where  $\sigma$  is the posterior standard deviation.

It is worthy to note that the posterior standard deviation can approach or exceed the prior standard deviation in two cases. The first one happens when data provide no additional information of the parameters. The second one may happen when the

## 2 Inversion of synthetic data

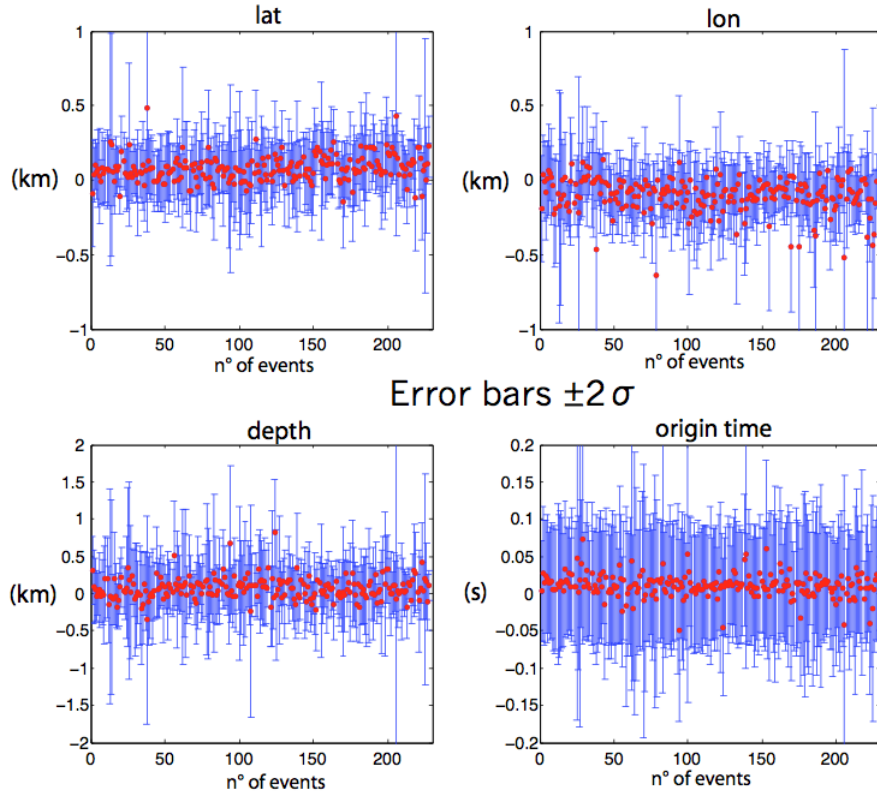


Figure 2.10: Difference between the mean posterior value of each event parameter and the corresponding value in the input synthetic model.

posterior distribution is not unimodal. In this second case it would be suitable to investigate the whole posterior distribution and not just the mean and standard deviation values. Nevertheless, because of the high number of parameters to estimate in the LET inversion problem, the visual inspection of every posterior distribution is impossible. Then, we considered as “resolved” those parameters that are characterized by a substantial reduction in the standard deviation of the posterior distribution with respect to the prior one.

Figure 2.9 shows the frequency distributions for the 4 parameters of one earthquake. In this case the 1D marginal PDFs are very narrow, clearly unimodal and the posterior mean values are very similar to that used in the input synthetic model. Figure 2.10 shows the difference between the mean posterior value of each earthquake parameter and the corresponding value in the input model.

## 2.2 Simulps LET

The same synthetic test described in the previous section has been performed with the SIMULPS13 code (Thurber, 1993; Eberhart-Phillips, 1993; Eberhart-Phillips and Reyners, 1997; 1999). Since the synthetic data and the ray-tracing algorithm (Um and Thurber, 1987) are the same, every difference in the results must be attributed to the different approach to both parameters estimation and model parameterization.

### 2.2.1 Standard linearized approach to LET

Given starting earthquake locations and a starting model of velocity field, the ray tracing allows computing theoretical arrival times. Then, the differences between the observed arrival times and the arrival times calculated in the initial model (named residuals,  $r_{ij}$ ) are used as observed data in the inversion procedure. The residuals can then be related to perturbations of the earthquake coordinates ( $\Delta x^i$ ), the origin time ( $\Delta \tau_i$ ) and the velocity structure ( $\Delta m$ ). By assuming that the travel time anomaly is stationary for a small perturbation of the ray-path:

$$r_{ij} = \sum_{k=1}^3 \frac{\partial T_{ij}}{\partial x_k^i} \Delta x_k^i + \Delta \tau_i + \int_{\gamma_{ij}} \frac{1}{\delta v} ds = \sum_{k=1}^3 \frac{\partial T_{ij}}{\partial x_k^i} \Delta x_k^i + \Delta \tau_i + \sum_{l=1}^L \frac{\delta T_{ij}}{\partial m_l} \Delta m_l \quad (2.1)$$

With an iterative scheme for solution, the linearized inversion code improves the estimates of the velocity structure and model parameters by perturbing them in order to minimize the weighted root-mean-square misfit. This goal is achieved by applying iteratively the damped least square method, with the appropriate damping parameter found using a trade-off analyses (Menke, 1986).

### 2.2.2 Model parameterization and starting models

The resolution of linearized tomography strongly depends on the particular choices about model parameterization. The travel-times data are inverted for the  $V_p$  and  $V_p/V_s$  values at the nodes of a 3D regular grid. The grid is regular but not constant in spacing, with a finer spacing in the regions with a better ray-coverage and coarser

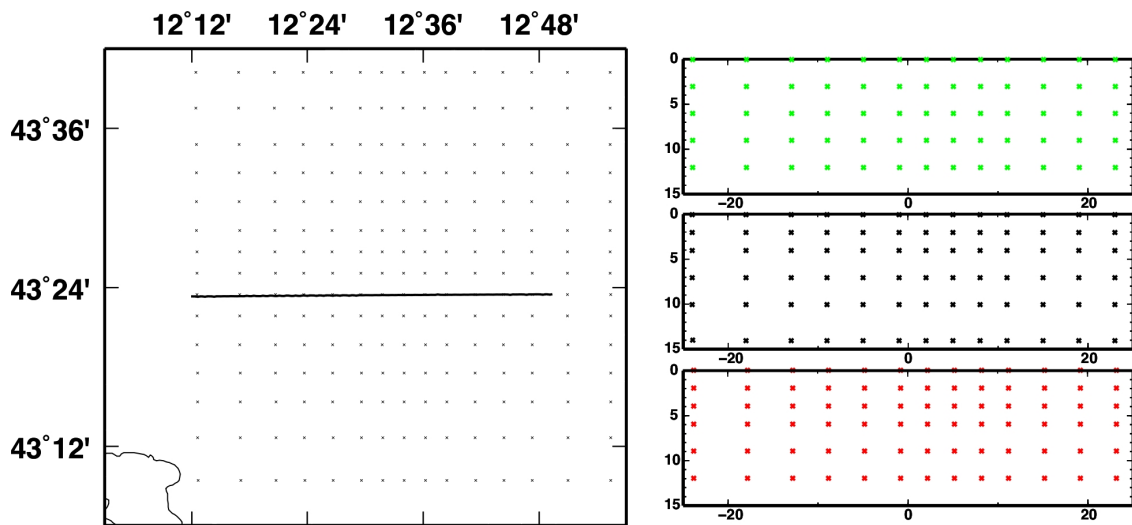


Figure 2.11: Three examples of model parameterization. The grid geometry is the same on the horizontal layers (right panel) but differ in the vertical direction (left panels). Green model (M1): inter-nodal vertical spacing of 3 km. Black model (M2): vertical spacing of 2 km down to 4 km and 3-4 km for the deeper layers. Red model (M3): vertical spacing of 2 km down to 6 km and 3 km for the deeper layer.

elsewhere. Each layer of nodes shares the same grid spacing but the distance between different layers can be different. Usually the vertical spacing increases at increasing depth, because at depth the resolution is potentially lower. More, data are inverted only for those nodes that are characterized by a derivative weight sum greater than a certain threshold. The DWS represents an estimate of the ray density around each of the grid nodes (Thurber, 1993). Velocity values are assigned to nodes of a 3-D grid and the velocity is continuously defined within the volume by using a linear interpolation with the surrounding eight neighboring nodes.

As previously seen, the wider is the grid spacing, the lower will be the model resolution and smaller the model uncertainties. By reducing the spacing, the model resolution is potentially higher but the solution becomes quickly non-unique and some regularization is required to get a unique solution. The regularization method employed in the `simulps13` code is the constraint of minimizing the L2-norm of the model parameters, with the appropriate damping value selected according to a trade-off between data and solution variance (Menke, 1989; Eberhart-Phillips, 1986). I

choose the more suitable parameterization after some trial inversions, looking at the resulting model, the final data misfit and the resolution matrix. To find the best damping parameter, I run some single-iteration inversions varying the damping until the correct balance of misfit reduction and model complexity was found.

Three different trial parameterizations are shown in Figure 2.11. The grids of nodes are identical in the horizontal planes but they differ for the vertical node spacing. As I shall show afterwards, the three parameterizations allow obtaining roughly the same data misfit but the reliability of the resulting velocity models is different.

For each model, all inversion parameters are identical, except for the appropriate damping value, selected according to the different trade-off curves.

**Starting models** The starting models for  $V_p$  and  $V_p/V_s$  and the starting earthquake parameters are equal to the mean values of the prior distributions used in the Rj-McMc LET synthetic test (see Figure 2.4).

### 2.2.3 Data misfit and resolution analysis

For each of the three different parameterizations, the best-fit model is obtained after 5 iterations. In the first iteration the data have been inverted to adjust the earthquake locations. During the subsequent 4 iterations the data have been inverted simultaneously for both the  $V_p$ ,  $V_p/V_s$  and earthquakes parameters. At each iteration the solution model of the previous iteration is used as starting model. The number of iterations has been chosen according to the f-test results, i.e., iterations stop when the further reduction in data variance is negligible according to the f-test statistic. The data variance reductions, i.e. the difference between the data variance computed in the starting model and the data variance computed in the final mode, are in the range 85-87%, for the three models.

The analysis of the uncertainty associated to every inverted parameter could be done by the inspection of the standard errors. Nevertheless, the estimate of the standard errors is biased by the regularization applied to the inversion. Usually, the higher the damping value is, the lower is the estimated standard errors. The real values of standard errors could be derived by setting the damping values close to

## 2 Inversion of synthetic data

zero. But in this case the inversion becomes extremely unstable.

A way to overcome this problem and to assess the resolution of the results is to analyze the full model resolution matrix (Menke, 1989). At this scope, I computed the averaging vectors of the model resolution matrix for each of the inverted nodes and the correspondent value of the spread function. For a node to be adequately resolved, its row of the resolution matrix should be peaked on the diagonal, without a significant contribution from off-diagonal nodes. The relative size and pattern of the off-diagonal elements show how much a given parameter is smeared on the surrounding nodes (i.e., the correlation between the given parameter and the others). A compact way of estimating how strong and peaked the resolution is for a given inversion node is the spread function (Michellini & McEvelly, 1991; Toomey & Foulger, 1989). The spread function  $SPF_j$  for a node  $j$  is computed from all the elements  $R_{jk}$  of the corresponding row of the resolution matrix  $R$ , weighted depending on the distance  $D_{jk}$  between the node  $j$  and the surrounding  $k$  nodes ( $k = 1, 2, \dots, N$ ):

$$SPF_j = \text{Log} \left[ \|R_j\|^{-1} \sum_{k=1}^N \left( \frac{R_{jk}}{\|R_j\|} \right)^2 D_{jk} \right] \quad (2.2)$$

For each node (i.e. for each averaging vector), the contour of the volume where the resolution is 70 per cent of the off-diagonal element allows easily to visualize the directionality of the smearing between each parameter and the surrounding parameters (Figure 2.12). Note for example the vertical smearing of velocity between nodes located at 0 and 3 km depth. By the inspection of resolution plots like that shown in Figure 2.12 a certain threshold for the SPF can be chosen. Parameters characterized by an SPF value less than the threshold should be considered as not resolved. Conversely, if the SPF value is greater than the threshold the parameter can be considered as well resolved. Clearly the choice of the threshold is arbitrary. Anyway, the best way to assess the resolution is by comparing the resulting models with the input synthetic models.

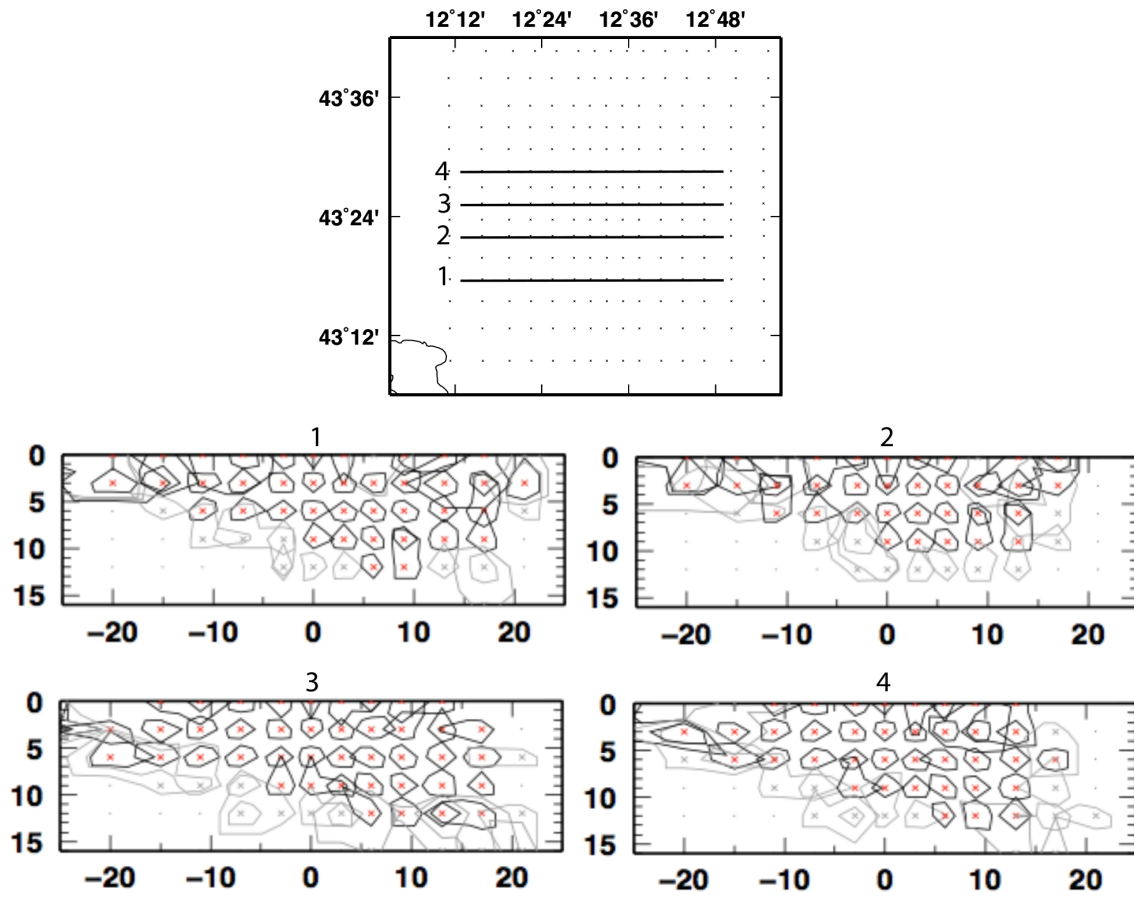


Figure 2.12: Model resolution for the  $V_p$  parameters of model M1 plotted on 4 vertical sections. The 70% smearing contouring for inverted nodes (crosses) with spread function  $\leq 2.5$  is shown. The nodes with  $SPF_j \leq 2$  and with  $2.0 < SPF_j \leq 2.5$  have red and grey crosses, respectively.

### 2.2.4 Best-fit $V_p$ and $V_p/V_s$ models

In Figure 2.13 the  $V_p$  models obtained with the three different parameterizations are plotted on a vertical cross-section, together with the input synthetic  $V_p$  model. The main  $V_p$  features are recovered in all the three models, except for the deeper high  $V_p$  anomaly, where the  $V_p$  is notably lower than in the input model. Model M2 is characterized by the relative better correspondence with the input synthetic model. Figure 2.14 shows the  $V_p$  and  $V_p/V_s$  parameters of model M2 plotted on the horizontal layers. Figure 2.15 (bottom panels) shows the vertical cross-section for both the  $V_p$  and  $V_p/V_s$  structure of model M2. Also not well recovered is the shallow  $V_p/V_s$  model, where the high  $V_p/V_s$  region in the synthetic model is visibly smeared at shallower depth.

**Effect of the regularization constraint** In all the three models, the shallower high  $V_p$  anomaly is recovered better than the deeper one (see Figure 2.13). This is likely a consequence of the different ray coverage and density in the two model regions. The difference in data resolution power of the two model regions is enhanced by the regularization constraint, which over damps the deeper anomaly, further reducing the data resolution power. The low  $V_p$  basin-shaped anomaly at shallow depth is characterized by a similar over-damping in all the three models, with the  $V_p$  locally approaching the starting value. Consequently, the lateral continuity of the low  $V_p$  basin in the synthetic model can't be correctly recovered. A similar reason can be advocated for the smearing of the high  $V_p/V_s$  regions into shallower depth (see Figure 2.15 bottom right panel). In this case the regularization constraints has the effect to enhance the correlation between parameters, as also suggested by the analysis of the model resolution matrix.

**Dependence of the model on the parameterization** The location of the shallow high  $V_p$  anomaly depends on where the grid nodes are placed. Models M2 (a) and M3 (b) have the grid nodes in locations similar to those used to construct the input synthetic model and the high  $V_p$  anomaly is correctly placed. Conversely, in model M1 (c) the correspondent grid nodes are located at higher depth and the high  $V_p$  anomaly is shifted accordingly.

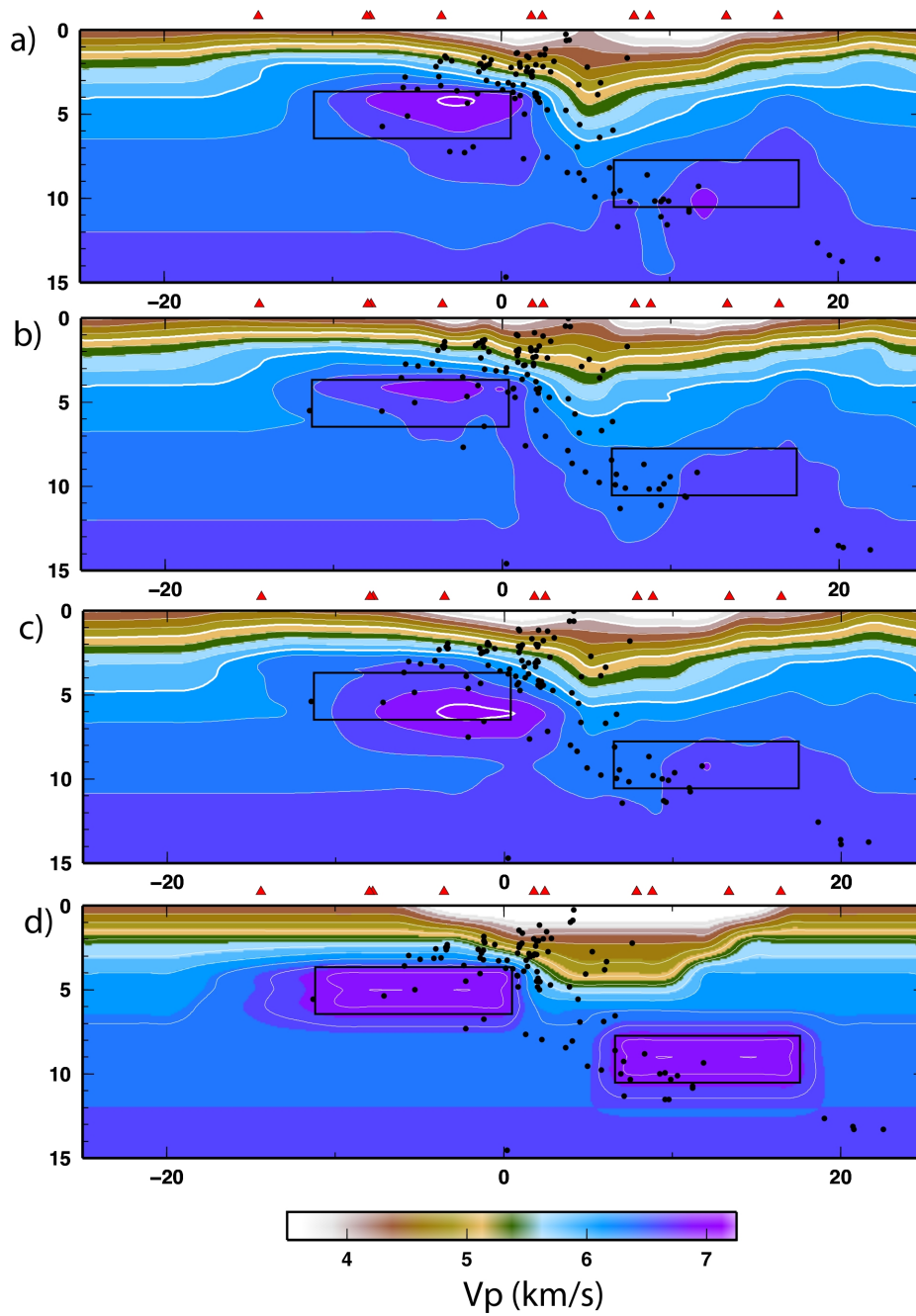


Figure 2.13: Best-fit Vp models plotted on a vertical cross-section (see Figure 2.14 for the location); a) model M2, b) model M3, c) model M1, d) synthetic input model. The black rectangles highlight the correct location of the high Vp anomalies.

## 2 Inversion of synthetic data

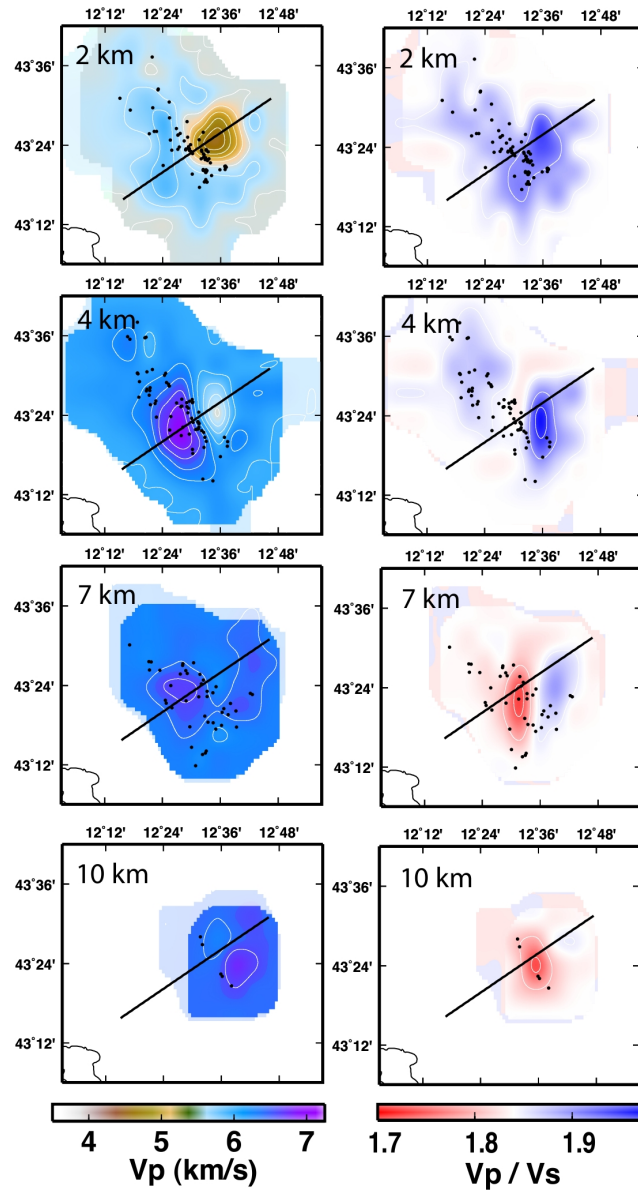


Figure 2.14: Best-fit  $V_p$  (right panels) and  $V_p/V_s$  (left panels) models. White regions correspond to not-resolved region ( $SPF > 2.5$ ), shaded areas correspond to regions where the resolution could be questionable ( $SPF > 2$ ) and full color region correspond to resolved regions ( $SPF < 2.0$ ).

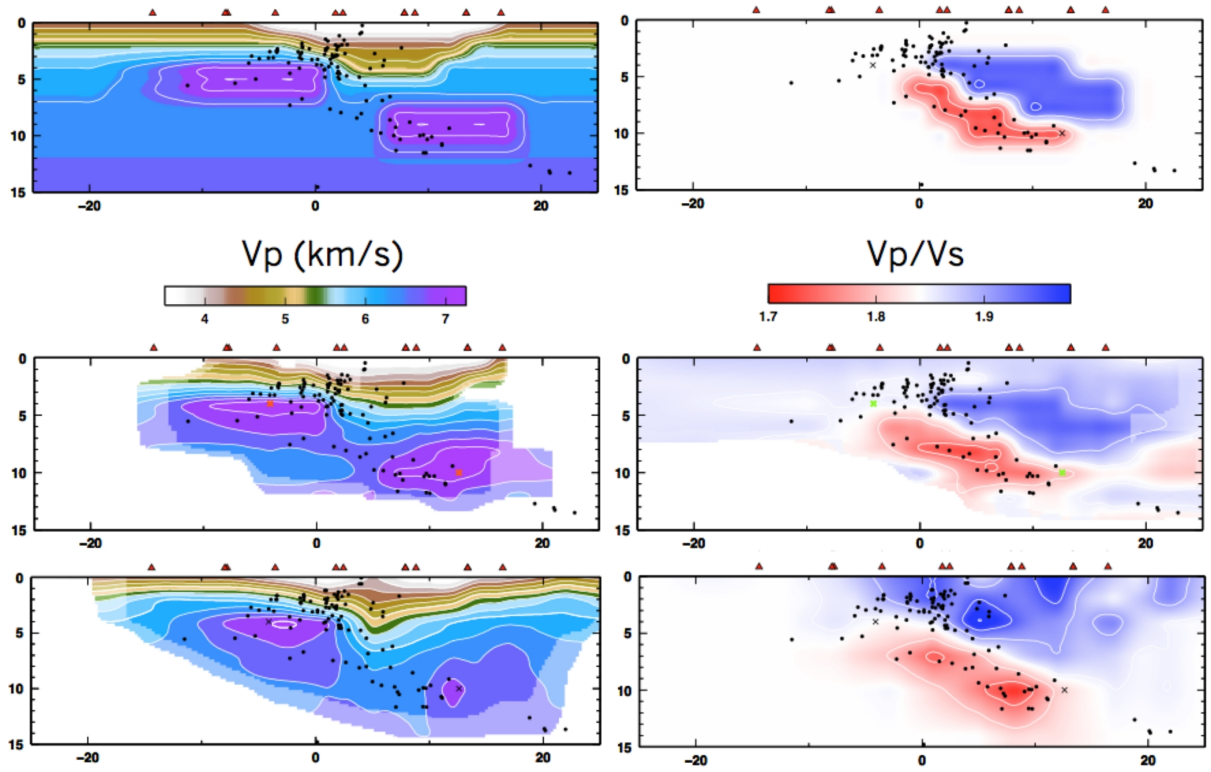


Figure 2.15:  $V_p$  (right panel) and  $V_p/V_s$  (left panel) models plotted on a vertical cross-section (see Figure 2.14 for the location). Top panels: synthetic input models; central panels: mean posterior models of the RjMCMC LET (see Figure 2.8); bottom panels: best-fit model M2 of Simulps13 LET. The white regions correspond to not-resolved region ( $\text{SPF} > 2.5$ ), the shaded areas correspond to regions where the resolution is poor ( $\text{SPF} > 2$ ) and full color regions correspond to well-resolved regions ( $\text{SPF} < 2$ ).

## 2.3 Comparison between Simulps and Rj-McMc results

### 2.3.1 Data fitting

The final misfit, calculated according to REF, is in the range 8100-9050 for the three models obtained with SIMULPS. The data fitting in SIMULPS is usually given in terms of data variance reduction.

I chose to use the simple least square data misfit for the comparison because the data variance computed by SIMULPS is weighted and the weighting scheme is different between the two inversion methods. Conversely, the least squares misfit depends only on the data uncertainties. For example, no different weight is given for travel-time residuals greater than a certain threshold. The least square misfit obtain with SIMULPS is about about 30% greater than the misfit obtain with our code. The better performance of the Rj-McMc code is notable also by comparing the resulting velocity models (Figure 2.15).

### 2.3.2 Dependence on parametrization and regularization

The number of inverted parameters for the three models is in the range 2200-2832 (1288-1920 velocity parameters and 912 event parameters). It is notable that with our code, although the locations of the cells are unknown, the total number of parameter describing the velocity structure is less than the number of velocity parameter inverted by SIMULPS.

In Figure 2.15 both the  $V_p$  and the  $V_p/V_s$  models are shown, together with the mean  $V_p$  and  $V_p/V_s$  models obtained from the Rj-McMc code. Looking at the Figure, the velocity structure is better resolved by the Rj-McMc tomography than by the linearized tomography, for both the  $V_p$  and  $V_p/V_s$  structures. The Rj-McMc models don't depend on the particular choice about parameterization, because the best parameterization is directly extracted by the data. More, the intensity of the high  $V_p$  anomalies is well recovered for both the shallower and deeper anomalies, independently of the difference in the density of ray-coverage. This improvement is essentially due to the absence of any global regularization

### 2.3 Comparison between Simulps and Rj-McMc results

applied to the inversion technique. The absence of regularization strongly reduces the smearing of the individual parameters toward the surrounding volume and allows the Rj-McMc tomography to recover both the lateral continuity of the low Vp shallow basin and the absence of Vp/Vs anomalies down to 3 km depth.

Finally, the earthquakes locations are better recovered too. To show this, I computed, for each parameter of every earthquakes, the difference between the values obtained after the inversion and the corresponding values in the input synthetic model (Figure 2.16). The input synthetic locations are better recovered by the Rj-McMc tomography than by the Simulps13 tomography for all the four events parameters.

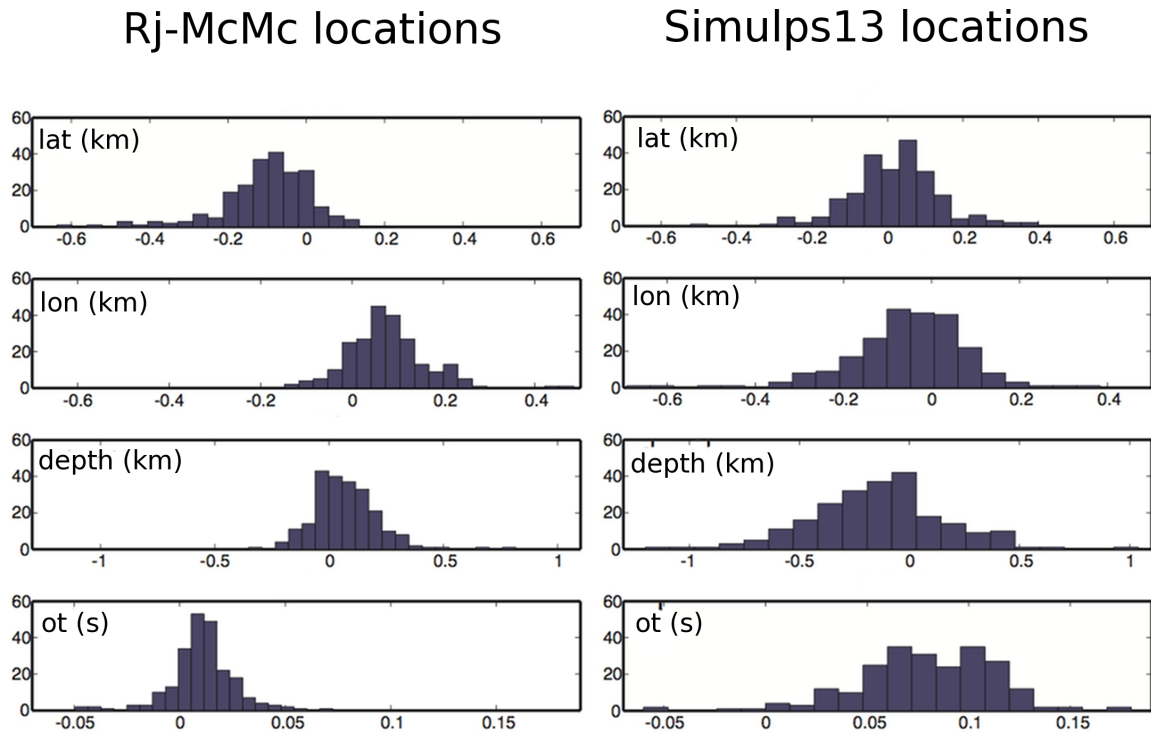


Figure 2.16: Frequency distributions of the differences between recovered and input earthquake parameters.

### 2.3.3 Dependence on starting model

To test the dependence of the inversion solution from the starting model and prior information, the synthetic test previously described has been repeated by changing only the starting Vp model in the Simulps13 inversion and the mean values of the prior distribution in the Rj-McMc tomography. The synthetic input structure is unchanged. The only difference between the two synthetic tests is the 1D starting Vp model that in TEST2 has an additional low velocity layer between 5 and 7 km depth.

Figure 2.17 shows the Vp model obtained with the two different starting models by the two inversion codes. As expected, the mean posterior model obtained by the Rj-McMc code is quite similar in the two cases. Conversely, the two Simulps13 model solutions have notable differences, showing a strong dependence on the starting Vp structure. The shallower high Vp anomaly in the SIMUPS solution, for example, is reduced in thickness and increased in intensity because of the existence of the low velocity layer in the starting model. In the Rj-McMc tomography, the Vp value is sampled in between  $\pm 4\sigma$  from the mean value of the prior distribution. At 6 km depth, the mean values in the two cases are 6.2 km/s and 5.2 km/s and the Vp parameter is sampled in the ranges 4.2-8.2 km/s and 3.2-7.2 km/s, respectively. In the correspondence of the high Vp anomaly the value is 6.9 km/s, which is inside the ranges of the prior distribution. Therefore, the correct value of the Vp is recovered despite the difference in the prior distributions. The only difference in the two cases is that the real value corresponds to a region of the prior distribution with a lower probability in the second case. Nevertheless, this doesn't prevent the value to be correctly recovered.

Finally, it is remarkable that also the recovered earthquakes locations are characterized by notable differences for the models obtained by the Simulps13 tomography. The more notable effect is that the depth of the hypocenters is shifted downward because of the existence of the low velocity layer.

### 2.3 Comparison between Simulps and Rj-McMc results

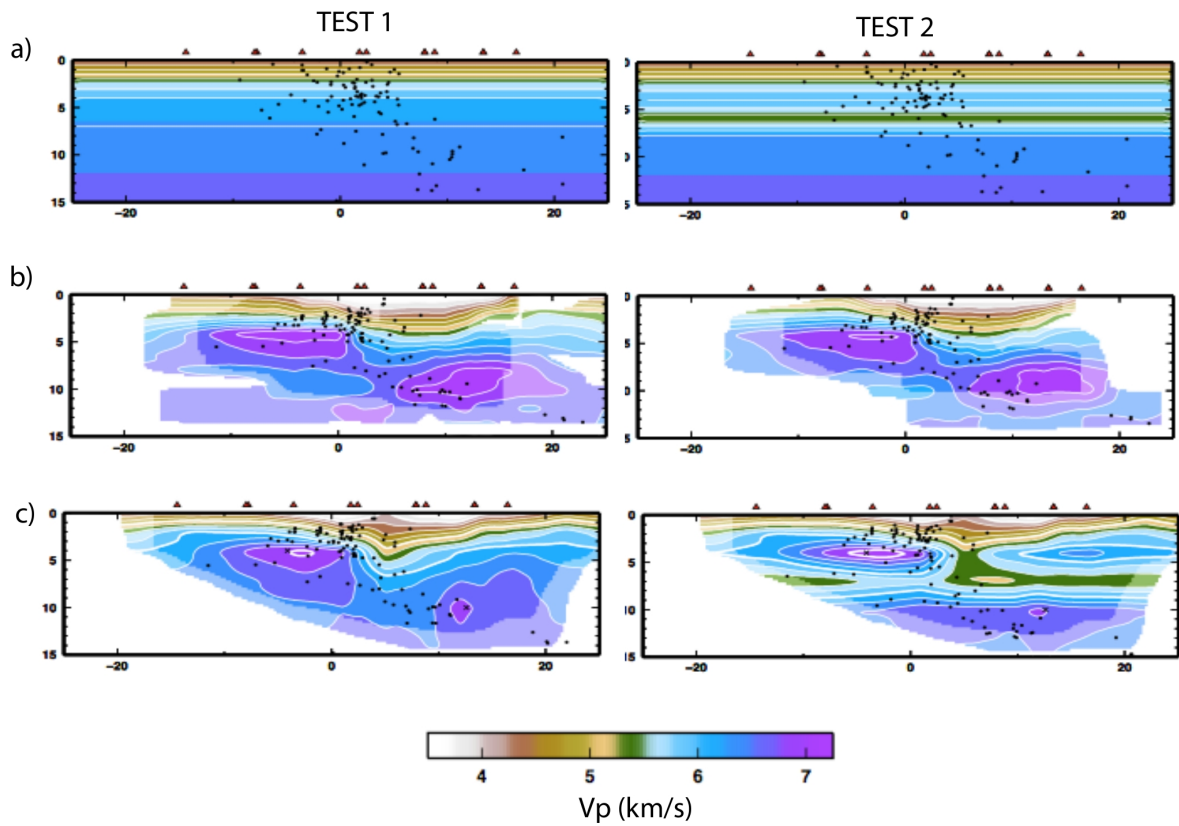


Figure 2.17: Vp structure and earthquake locations a) starting SIMULPS model and mean prior information for the Rj-McMc tomography; note that the two TESTs differ only for the low Vp channel at about 6 km depth, b) models obtained with the Rj-McMc code, c) models obtained with the SIMULPS code.



# 3 Rj-McMc LET of the Alto Tiberina Fault

The Alto Tiberina Fault (ATF) is the more recent and eastern one of the low-angle normal faults (LANs) that drives the regional scale evolution of the extensional basins in the northern Apennines (Figure 3.1; Piali et al., 1998; Chiaraluce et al., 2007; Collettini, 2011). LANs are recognized to accommodate extension of continental crust and are widely debated in the published literature (Wernicke, 1995, and reference therein) because of their unusual low dip compared to the typical rupture criteria (Anderson, 1951), which require a very weak detachment fault.

The potentially higher resolution at depth allowed by our new tomographic code (see the results of synthetic tests in Chapter 2) can provide new insights into the relationship between the seismicity distribution along the ATF and the rheological properties of the rocks intersected by the detachment. The deep velocity structure is still uncertain, mainly because of the low resolution at depth of the reflection seismic profiles.

More, the availability of high-resolution seismic reflection profiles and boreholes data provides the opportunity to test the reliability of the shallow velocity structure obtained with our new tomographic code.

Finally, the ATF is a possible target for an International Continental Scientific Drilling Program (ICDP) project aimed at drilling the fault in order to sample the fault core at seismogenic depths (Cocco et al., 2009) and our velocity model may provide suitable information for an intelligent drilling strategy.

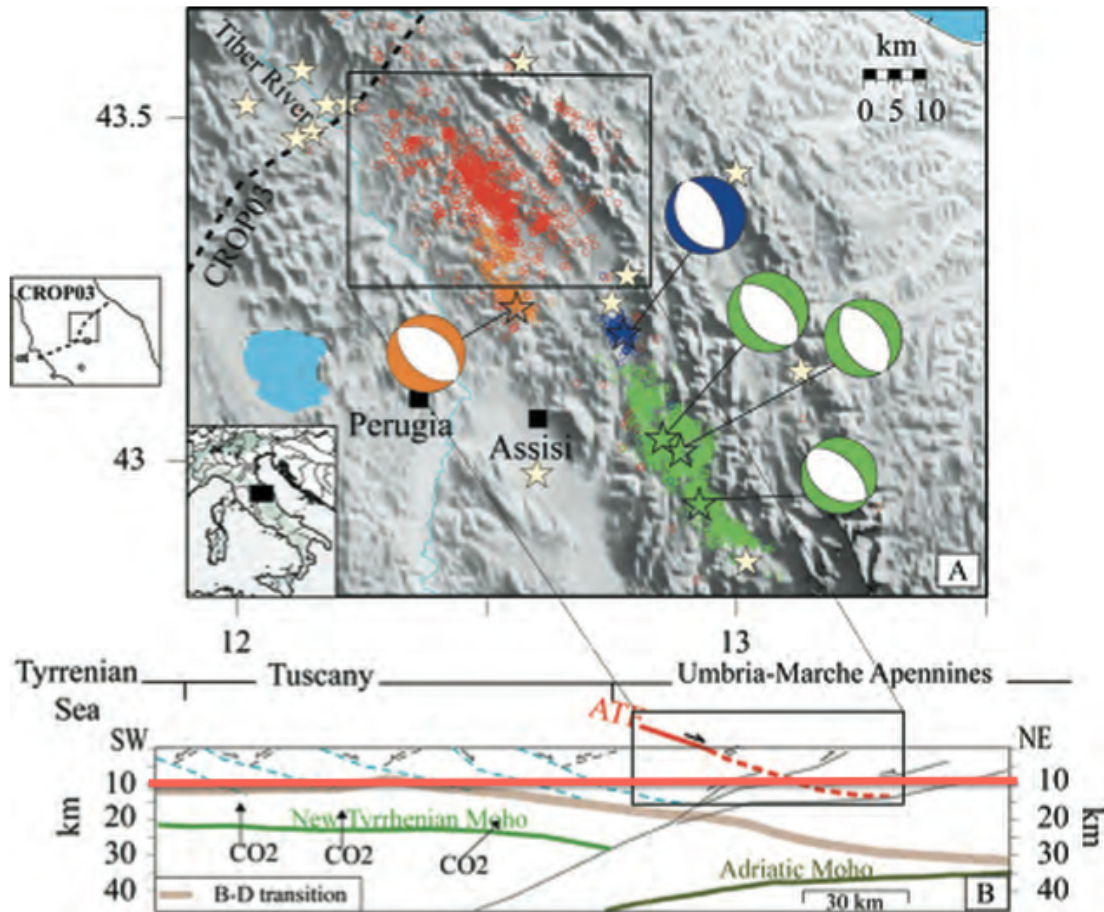


Figure 3.1: Top panel: relief map and seismicity distribution of study area. Red symbols show the epicenters of the earthquakes recorded during the 2000 – 2001 seismic survey (this study); Orange and blue symbols indicate the aftershocks of the 1984 Gubbio (Mw 5.1) and the 1998 Gualdo Tadino (Mw 5.1) earthquakes, respectively. Green symbols indicate the seismicity during the 1997 Colfiorito sequence, consisting of several normal faulting main shocks. Bottom panel: crustal-scale cross-section interpretation of the CROP03 seismic profile running from the Tyrrhenian to the Adriatic coasts (Barchi et al., 1998; Collettini and Barchi, 2004). The ATF is drawn in red, while other low-angle normal faults in the Tyrrhenian and Tuscany sectors are shown in blue. (Modified from Chiaraluce et al., 2007).

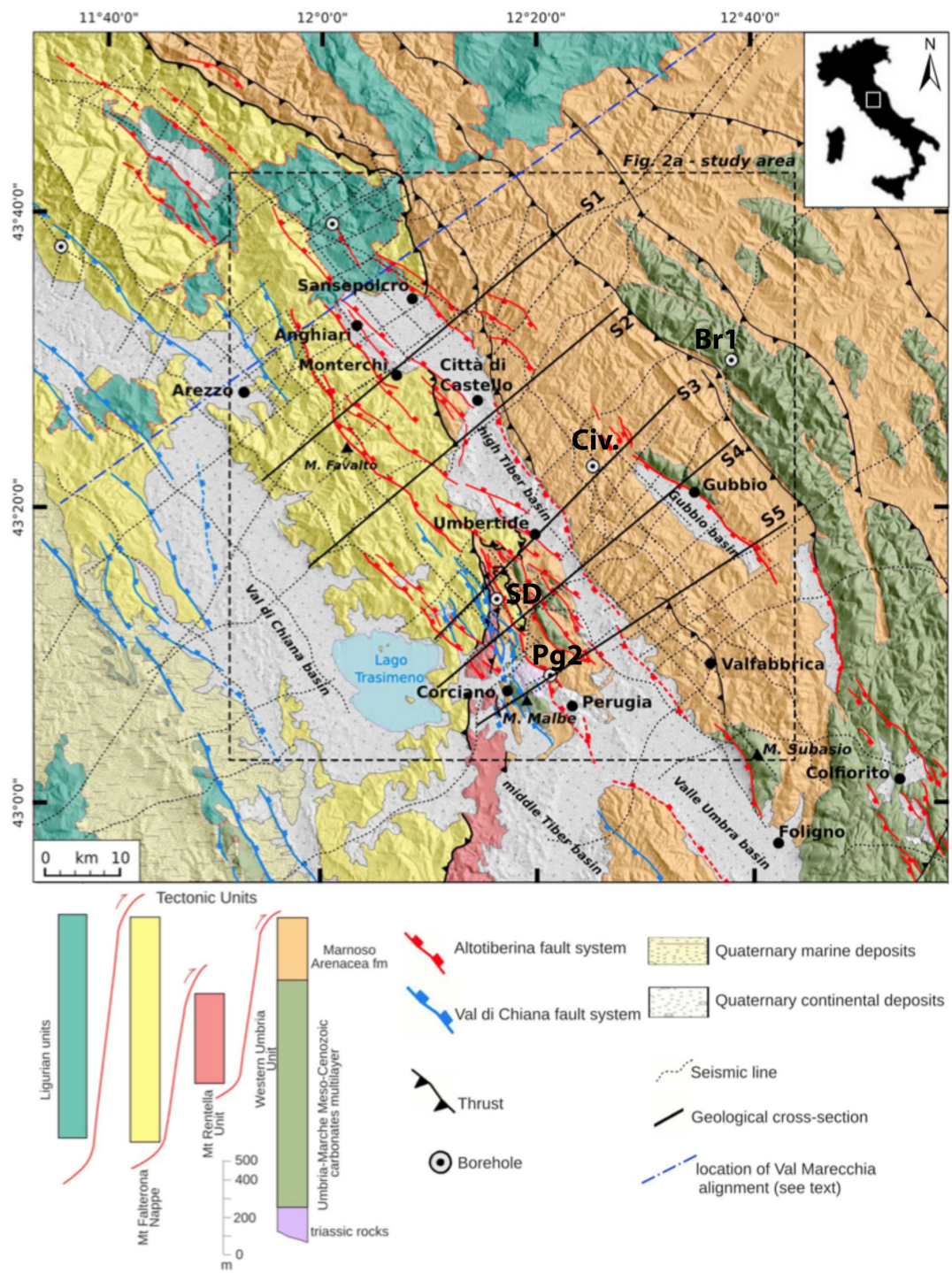


Figure 3.2: Geologic map of the study area (modified from Mirabella et al., 2011). White circles mark the boreholes sites: Mt. Civitello (Civ.), Burano 1 (Br1), Perugia2 (Pg), San Donato (SD).

### 3.1 Tectonic setting and velocity constraints

Since the Early Miocene, the Apennine belt has been characterized by the eastward migration of two NW-SE striking, active deformation belts, with compressional tectonic followed by a later extension (e.g., Barchi et al., 2006; Bonini and Tanini, 2009; Sani et al., 2009).

The main geological units in the investigated region belong to the Western Umbria Unit and from bottom to top consist of (Figure 3.2, Mirabella et al., 2011 and references therein): (i) late Paleozoic-middle-triassic clastic and metasedimentary rocks forming the top of the basement, (ii) late Triassic evaporites, (iii) lower Jurassic-Oligocene carbonates multilayer and (iv) Umbrian turbidites.

The Umbria unit is characterized by contractional structures at variable scales, the greater one involving the entire succession. Compressional structures are evident west of the Tiber valley, where a regional-scale thrust caused the doubling of the evaporitic and the underlying uppermost basement, as also testified by the stratigraphy found in Perugia2 and S. Donato boreholes. To the east, other thrust faults involve the Umbria Unit and are visible around the Calcareous ridge. The tectonic pile has been dissected by extensional deformation accommodated by a complex set of normal faults since the Pliocene. East-dipping and west-dipping high-angle normal faults have been generally interpreted as synthetic and antithetic secondary faults of the ATF system. The most important, both west-dipping, are the Gubbio and the Sansepolcro faults (e.g., Boncio et al., 2000; Barchi et al., 1999; Mirabella et al., 2004; Barchi and Ciaccio, 2009).

Borehole data provide useful constraints on the thickness and velocity of the main lithological units (see Mariucci et al., 2008 and references therein):

**The sedimentary succession** The Umbria sedimentary sequence, where not doubled, is about 4 km thick. The Quaternary continental sediments outcropping in the Tiber Valley and in the Gubbio and Sansepolcro basins have very low  $V_p$  ( $V_p < 3 \text{ km/s}$ ). The Miocene foredeep succession is characterized by  $V_p$  in the range 3.4-4 km/s, the carbonates multilayer has  $V_p$  in the range 5-6 km/s and higher velocity has been measured for the underlying Triassic evaporites formation that is about 1.5-2 km thick. As regard the evaporites, P-wave and S-wave velocities have been

measured on both outcrops and borehole samples (Trippetta et al., 2010). Both  $V_p$  and  $V_p/V_s$  show a strong variability, depending on the composition, pressure and fluids saturation. The average laboratory P-wave velocity is 6-7 km/s for dolostone, 4.6-5.3 km/s for gypsum–dolostone and 5.8-6.4 km/s for anhydrite ( $V_p$  is given at pressure ranging in between 0-100 MPa, corresponding to about 0-4 km).  $V_p/V_s$  ratios appear to be independent of confining pressure, with average values of 1.8 to 2.2 for sulphates and 1.9 to 2.2 for dolostone, respectively, for dry and saturated conditions.

**The basement** The uppermost sheet of the basement has been encountered at the base of the triassic evaporites in two boreholes (Perugia2 and San Donato, see Figure 3.2) and consists of phylladic and metamorphosed siliciclastic rocks. Borehole sonic log measurements indicate P-wave velocity in the range 4.8-5.2 km/s, significantly lower than the overlying evaporites. No S-wave velocity measurements are available. Nevertheless, both phyllites and metamorphosed siliciclastic rocks are expected to have low  $V_p/V_s$  ratio ( $<1.76$ , Christensen, 1996). The maximum thickness penetrated by the boreholes is 1.5 km but the real thickness is still unconstrained (Mirabella et al., 2008a,b). Boreholes have never reached the underlying crystalline basement and its nature is unknown. Refraction DSS data indicate that it is characterized by  $V_p$  values of about 6 km/s (Ponziani et al., 1995). Therefore, what we expected to image by tomographic investigation is a low velocity layer in between the high  $V_p$  triassic evaporites and the bulk crystalline basement.

**The ATF** The ATF bounds the western flank of the high Tiber Quaternary basin, is about 70 km long and dips NE-ward at an angle of  $15^\circ$ – $20^\circ$ . Its activity started at about 3 Ma and is documented in a large geological and geophysical dataset (e.g., Barchi et al., 1998; Boncio et al., 2000; Collettini and Barchi, 2002; Brozzetti et al., 2009), with the maximum offset, although not well-constrained, reaching about 4-8 km (Barchi et al., 1998; Mirabella et al., 2011).

The presently active extension is in the order of 2.5–3.0 mm/yr (D’Agostino et al., 2009), accommodated by moderate-magnitude earthquakes along high angle normal faults and by microseismicity (Piccinini et al., 2003; Chiaraluce et al., 2007) and creep (Hreinsdóttir and Bennett, 2009) along the ATF. The ATF appears not pro-

duce large earthquakes ( $M > 5.5$ ), at least in the past 2000 yrs., and is characterized by a diffuse seismicity (Collettini and Sibson, 2001; Chiaraluce et al., 2007). The ATF seismicity rate is high (about 3 events per day) and mainly constant with time, suggesting that the ATF releases stress continuously with time (Chiaraluce et al., 2007). More, the observed microseismicity is not enough to achieve the observed slip rate and part of the displacement must be accommodated a-seismically.

The weakness of the ATF can be partly explained by high pore fluid pressure, by the presence of phyllosilicates in the gouge or by a combined effect of the two because fluids-rocks interactions favor the development of the phyllosilicates (e.g., Collettini and Sibson, 2001; Collettini, 2011). It has been suggested that fault weakening can result from CO<sub>2</sub>-rich hydrous fluids reacting with the fault zone, causing a decrease in the friction coefficient and frictional-viscous creep along the fault (e.g., Holdsworth, 2004; Collettini and Holdsworth, 2004).

## 3.2 Rj-McMc tomography

### 3.2.1 Seismic data and networks

The arrival times data-set has been collected during an experiment run in 2000-2001 (Piccinini et al., 2003; Chiaraluce et al., 2007; Moretti et al., 2009) and consists of more than 2000  $M_L < 2.5$  earthquakes, which represents the background seismicity of the area, detected at 58 stations (Figure 3.3). From this dataset we selected 1262 events characterized by a back-azimuth gap less than  $150^\circ$ . The arrival time dataset consists of 14839 P-phases and 14343 S-wave phases.

We derived arrival times uncertainties from the SAC weighting scheme (0-4), by associating to these weights standard deviation of 0.025s (weight=0), 0.05s (weight=1), 0.1s (weight=2) and 0.3s (weight=3). Readings with SAC weight equals to 4 are discarded.

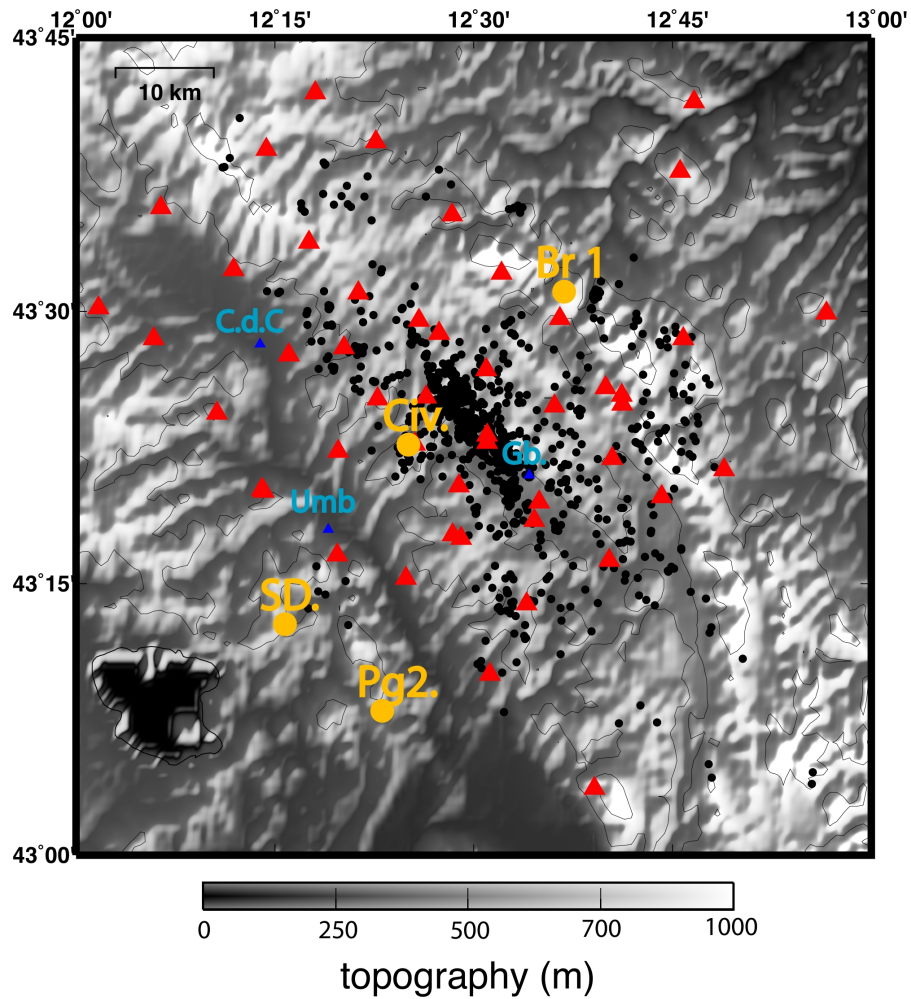


Figure 3.3: Relief map showing seismic stations (red triangles) and earthquakes (black points). Yellow circles mark the location of the Civitello (Civ.), Burano 1 (Br. 1), San Donato (SD) and Perugia2 (Pg2) boreholes. Blue triangles mark the main towns: Città di Castello (C.d.C.), Gubbio (Gb.) and Umbertide (Umb).

### 3.2.2 Prior information

We used Gaussian prior distributions for both velocity and earthquakes parameters. The prior model of  $V_p$  and  $V_p/V_s$  is the same used for the synthetic tests described in the Chapter 2. The background nodes grid is characterized by a vertical spacing of 1 km, down to 8 km depth, and 2 km at greater depth. The horizontal spacing is 2 km in both latitude and longitude directions. The background grid defines the maximum spatial resolution to be 2 km in the horizontal plane and 1 km in the vertical plane. The size of the model is 90 km in the  $xy$  plane and 16 km in the  $z$  direction.

Two prior Gaussian distributions (one for the  $V_p$  parameter and one for the  $V_p/V_s$  parameter) are associated to each one of the grid nodes. The mean prior values of earthquake parameters are the approximate locations obtained with Hypoellipse (Lahr, 1989) by Moretti et al. (2009). Approximate locations are used as prior information over the earthquake parameters in order to speed-up the convergence of the Rj-McMc sampling. Standard deviations are set equal to 1 km in latitude and longitude and 2 km in depth.

### 3.2.3 RjMcMc sampling of the PDF and data misfit

We run 20 Markov chains of about 300000 models/chain. After a burn-in phase of 200000 models/chain, when the sampling algorithm has been judged to have converged, we collected every 20th models/chain of the generated 100000 models/chain (Figure 4.6). Then, the total number of PDF samples is 100000. The recipe of sampling and the convergence assessment criteria are the same described in Chapter 2. The misfit level reached by the chains during the post burn-in phase is in the range 30000-34000. We estimated 4 parameters ( $x$ ,  $y$ ,  $z$ ,  $ot$ ) of 1262 events and 5 parameters ( $x$ ,  $y$ ,  $z$ ,  $V_p$ ,  $V_p/V_s$ ) of a number of Voronoi's cells in the range 800-1100 (Figure 4.7), depending on both the chain and the individual model. Since the total number of estimated parameters is in the range 9000-10500 and the number of data is 29182, this misfit level corresponds to a normalized  $\chi^2$  misfit measure in the range 1.5-1.8.

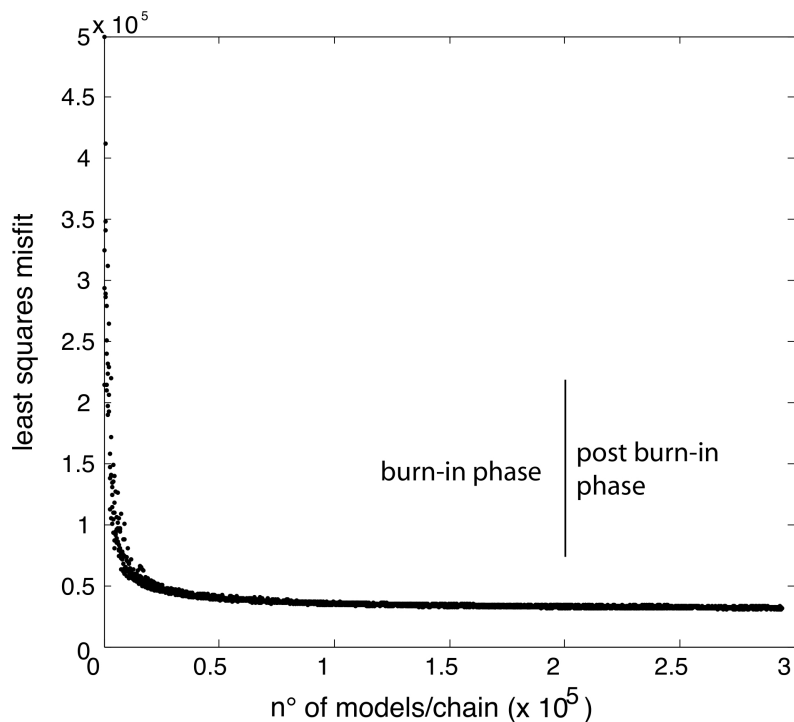


Figure 3.4: Misfit evolution during the Rj-McMc sampling.

The 1D marginal PDFs for each one of the sampled parameters are derived from the ensemble of PDFs collected models. In the following discussion we analyze and discuss mean and standard deviation values related to every model parameters. As previously described, the individual models characterized by different Voronoi's tessellation are all rasterized on the regular grid and the mean and standard deviation value of the 1D marginal PDFs over the velocity parameters ( $V_p$  and  $V_p/V_s$ ) are computed for each one of the grid nodes. If the posterior standard deviation is less than the prior standard deviation, some new information over the model parameter is added by the data to the prior information. Otherwise, if the posterior standard deviation is less or equal the prior, no additional information has been added to our a-priori knowledge of the model parameter. We interpret  $V_p$  and  $V_p/V_s$  anomalies with standard deviation less than 0.4 km/s and 0.07, respectively.

As regard the event parameters, the posterior standard deviations are always less than the prior standard deviations for all the 4 hypocentral parameters. Posterior standard deviations amount to 80-150 m for event latitude and longitude and 200-

### 3 Rj-McMc LET of the Alto Tiberina Fault

500 m for event depth. About 50 earthquakes have posterior standard deviation of at least one of the hypocentral coordinates greater than 0.5 km and are not shown in the Figures.

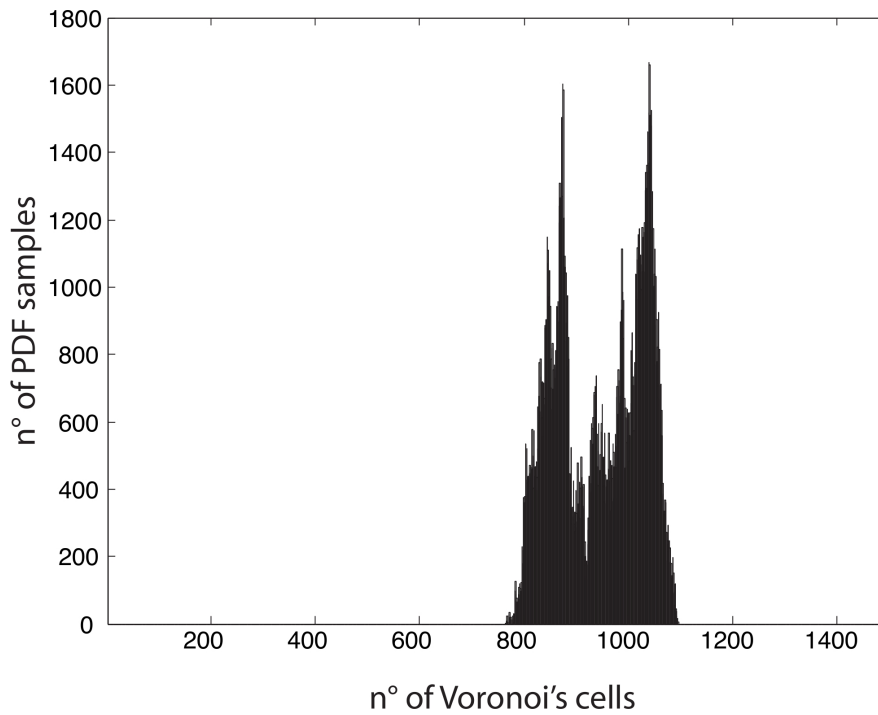


Figure 3.5: 1D marginal PDF describing the sampling of the number of Voronoi's cells. The prior distribution is uniform in between 1 and 1500.

### 3.2.4 Discussion on the $V_p$ and $V_p/V_s$ mean posterior models

**$V_p$  and  $V_p/V_s$  horizontal cross-sections** The shallower  $V_p$  structure (1 km depth, Figure 4.8) is strongly correlated to the rocks outcropping in the area. The basins hosting Quaternary continental deposits (Tiber, Gubbio and Sansepolcro basins) are characterized by very low  $V_p$  ( $<3.5$  km/s). The low  $V_p$  correlates with relatively high  $V_p/V_s$  and the higher  $V_p/V_s$  anomalies are found in the Gubbio and Sansepolcro basins, bounded to the east by high-angle west-dipping normal faults. Conversely, the higher  $V_p$  is found below the NW-SE-trending carbonatic ridge ( $V_p=5-5.7$  km/s) and in the SW part of the model, well matching the geometry of the outcropping carbonates.

The most seismicity down to 5 km depth occurs in a region of  $V_p/V_s > 1.9$  and  $V_p$  of about 5.5-6.0 km/s. At 3 km depth the hypocenters are distributed along two parallel NW-SE alignments (3 km depth, 4.8). The eastern one is approximately located below the northern sector of the mapped Gubbio fault.

The NW-SE-elongated high  $V_p$  belt found below the Calcareous ridge is visible down to about 7 km (Figure 4.9). More discontinuous high  $V_p$  anomalies are present also in the SW region of the resolved model. At greater depth there is an evident separation between low  $V_p$  to the north and high  $V_p$  to the south, with the velocity difference increasing at increasing depth.

The most hypocenters below 5 km depth are located in low  $V_p$  regions and define NW-SE alignments facing the high  $V_p$  belt. At increasing depth the  $V_p/V_s$  decreases on average, higher  $V_p/V_s$  regions are correlated with higher  $V_p$  regions and lower  $V_p/V_s$  regions are correlated with lower  $V_p$  regions.

**Across-ATF  $V_p$  and  $V_p/V_s$  cross-sections** The cross-sections a and b in Figure 4.10 allow a straightforward correlation between seismic velocity, borehole data and seismic reflection profiles. Our  $V_p$  model near the Burano1 well is consistent with the sonic log measurements of the evaporites encountered at 600 m depth ( $V_p=5$  km/s, Trippetta et al., 2010). The up warping of the contour lines highlights the compressional structure beneath the Calcareous ridge and is consistent with both the seismic profile by Tavani et al. (2008) (supplementary Figure 3.16) and the location of the outcropping carbonates.

### 3 Rj-McMc LET of the Alto Tiberina Fault

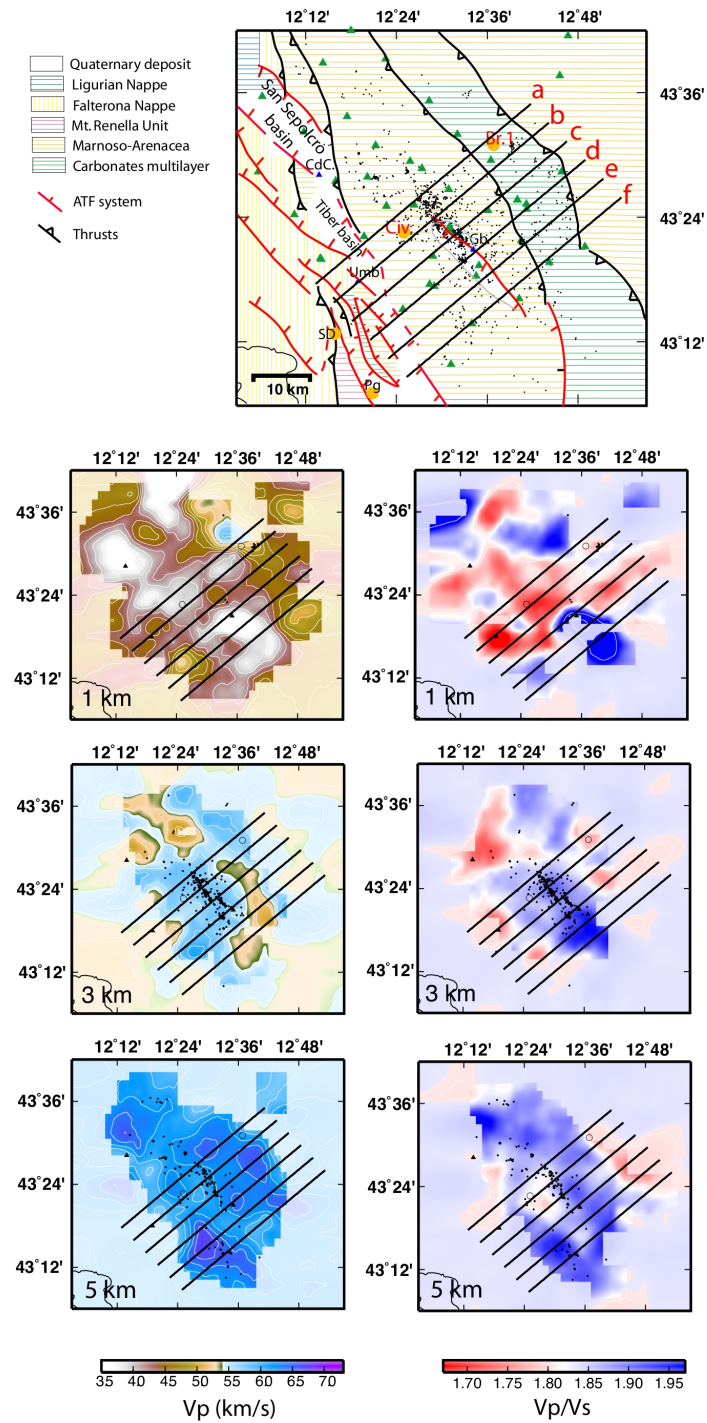


Figure 3.6:  $V_p$  (left panels) and  $V_p/V_s$  (right panels) on horizontal cross-sections at 1, 3 and 5 km depth. Full color regions are areas where the posterior standard deviation is less than the prior standard deviation (see supplementary Figure 4.19).

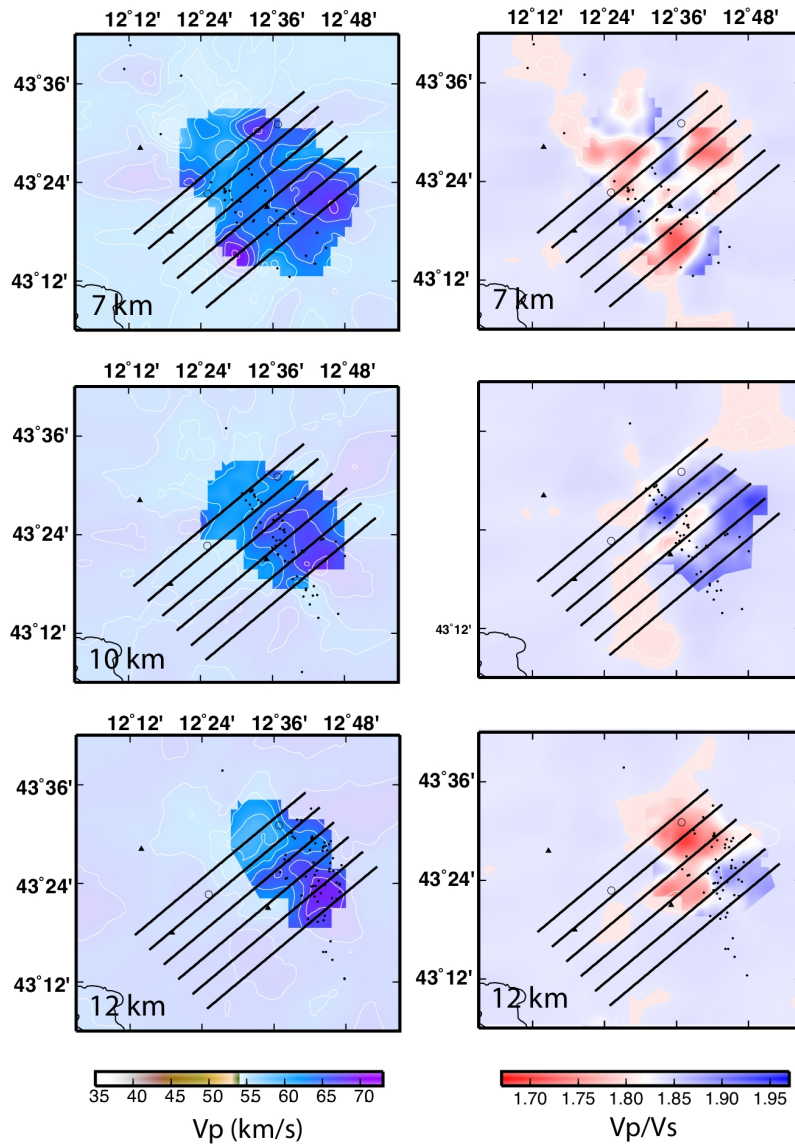


Figure 3.7: Same of Figure 4.8 for horizontal cross-sections between 7 and 12 km depth. Full color regions are areas where the posterior standard deviation is less than the prior standard deviation (see supplementary Figure 4.20)

The Mt. Civitello well penetrates the top of the Marne a fucoidi formation at about 800 m depth and the evaporites layer at 2.2 km depth (see supplementary Figure 3.14). Our Vp model shows constant velocity of 3.8-4 km/s down to 1 km, a steep velocity gradient in between 1 and 2 depth and a Vp in the range 5.5-6.2 km/s down to the base of the well (about 5 km). The Vp values are consistent with log data for the Marnoso Arenacea formation. It is about 0.5 km/s lower than the sonic log (-9%) for the carbonates multilayer and about 0.25 km/s on average lower for the triassic evaporites (-4%). Standard deviations are in the range 0.15-0.25 km/s. Our model detects the steep velocity gradient between the Marnoso Arenacea formation and the carbonates multilayer but has clearly too low vertical resolution to recover a change of 1.5 km/s in less than 0.5 km. The discrepancy between velocity data and sonic log measurements are in the order expected for the different frequency of investigation and the occurring of velocity dispersion. Velocity dispersion in the seismic and sonic frequency bands is substantial (about 5-10% as minimum), except for the cases of dry rocks or 100% saturated rocks (Batzle et al., 2006 and references therein).

Moreover, the different units encountered by the Mt. Civitello well show peculiar Vp/Vs ratio. The turbiditic formation has generally very low Vp/Vs (<1.75) that can be explained by the main siliciclastic composition. The higher Vp/Vs (1.85-1.90) is found within the evaporite formation and corresponds to values found in not fluid saturated evaporites (Trippetta et al., 2010). Intermediate values are found for the Carbonates multilayer.

On the base of the constraints derived by borehole data and seismic profiles (Mirabella et al., 2004; 2008; 2011, see also supplementary Figure 3.15), we extrapolated the location in our model of the top of the carbonates multilayer and the top of the evaporites formation. The shallow Vp structure (0-4 km) shows similar features in all the six cross-sections, highlighting the folded and faulted structure of the Umbria sedimentary sequence. The down warping of the Vp contour lines reveals the SW-ward displacement related to the Gubbio fault, while the up warping of the contour lines delineates the thrust tectonic below the Calcareous ridge.

Conversely, the Vp/Vs model at shallow depth shows notable variation between the different cross-sections. In the northern sections (a-c, Figure 4.10) the Vp/Vs appears to be directly related to the lithology, as already described for the Mt.

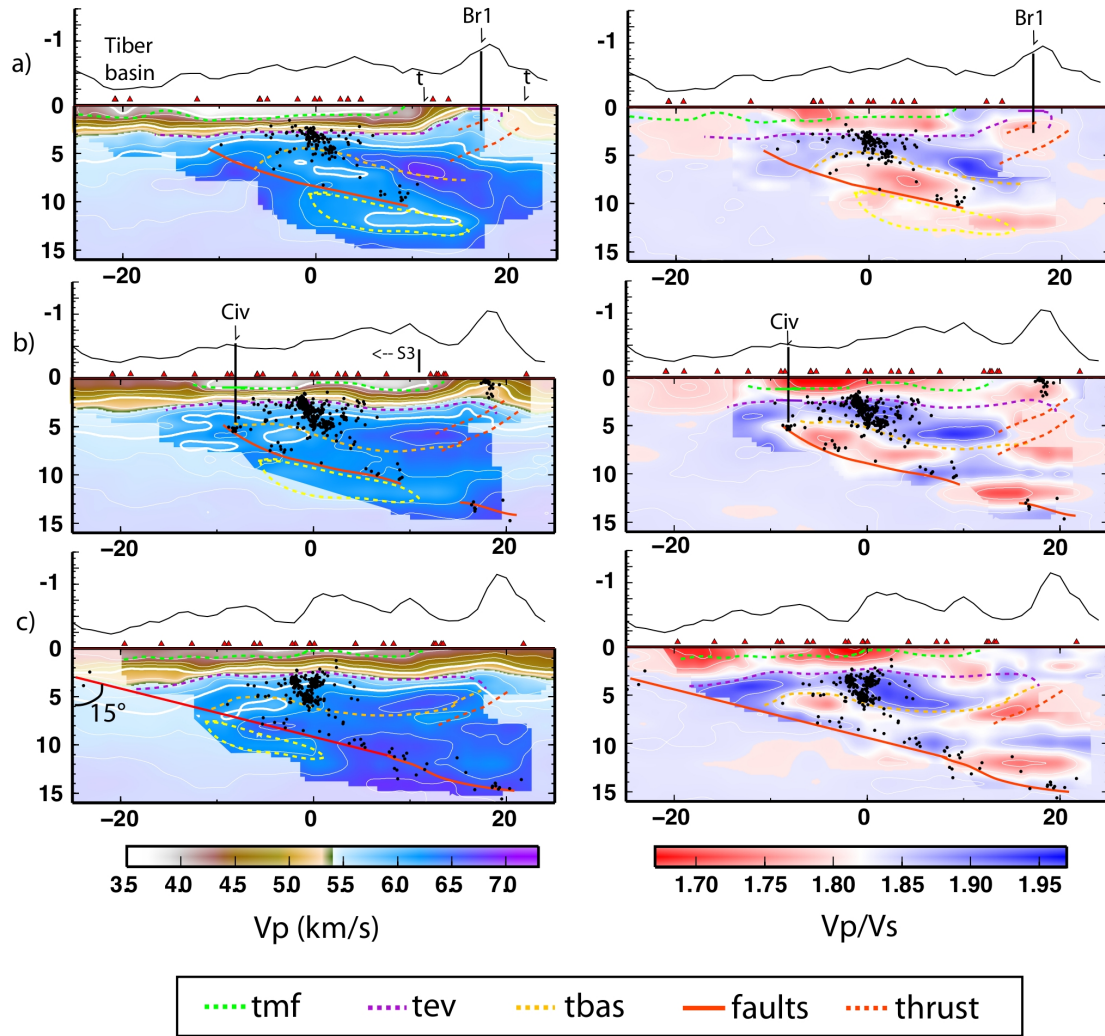


Figure 3.8: Mean  $V_p$  (left panels) and  $V_p/V_s$  models (right panels) plotted on vertical cross-sections. See Figure 4.8 for the locations. Full color regions are areas where the posterior standard deviation is less than the prior standard deviation.

3 *Rj-McMc LET of the Alto Tiberina Fault*

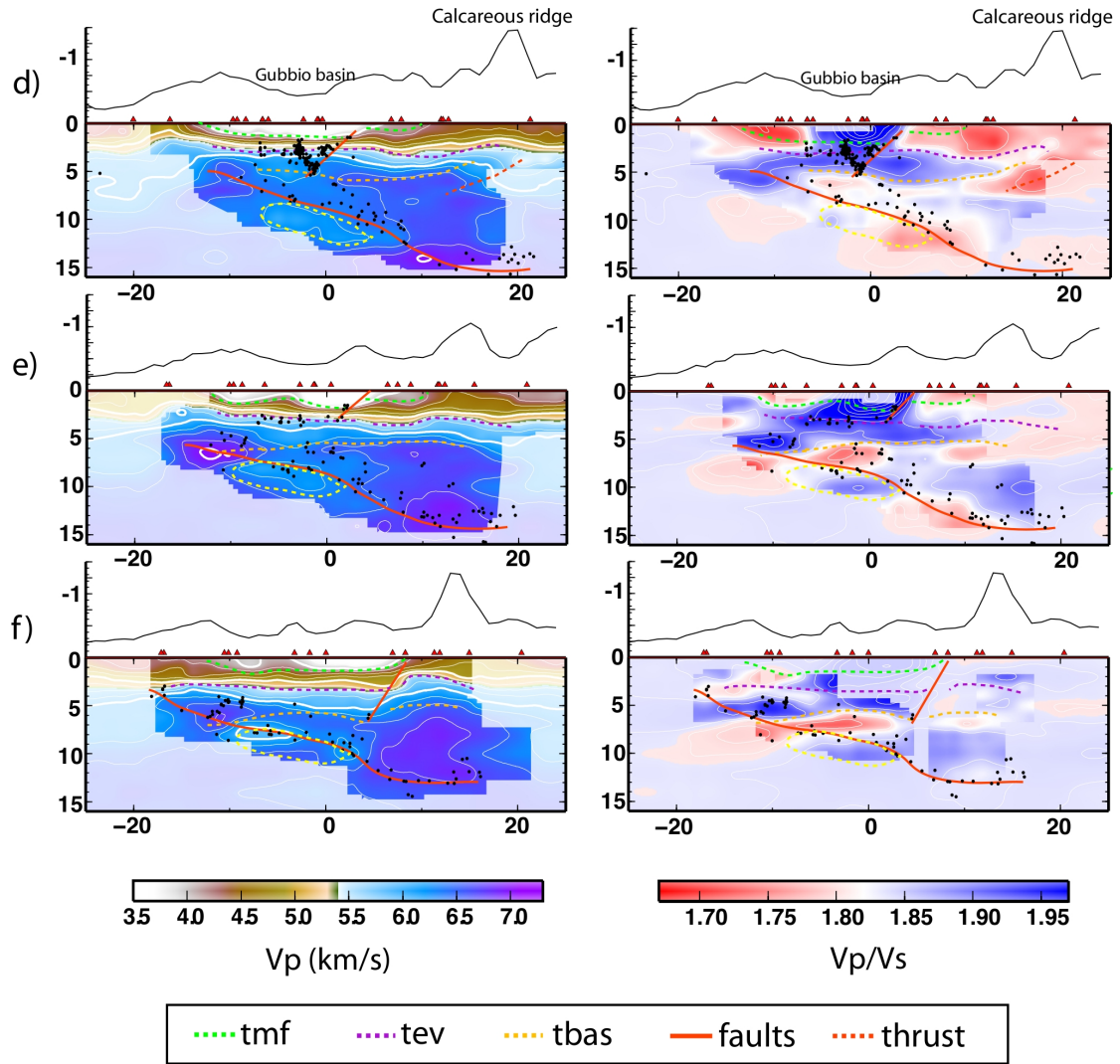


Figure 3.9: Mean  $V_p$  (left panels) and  $V_p/V_s$  models (right panels) plotted on vertical cross-sections. See Figure 4.8 for the locations. Full color regions are areas where the posterior standard deviation is less than the prior standard deviation.

Civitello well stratigraphy. In the southern sections (d-e, Figure 3.9), a strong high  $V_p/V_s$  ratio ( $>1.95-2.2$ ) is found to the west of the Gubbio fault from surface to about 4-5 km depth. The micro-seismicity delineates the Gubbio SW-dipping high-angle normal fault and also a NE-dipping high-angle synthetic fault (see section d). A similar high  $V_p/V_s$  ratio has been previously found in the hanging wall of the high-angle normal faults of the northern Apennines (Chiarabba and Amato, 2003; Moretti et al., 2009; Chiarabba et al., 2009) and was interpreted as being the result of a up-ward fluid migration during major earthquakes, which nucleated within the evaporites unit (Miller et al., 2004; Mirabella et al., 2008). More, the presence of overpressured fluids inside the low permeability evaporites unit is thought to favor the reactivation of the high angle normal faults in the region (Chiaraluce et al., 2003). Consistently, the shallow cluster of seismicity occurs within the high  $V_p/V_s$  evaporites unit in all the six sections but only in the sections across the Gubbio fault the  $V_p/V_s$  is very high and extends up to the ground surface.

The depth of the top of basement is the more questionable. Seismic reflection and borehole data suggest that the top of the low  $V_p$  basement is located at about 5-7 km depth. We performed a synthetic test similar to those described in Chapter 2, in order to understand what is the minimum resolvable thickness of the inferred low  $V_p$  upper sheet of basement. The results (see supplementary Figure 3.17) show that we are able to resolve a low  $V_p$  layer of minimum thickness of about 1.5 km. Since the evaporites formation is the only lithological unit for which the  $V_p/V_s$  ratio has been estimated for a wide range of composition, fractures and fluids pressure (Trippetta et al., 2010), and the  $V_p/V_s$  ratio is always  $> 1.8$ , we attempted to locate the evaporites-basement interface across the entire resolved model by considering the  $V_p/V_s=1.80$  contour line. In this way we found a good correlation with the top of the basement inferred from the migrated seismic reflection profiles (Mirabella et al., 2004; 2008; 2011). We suggest that regions where a velocity reversal occurs and very low  $V_p/V_s$  correlates with low  $V_p$ , correspond to the philladic or siliciclastic uppermost sheet of basement (i.e. the acoustic basement, more visible in the cross-sections a-c), whereas the normal-to-low  $V_p/V_s$  regions correlated with high  $V_p$  correspond to the crystalline basement which composition is still unknown (more visible in the cross-sections d-f). An outcome of the suggested location for the top of the basement is that the evaporites unit is at least doubled by thrust tectonic

below the Calcareous ridge. Otherwise, the top of the basement should be located shallower, inside the high  $V_p/V_s$  region. We don't exclude this second hypothesis. What is notable is that our  $V_p/V_s$  model provides a useful constraint on the maximum thickness of the evaporites layer at depth.

The inferred top of basement corresponds also to a strong decrease in seismicity, in agreement with the existence of basement rocks that are weaker than the overlying brittle dolostone. More, the low  $V_p$  and  $V_p/V_s$  basement underlying the shallow seismicity defines a lens-shaped NE-dipping structure similar to the lens-shaped structure formed by a package of reflectors identified in the CROP03 profile (Barchi et al., 1998) and associated to an extensional duplex.

**Seismicity along the ATF detachment** Our velocity model provides a unique opportunity to address the relationship between seismicity distribution and velocity structure, adding new information to previous analyses of ATF seismicity (Piccinini et al., 2003; Chiaraluce et al., 2007; Moretti et al., 2009). The hypocenters along the ATF detachment don't define a narrow planar fault, but rather they diffuse into a ca. 1.5-2 km thick region, too thick to be considered as a single detachment plane. Since we plotted only hypocenters with depth error (i.e. standard deviation) less than 0.5 km, it seems unlikely that this can be due entirely to errors in hypocenter locations. More, the average dip is about  $15^\circ$  but the hypocenter distribution shows a staircase geometry.

The NE-dipping alignment of hypocenters is not highlighted by a simple pattern of  $V_p$  and  $V_p/V_s$  anomalies. On the base of a widespread low  $V_p/V_s$  anomaly, Moretti et al. (2009) suggest the existence of CO<sub>2</sub>-saturation in the rock volume around the ATF and that the detachment acts as an impermeable barrier to deeper fluids from the crust. This interpretation mainly derives by the following evidences: i) CO<sub>2</sub> local over-pressure is able to explain the weakness of the ATF and the occurrence of microseismicity (Collettini and Barchi, 2002; Chiaraluce et al., 2007); ii) CO<sub>2</sub>-overpressure has been found at 4-5 km within the evaporites in two deep boreholes (Perugia2 and San Donato) located in the footwall of the ATF (Chiodini et al., 2004; Heinicke et al. 2006); iii) a very low permeability has been found in the fault core of the Zuccale fault, an older analogue to the ATF (Collettini et al., 2006). It is reasonable to suppose that if the ATF acts as an impermeable barrier, the

evidences of fluid overpressure should concentrate in the footwall and not all around the fault. Strikingly, in our velocity model the most footwall volume of the ATF is characterized by a low  $V_p$  (dashed yellow contour line in Figures 4.10 and 3.9), corroborating the existence of fluid overpressure in the footwall of the fault. The increase in pore pressure increases the porosity volume of the rocks at low effective stresses and, consequently, both the  $V_p$  and  $V_s$  decrease. The relative decrease of  $V_p$  and  $V_s$ , and thus the change in  $V_p/V_s$  depends, on fluid phase, saturation and pore geometry (e.g., Dvorkin et al., 1999; Takei, 2002; Wilkens et al., 2004). In our model the low  $V_p$  correlates with relatively high  $V_p/V_s$ . We are not confident in the reliability of the  $V_p/V_s$  found in the footwall because all the ray-paths are parallel to the ATF, i.e. likely parallel to the fabric of the rocks and can be biased by anisotropic effects (Wang et al., 2012).

The low  $V_p$  in the footwall of the ATF is visible in all the six cross-sections but it vanishes in the deeper part of the ATF, in correspondence of a very high  $V_p$  body. In correspondence to the same high velocity body, the hypocenters distribution flattens to horizontal. The nature of this body is unknown and the cause of the flattening is difficult to unravel. Nevertheless, the spatial correlation is notable and points to a link between the change in the dip and a rheological transition in the rocks intersected by the ATF.

All these evidences point to a complex architecture of the ATF, with deformation distributed within a wide and thick fault zone, where fluids play a key role and with rocks adjacent to the fault characterized by different rheological properties.

### 3.3 Comparison with previous models

The dataset used in this study has been already inverted with the Simulps code by Moretti et al. (2009). In addition, we performed a second linearized inversion with a different Vp starting model, which lacks of the velocity reversal existing in the starting Vp structure by Moretti et al. (2009). A second difference is in the model parameterization, with a vertical spacing of 2 km instead of 3 km. The two solutions are quite similar in the well-resolved region of the model, whereas some differences exist in poor resolved regions, where the respective starting reference models affect the two models. In Figure 3.10 the two Simulps solutions are compared with the model obtained with our new code.

The three Vp models share the main Vp anomalies: (i) the up-warping of the contour lines below the Calcareous ridge and the underlying high Vp body (anomaly A), (ii) the velocity reversal below the Mt. Civitello borehole (anomaly B), (iii) the up-warping of contour lines to the NE of the Mt. Civitello well. Anomaly A is a different depth in the two Simulps solutions and is more intense in the model by Moretti et al. (2009). The reason can be found in the different parameterization and different starting models used in the inversion, as shown in Chapter 2. The main differences between the Simulps and the Rj-McMc Vp models are in the shallower structure. The Rj-McMc model is more consistent with sonic-log data from the Mt. Civitello well and reveals the steep Vp gradient in correspondence of the transition between the Marnoso-Arenacea formation and the Carbonates multilayer. The fixed parameterization prevents to detect steep velocity gradients. Similarly, the up-warping of the Vp contour lines is more evident in the non-linear solution and the Vp at the surface is higher, consistent with the outcropping carbonates.

The Vp/Vs models show more notable differences. The two models obtained with the Simulps code show strong differences where their respective starting Vp models differ (see the region below the anomaly A). The lower Vp/Vs ratio in model by Moretti et al. (2009) may be reliable or it may be partially caused by the lower Vp existing in the starting model in between 4.5-7.5 km. Moreover, both the models lack of visible difference between the shallow Marnoso-Arenacea formation and the underlying carbonates and evaporites formations found in the model obtained with the Rj-McMc code.

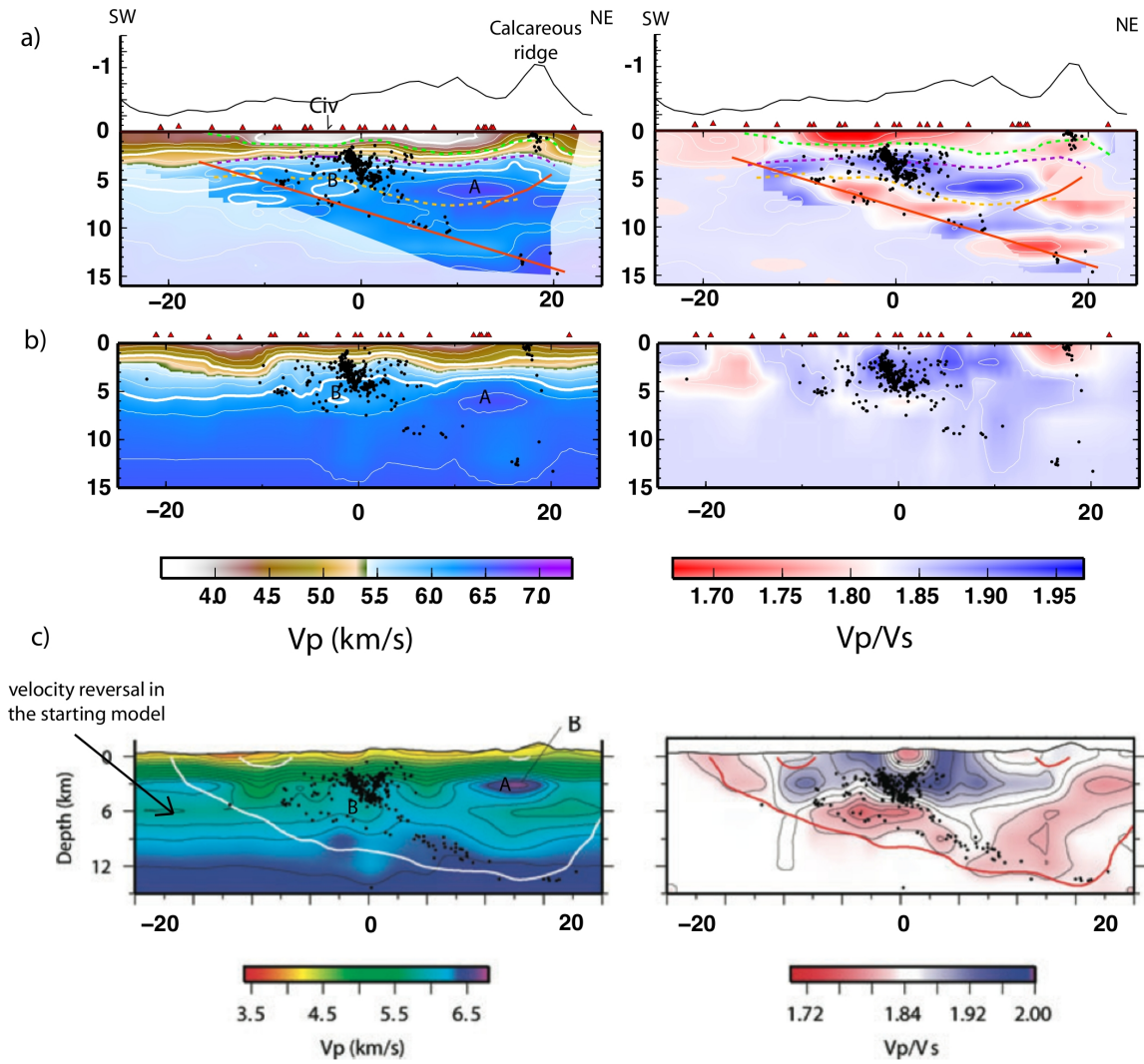


Figure 3.10: Comparison between models obtained with the Rj-McMc code (a) and with the Simulps code (b-c). b) our best Simulps solution; c) solution by Moretti et al. (2009).

Finally, we compared the data misfit in the two models. In the model obtained with the Rj-McMc code, the data misfit is computed by considering the mean posterior model for both the earthquake parameters and the velocity parameters. We use the simple least square data misfit ( $\phi = \sum_i ((d_i^{obs} - d_i^{calc})/\sigma_i)^2$ ) for the comparison because it doesn't depend on the data weighting scheme, which is different between the two inversion methods. It depends only on data uncertainties, which

### 3 Rj-McMc LET of the Alto Tiberina Fault

have been defined on the base of the SAC weights: standard deviations of  $0.025s$  (weight=0),  $0.05s$  (weight=1),  $0.1s$  (weight=2) and  $0.3s$  (weight=3). The data misfit is much higher for the model obtained with Simulps (Rj-McMc model:  $\phi_p = 15000$ ;  $\phi_s = 18000$ ; Simulps model;  $\phi_p = 22000$ ;  $\phi_s = 67000$ ), with the greater difference found for the S-wave data. The histograms of P and S arrival-time residuals are shown for both the two different models in Figure 4.17.

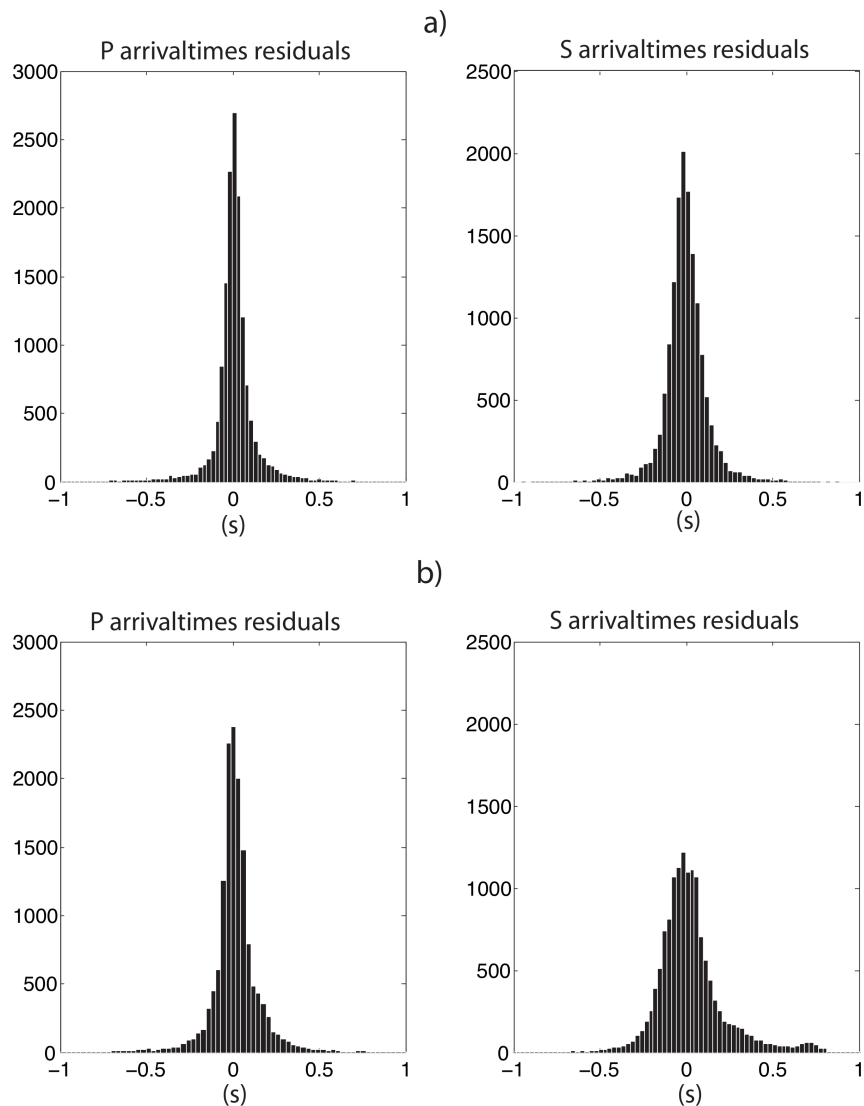
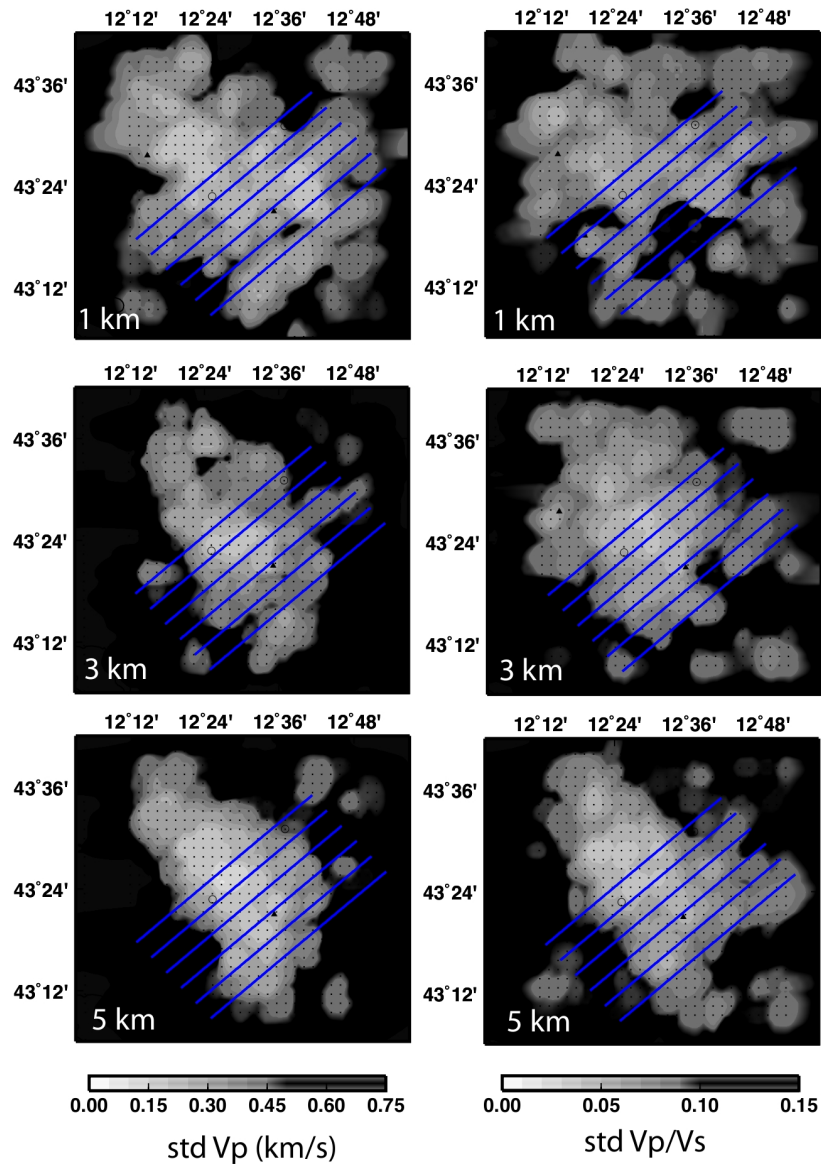


Figure 3.11: P- and S- residuals between observed and theoretical arrival times; a) theoretical arrival times computed in the Rj-McMc model, b) theoretical arrival times computed in Simulps model.

## Supplementary Figures

Figure 3.12: Standard deviations of the  $V_p$  (left panels) and  $V_p/V_s$  (right panels)

3 Rj-McMc LET of the Alto Tiberina Fault

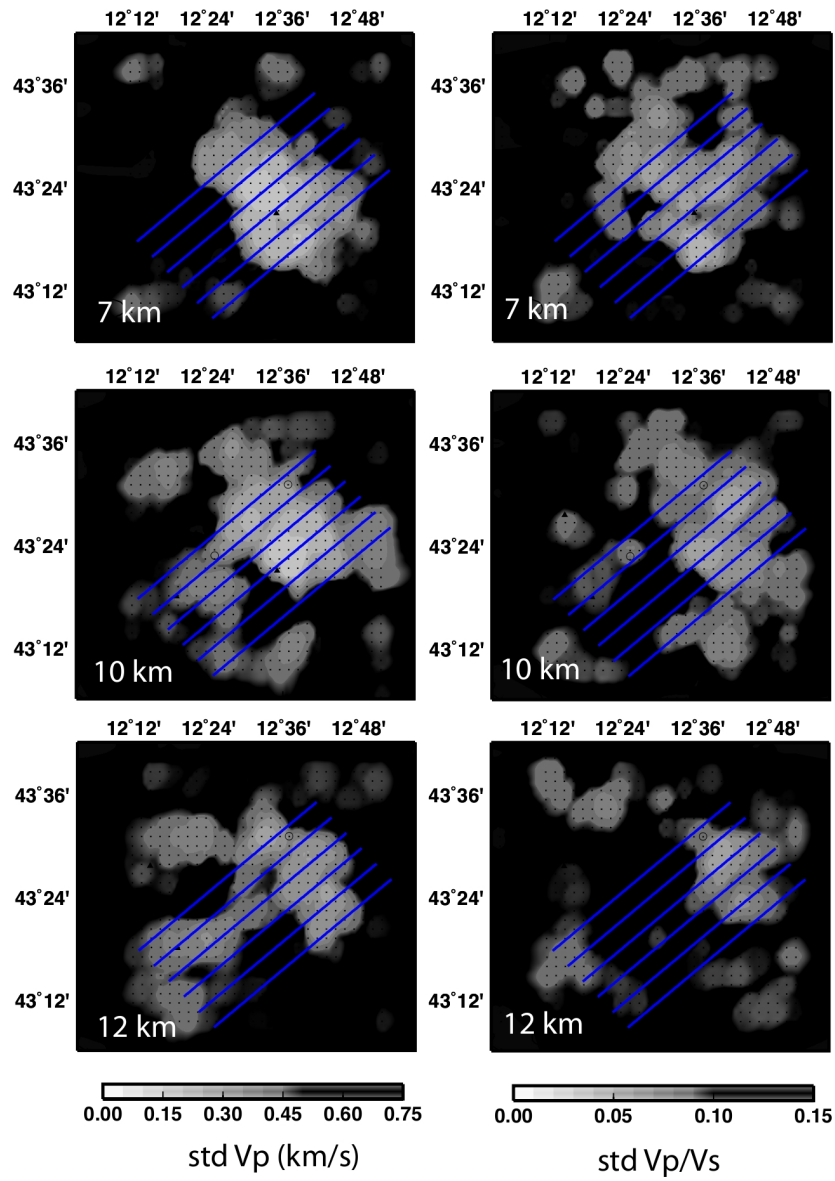


Figure 3.13: Standard deviations of the Vp (left panels) and Vp/Vs (right panels) of the grid nodes at 7, 10 and 12 km depth.

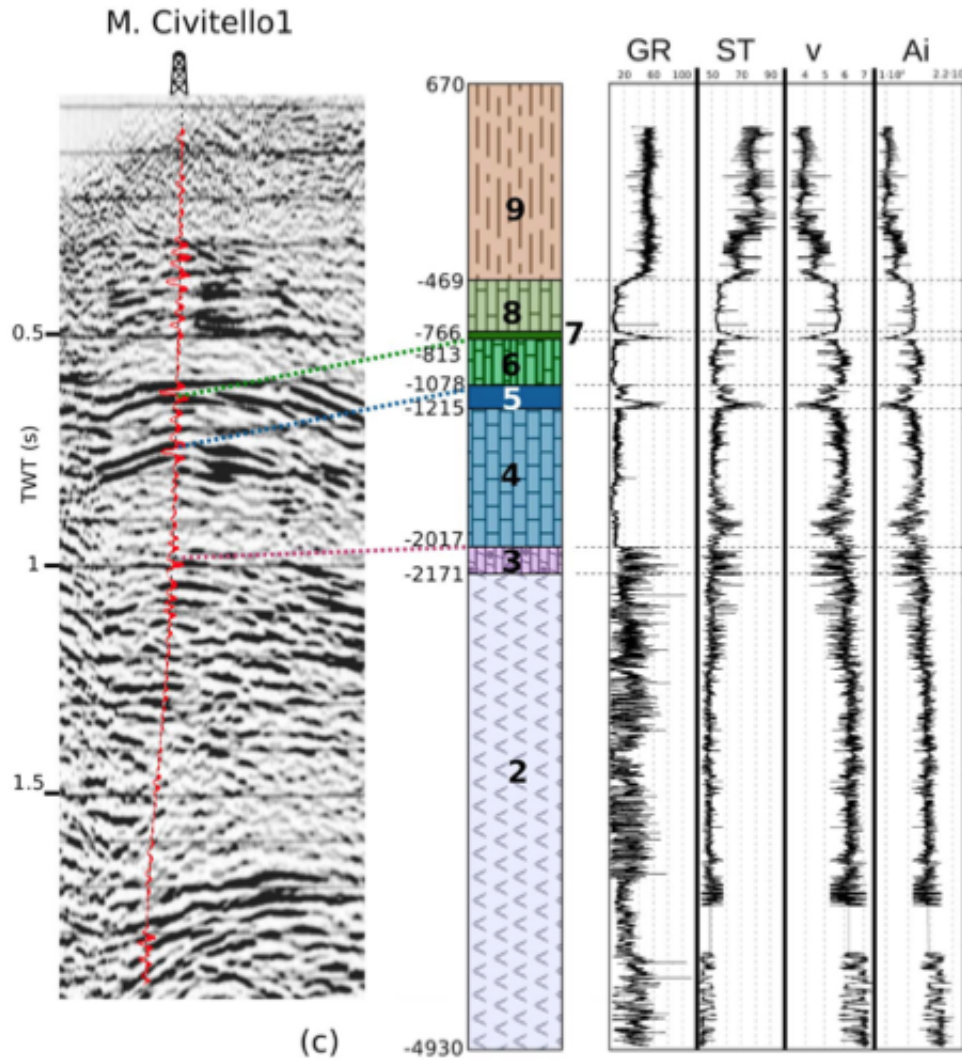


Figure 3.14: Mt. Civitello seismic image, geological sketch and log data. Numbered units are: 2) late Triassic evaporites, 3) transitional facies between the evaporites and the Calcare Massiccio formation (Lias); 4) Calcare Massiccio formation; 5) marly carbonates; 6) pelagic carbonates (Maiolica formation); 7) Marne a Fucoidi formation; 8) upper Cretaceous-Oligocene carbonates (Scaglia formation); 9) Marnoso Arenacea formation. (Modified after Mirabella et al., 2011)

### 3 Rj-McMc LET of the Alto Tiberina Fault

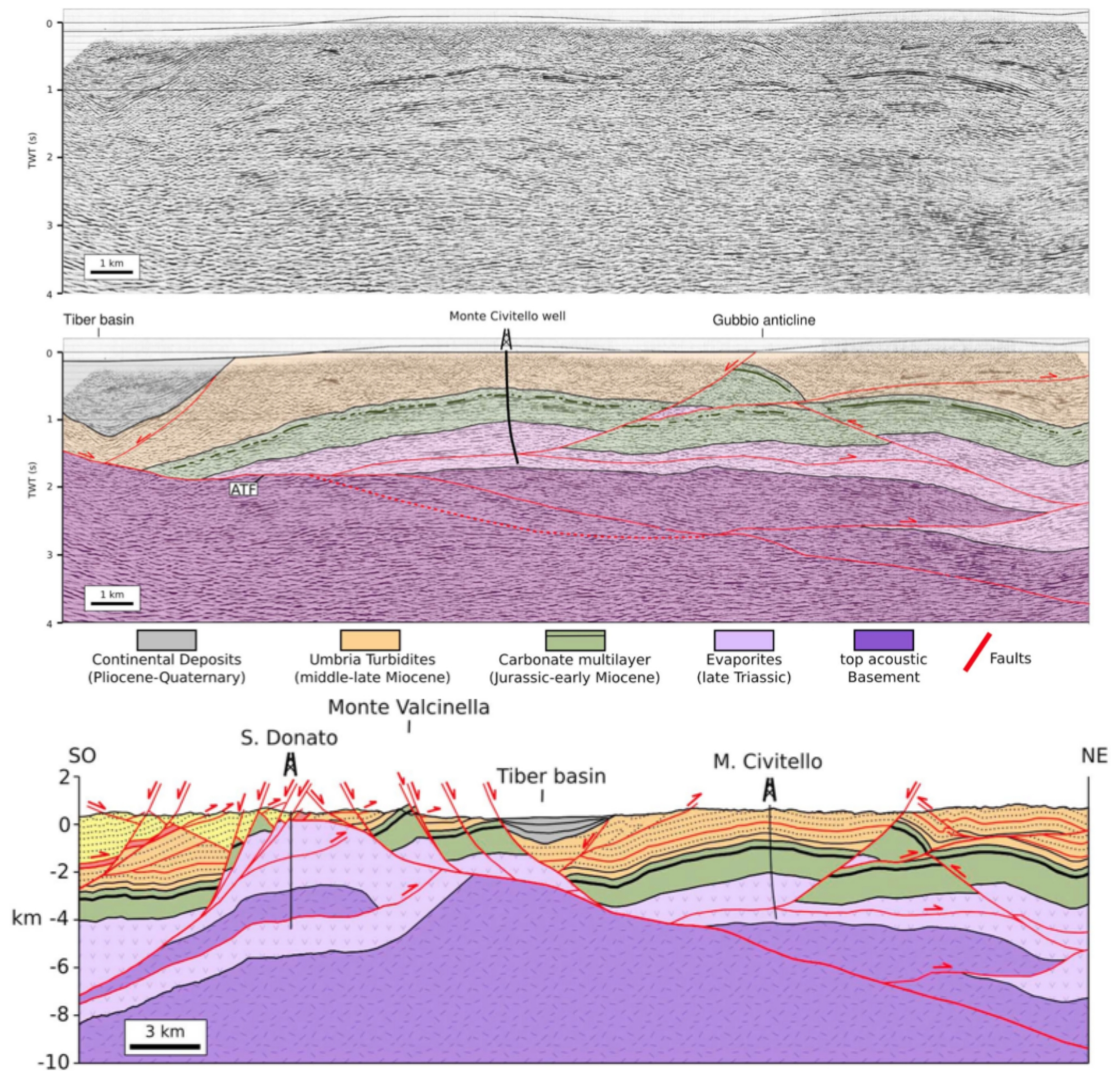


Figure 3.15: Original seismic profile (top panel), interpreted profile (central panel) and migrated section (bottom panel) by Mirabella et al. (2011). For the location see profile S3 in Figure 3.2.

### 3.3 Comparison with previous models

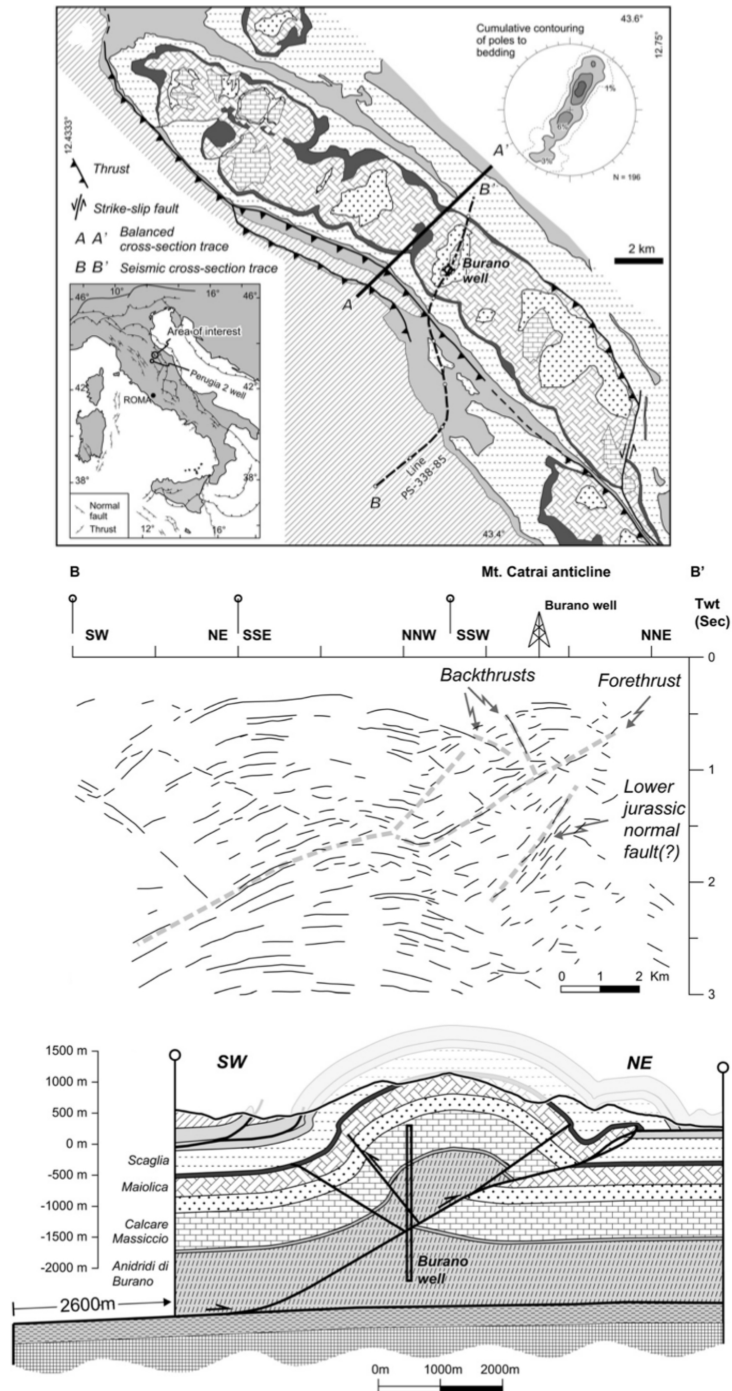


Figure 3.16: Map (upper panel) and interpreted balanced cross-section of the Carbonaceous ridge near the Burano1 (modified from Tavani et al., 2008).

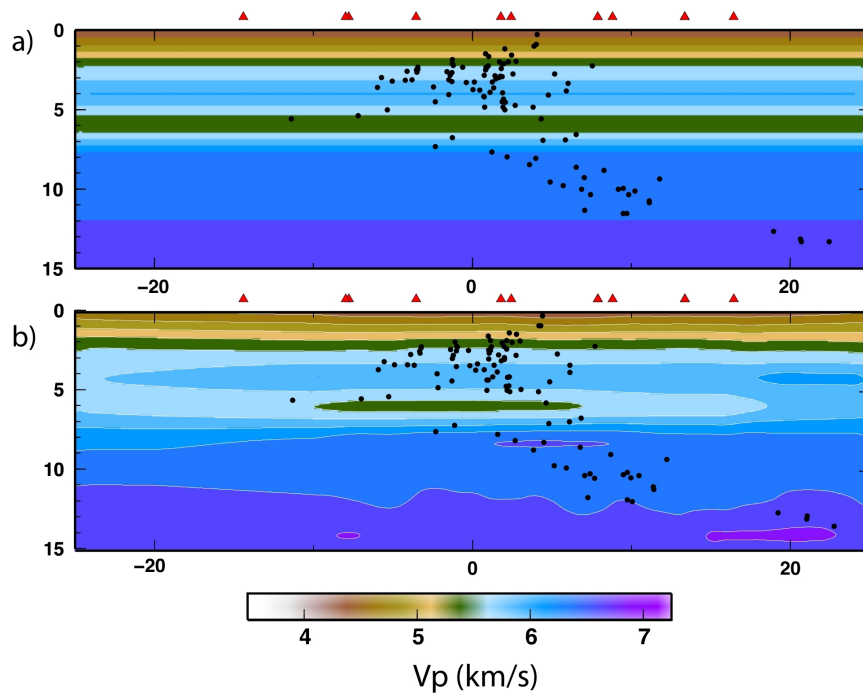


Figure 3.17: Synthetic test showing the capabilities to resolve the velocity reversal at the top of the basement, which is 1.5 km thick. a) Synthetic input  $V_p$  structure, b) recovered  $V_p$  structure. Note that the test has been performed with a subset of data (230 events) and represents a conservative estimate of the regions where a low  $V_p$  zone can be detected.

## 4 Rj-McMc LET at Parkfield

There are many challenging aspects of the application of the RjMcMc LET to the Parkfield area. First, all previously published tomographic models (e.g., Michelini and McEvilly, 1991; Eberhart-Phillips and Michael, 1993; Thurber et al., 2003; 2004; Zhang et al., 2005; Roecker et al. 2004; 2006; Zhang et al., 2009) revealed the existence of large velocity contrasts (up to 20-25%) across the San Andreas Fault. Therefore, a non-linear tomographic code could be demonstrated able to detect such large velocity heterogeneities without the necessity to have accurate starting velocity models. This is important because our new code would be demonstrated suitable for tomographic investigations in poorly known regions, where designing accurate starting models is not possible. Second, the amount of tomographic investigations in the area allows a proper comparison between velocity models obtained from the same data by applying different local earthquake tomography techniques and ray-tracing algorithms. Third, the SAFOD drilling site (San Andreas Fault Observatory at Depth; <http://www.icdp-online.de/sites/sanandreas/index/>) provides velocity data by sonic log measurements to be compared with absolute velocity data obtained from tomography. Fourth, the San Andreas Fault (SAF) near Parkfield has been intensively studied for decades, providing independent constraint to the interpretation of the velocity structure.

### 4.1 Tectonic setting

The San Andreas Fault (SAF) is a right-lateral, strike-slip fault system that extends approximately 1100 km from near the U.S.–Mexican border to northwest of Cape Mendocino, California, and forms the boundary between the Pacific plate to the southwest and the North American plate to the northeast (Figure 4.1). The transform motion began about 29 Ma and has right-laterally displaced rocks at least

300 km (Ross 1984; Irwin 1990). The region is dominated by the NW-SE-trending Southern Coast Ranges, lying between the Pacific coast and the Great Valley, from the San Francisco Bay to the Transverse Range. The range building occurred by folding and thrusting starting at ca. 3.5 Ma, induced by the convergence motion between the two plates, and by subsequent late Quaternary uplift (e.g., Page et al., 1998).

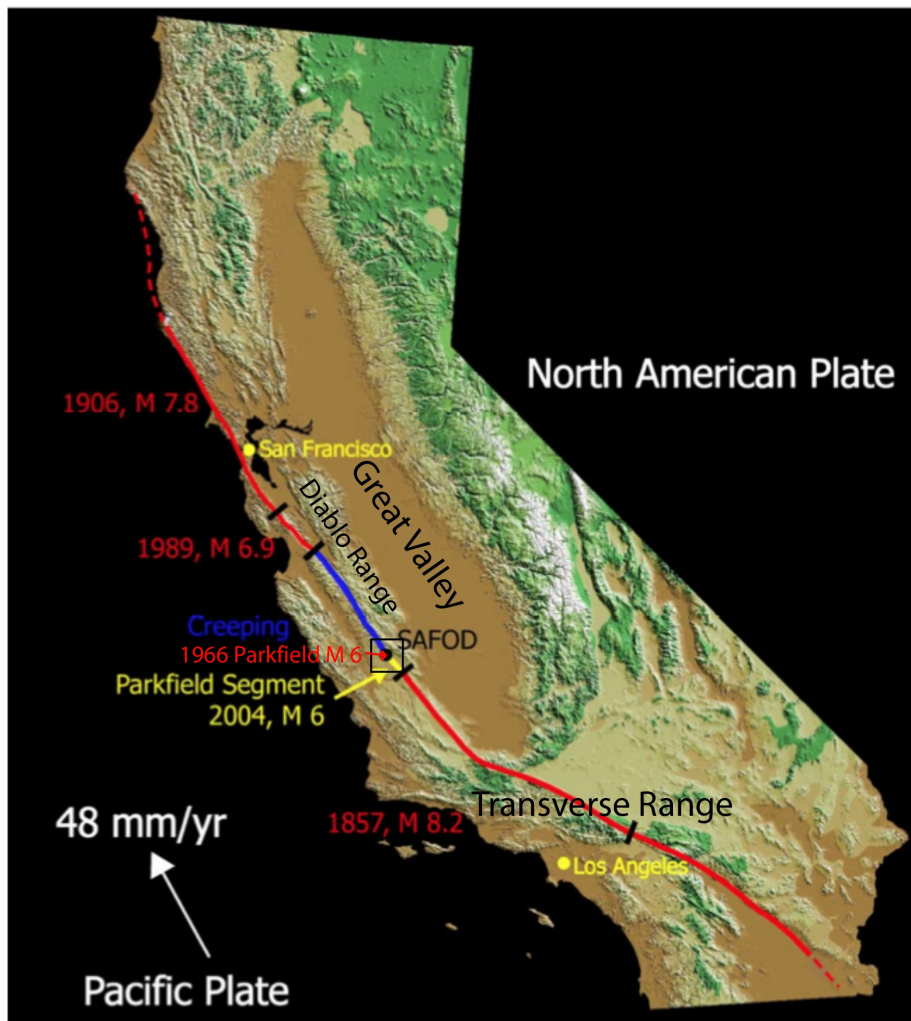


Figure 4.1: Map of California showing the tectonic setting of Parkfield, CA, at the transition between the locked and creeping segments of the San Andreas Fault and the location of SAFOD at the northern end of the Parkfield segment. The inset shows the region investigated in this study.

The Parkfield area is located at the northeastern end of the seismogenic Parkfield segment and adjacent to the creeping segment to the northwest. The historical seismicity is characterized by moderate-magnitude ( $M$  5.5–6) earthquakes occurring, on average, every few decades (e.g., Bakun and McEvilly, 1984; Bakun and Lindh, 1985). However, small to moderate earthquakes ( $M_w < 4$ ) occur more frequently (Nadeau and McEvilly, 1995; Waldhauser et al., 2004).

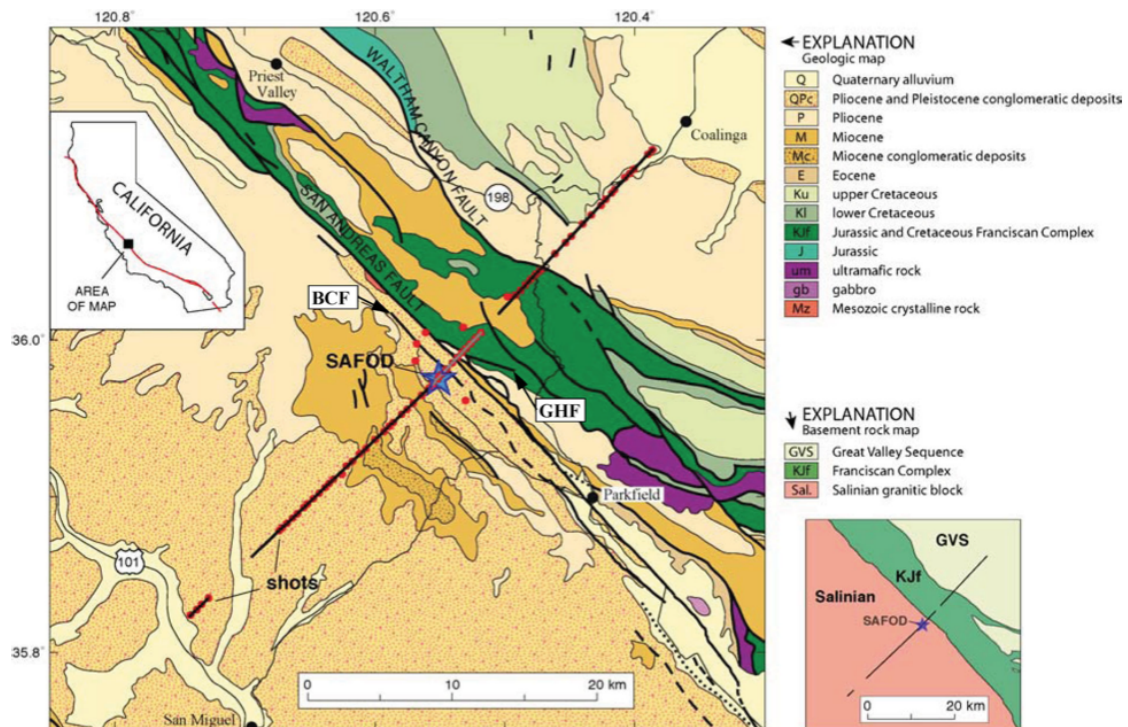


Figure 4.2: Simplified geological map of the Parkfield area (modified from Dibblee Jr. 1980; Bradbury et al. 2007; Ryberg et al., 2012). BCF: Buzzard Canyon fault, GHF: Gold Hill fault.

The long history of strike-slip movement along the SAF created a tectonic contact between continental blocks, which are different in both the tectonic setting where they originated and in their original latitudinal locations (Figure 4.2). Four Mesozoic complexes overlapping in age are present in the Parkfield region: (1) the Salinian block, (2) the Franciscan Complex, (3) the Great Valley sedimentary sequence, and (4) serpentine and ophiolites.

(1) The Salinian block consists of allochthonous late Cretaceous plutonic (mainly granitic and granodioritic rocks) and metamorphic rocks from the axial portion of the western Cordilleran plutonic belt (e.g., Ross, 1978). In the Parkfield area it is locally covered by a maximum of 2 km of Mio-Pleistocene clastic marine and non-marine rocks, dipping westward away from the Cholame Hills high, a Salinian basement uplift that lies some kilometers SW and parallel to the SAF. Metasedimentary rocks (schists) are found at the base of the Salinian pluton in Sierra de Salinas. Seismic reflection imaging (Bleibinhaus et al., 2007) near SAFOD suggests that the base of the Salinian block and the base of the underlying metamorphic rocks are located at about 8.5 and 12 km depth. The location of metasedimentary rocks below the pluton may be a result of tectonic wedging in the latest Cretaceous and Palaeocene (Barth et al., 2003; Grove et al., 2003).

(2) The Franciscan accreted subduction zone melange is widely exposed to the NE of the SAF. The melange, much weaker than the Salinian block, consists of oceanic mantle remnants, oceanic crustal blocks and sedimentary rocks, all included in a strongly sheared argillaceous matrix and in large coherent units of graywacke and metagraywacke. In the Parkfield area, it consists in a southeast-plunging anticlinoria (corresponding to the Parkfield grade, Figure 4.4) cored by serpentine bodies and metasedimentary rocks (Ross, 1978; Page, 1998; Rymer et al., 2003).

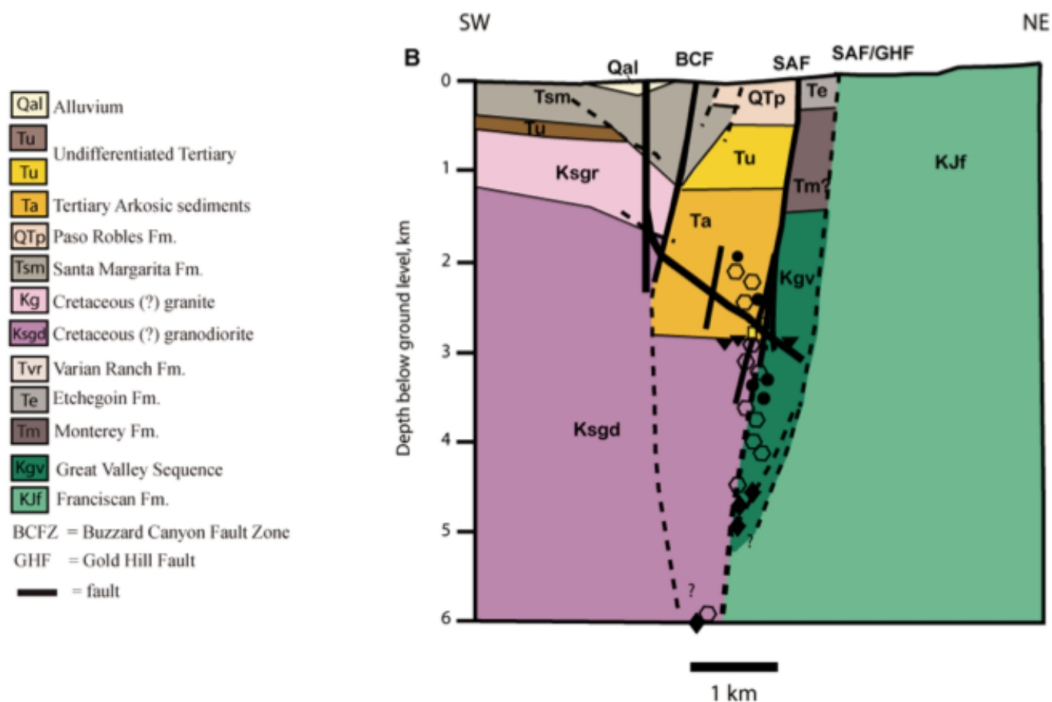
(3) The Jurassic-to-Cretaceous rocks of the Great Valley forearc sediments sequence (SVG, Dickinson, 1966; Page, 1998) are dominated by sandstone and mudstone and include ophiolitic rocks at its base, which correspond to the oceanic floor upon which the Great Valley sequence sediments were deposited. Small volumes of SVG rocks are sampled by the SAFOD main hole (Bradbury et al., 2007) but they are widely exposed to the east of the Parkfield grade, about 10 km from the SAF.

(4) Serpentinite bodies derived from peridotite are distributed into the Franciscan complex and are locally present near secondary faults or compose large diapirs, considered to be extruded by solid flowage from fissures along the crest of a pre-existing ridge (e.g., Table Mountain serpentinite, Dickinson, 1966). Serpentinization and mobilization were probably promoted by the transfer and pressurization of water during subduction and later re-activated by transverse compression (Coleman, 1996). Near SAFOD, the existence of a subsurface flat-lying sheet of serpentinite inside the Franciscan basement has been hypothesized on the base of gravity and

magnetic data (McPhee et al., 2004).

Finally, the shallower stratigraphy consists in Miocene-Pliocene sandstone and mudstone locally overlain by Pleistocene-Quaternary alluvial fan deposit (Dibblee, 1980).

At the surface, the SAF is characterized by a complex zone of faulting that is a few km wide (Dickinson, 1966; Rymer et al., 2006; Thayer, 2006), with 2-3 upwardly flaring flower structures (Catchings et al., 2002; Rymer et al., 2003). The SAFOD drill site lies 1.8 km southwest of the surface trace of the active strand of the San Andreas Fault. The drill site is located on a portion of the SAF characterized by aseismic creep and repeating micro-earthquakes, lying at the northern end of the rupture zone of the 1966 Mw6 Parkfield earthquake. Lithologies and faults encountered by the SAFOD borehole are summarized in Figure 4.3.



## 4.2 Rj-McMc tomography

### 4.2.1 Seismic data and Networks

The arrival times data set was analyzed by several investigations (Roecker et al., 2004; 2006; Thurber et al., 2003; 2004; Zhang et al., 2005). The main data was acquired by the Parkfield Area Seismic Observatory (PASO), a dense seismic array of 59 stations that operated for nearly two years (2000-2002) in a region of about 15 km around the SAFOD drilling site (Figure 4.4).

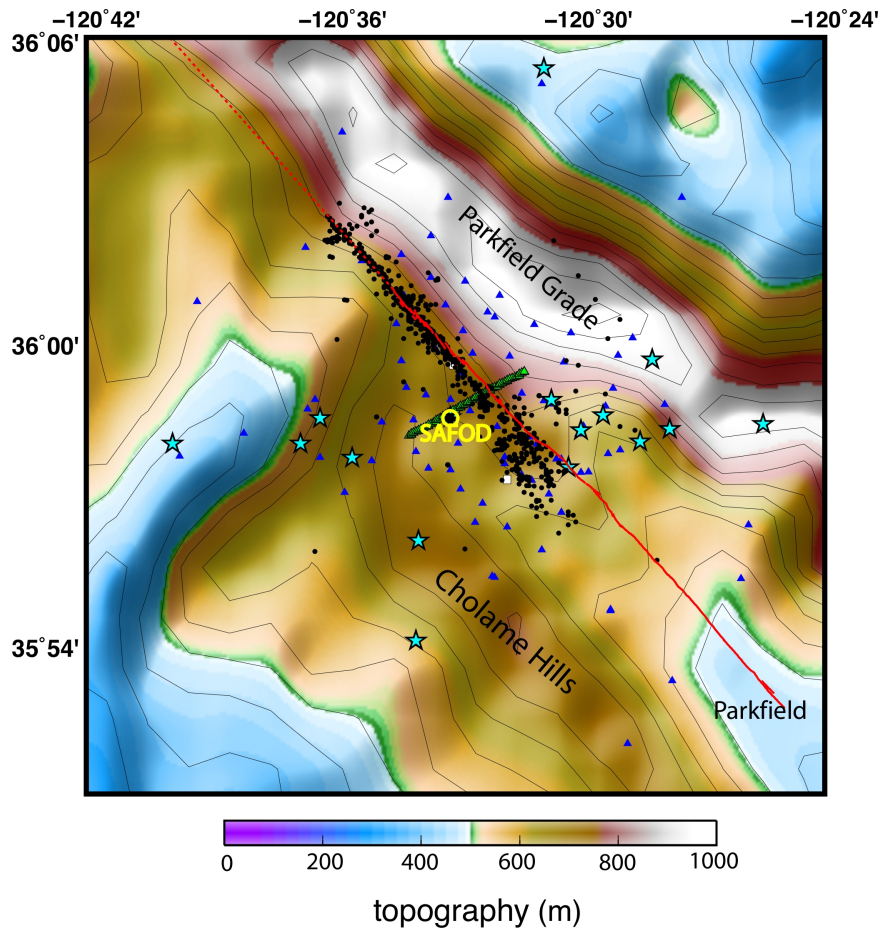


Figure 4.4: Relief map of the study area showing the location of the SAFOD drill site, the PASO array (blue triangles), shots (stars) and the PSINE seismic profile (green triangles). The red line marks the trace of the SAF. Seismicity with starting locations is shown by black points.

Additional data gathered during the same period come from the HRSN (UC-Berkeley's High Resolution Seismic Network), from the USGS CALNET seismic network, from the 32 three-component sensors installed in the SAFOD pilot hole and from 17 shot points set off in the region. More, we used data gathered during the 1998 PSINE survey by Catchings et al. (2002) and explosions from the field projects in 1994 (Li et al., 1997).

In total we used 861 events, 72 blasts and 82 shots. Shots are explosions from the survey by Catchings et al. (2002). The blasts group is composed of 66 shots detonated in October 2002 and acquired by the PASO network and by the borehole sensors and 6 explosions detonated in 1994. The locations are known, but the origin time is permitted to vary to allow for timing errors or near-source delays. The overall arrival time dataset consists of 43948 P-phase arrival times and 29158 S-wave arrival times. For 18689 S-phases, two readings are observed as result of some anisotropy in the crust. When two readings are observed, only the arrival time with the lower picking error is included in the inversion. If the errors are identical, the earlier arrival time is chosen.

We derived data uncertainties from the SAC weighting scheme 0-4. We associated to these weights standard deviation of  $0.025s$  (weight=0),  $0.05s$  (weight=1),  $0.1s$  (weight=2) and  $0.3s$  (weight=3). No different weights are associated to earthquake and shot/blast data. With these data uncertainties, the differences between arrival times of the faster and slower S-phases are less than  $1\sigma$  in the 95% of cases. Furthermore, we are confident that the effect of anisotropy on S-wave arrivals can be considered as included in the picking errors.

### 4.2.2 Prior information

Although some a-priori information can be extracted by the published velocity models and from the SAFOD data, we prefer to start from very rough a priori information. We used Gaussian prior distributions for both velocity and earthquakes parameters. The mean prior model of P-wave velocity is shown in Figure 4.5, together with the background nodes grid. The background nodes grid is characterized by a vertical spacing of 0.5 km, down to 5 km depth and 1-2 km at greater depth. The size of the model is about 25 km in the horizontal plane and 16 km in the

#### 4 Rj-McMc LET at Parkfield

vertical direction. The uneven grid spacing is due to the necessity of reducing the computing time since the great amount of data to deal with.

Two prior Gaussian distributions (one for the  $V_p$  parameter and one for the  $V_p/V_s$  parameter) are associated to each one of the grid nodes. The prior mean  $V_p/V_s$  model is constant throughout the investigate volume, with mean 1.65 and standard deviation equal to 0.15. Standard deviations for the  $V_p$  parameters are all equal to 0.5 km/s.

The mean prior values of the earthquake parameters are identical to those used by Thurber et al. (2004) as starting model for the linearized tomography. Standard deviations are set equal to 1 km in latitude and longitude and 2 km in depth. The origin time parameters are uniformly sampled in between  $\pm 1s$  from the mean prior values.

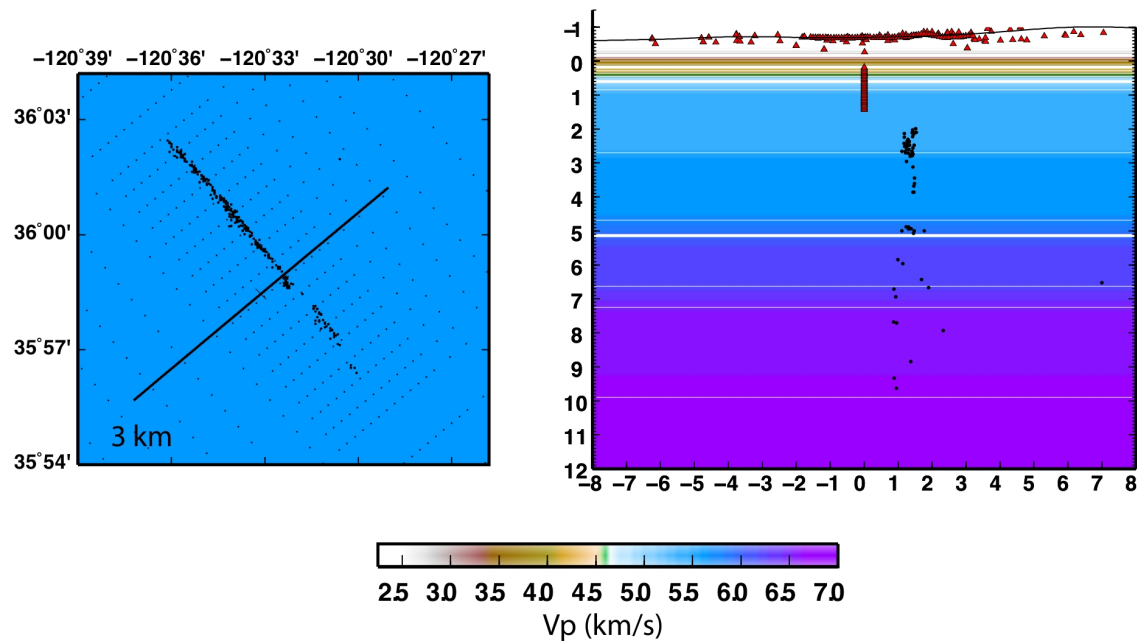


Figure 4.5: Prior mean  $V_p$  model plotted on a horizontal section at 3 km depth (left panel) and on a vertical cross-section (right panel). Red triangles: seismic stations; black circles: mean prior event locations. Note the string of borehole receivers deployed in the SAFOD pilot hole in July 2002.

### 4.2.3 RjMcMc sampling of the PDF and data misfit

We run 20 Markov chains of about 600000 models/chain. After a burn-in phase of 350000 models/chain, when the sampling algorithm has been judged to have converged, we collected every 20th models of the 250000 models/chain generated during the post burn-in phase (Figure 4.6). Then, the total number of PDF samples consists of 250000 models. The recipe of sampling and the convergence assessment criteria are the same described in Chapter 2.

The misfit level reached by the chains during the post burn-in phase is in the range 80000-90000. The number of estimated event parameters amount to 3516 (4 parameters of 861 earthquakes and 72 blasts origin times). The number of velocity parameters is in the range 1750-3250 (5 parameters for each one of the Voronoi's cells), depending on both the chain and the individual model (Figure 4.7). Since the total number of estimated parameters is in the range 5500-6500 and the number of data is 73106, this misfit level corresponds to a normalized  $\chi^2$  misfit measure in the range 1.2-1.3.

Since the huge amount of estimated parameters, the inspection of the PDF distribution for every parameter is not possible. Therefore, we analyze and discuss only the mean and standard deviation values of the 1D marginal PDF and compare them to the prior mean and standard deviation values. New information regarding the model parameter is added by the data to the prior information if the posterior standard deviation is less than the prior standard deviation. As previously described, the individual models are characterized by different Voronoi's tessellations and are all rasterized on the same regular grid (Figure 4.5). Then, mean and standard deviation values of the 1D marginal PDF over the velocity parameters ( $V_p$  and  $V_p/V_s$ ) are computed for each one of the grid nodes. Full maps showing the distribution of the standard deviations across the  $V_p$  and  $V_p/V_s$  models are provided as supplementary Figures 4.19 and 4.20. As regard the event parameters, the posterior standard deviations are less than the prior standard deviations for every event and all the 4 hypocentral parameters. Posterior standard deviations are in the range 100-200 m for event latitude and longitude and a factor of two greater for event depth. About 80 earthquakes have posterior standard deviation greater than 500 m and are not shown in the Figures.

#### 4 Rj-McMc LET at Parkfield

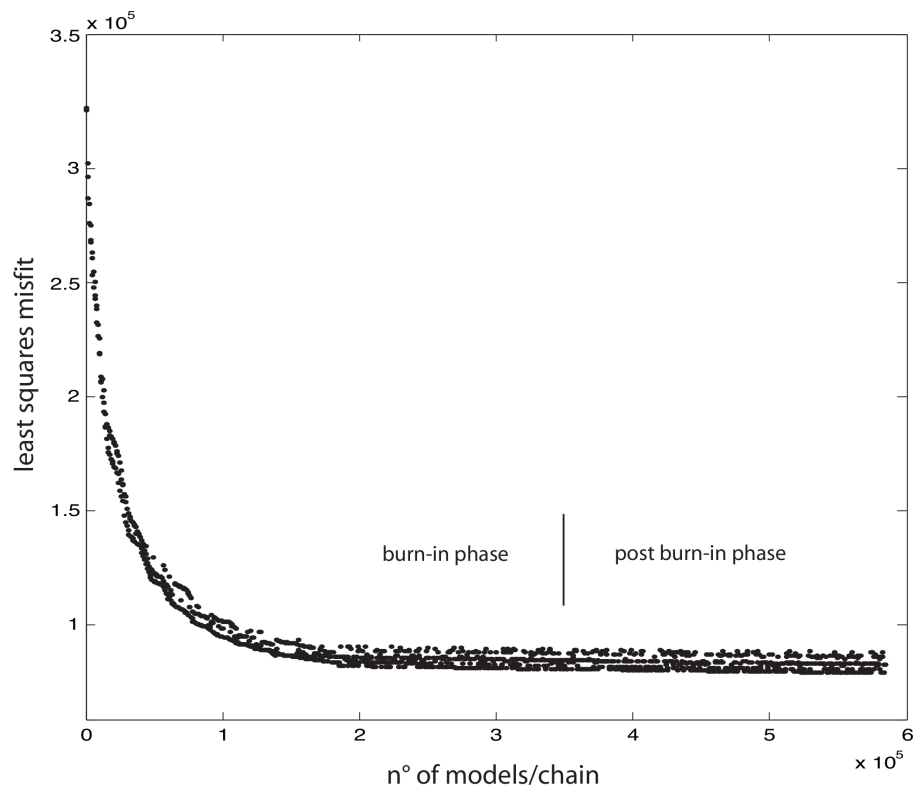


Figure 4.6: Misfit evolution during the Rj-McMc sampling.

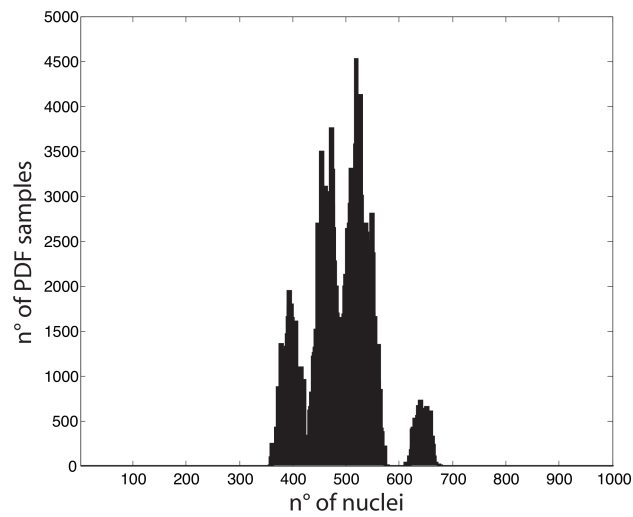


Figure 4.7: 1D marginal PDF over the number of Voronoi's cells.

#### 4.2.4 Discussion on the Vp and Vp/Vs mean posterior models

**Shallow layers (0-2 km, Figure 4.8)** The Vp structure is dominated by the velocity contrast across the SAF, with the southwest side on average about 1.0 km/s faster than the northeast side. At 1 km depth, the seismicity is localized on the northern part of the SAF trace, well-matching the steeper Vp gradient. The most seismicity appears below 2 km depth and is evenly distributed along the trace of the SAF, delineating a very narrow active fault region. Seismicity at this depth occurs inside a high Vp/Vs region.

At the surface (see layer at 0 km depth), a NW-SE elongated low Vp (<3 km/s) and high Vp/Vs belt is present to the east of SAFOD hole (PH) and around the SAF trace (red line), well-matching the LWZ found by shallow high resolution seismic surveys (Catchings et al., 2002). The low Vp belt corresponds to shallow sediments on the SE of the fault and to weathered, highly fractured Franciscan rocks mapped on the NE of the fault.

To the east of the SAF, the Vp is everywhere lower than 4.5-5 km/s, with velocity in average higher to the NW of the SAFOD borehole. In this depth range, velocity in the range 3-4 km/s has been reported for weathered crystalline rocks and well-cemented sedimentary rocks in southern California and velocity in excess of 4 km/s are found for Franciscan crystalline rocks (Gandhok et al., 1999; Catchings et al., 2002). The stronger high Vp/Vs region is characterized by two elongated belts. One high Vp/Vs belt is around and slightly parallel to the SAF, in correspondence of the steepest velocity gradient. The southern portion is located directly below Middle Mountain and appears to be bounded to the east by the Gold Hill fault (GHF) and to the west by the Buzzard Canyon Fault (BCF). The other one follows the shape of the Parkfield grade and corresponds to Franciscan rocks.

To the west of the SAF the velocity is everywhere higher than 4.5-5 km/s and correlated with Vp/Vs values lower than 1.9. Generally higher Vp regions correlate with lower Vp/Vs regions (<1.8), highlighting structural highs of the Salinian granitic basement. Conversely, regions with lower Vp and higher Vp/Vs (>1.9) are spatially correlated with thickened Cenozoic sedimentary rocks to the west of Cholame Hills (Hole et al., 2006).

4 Rj-McMc LET at Parkfield

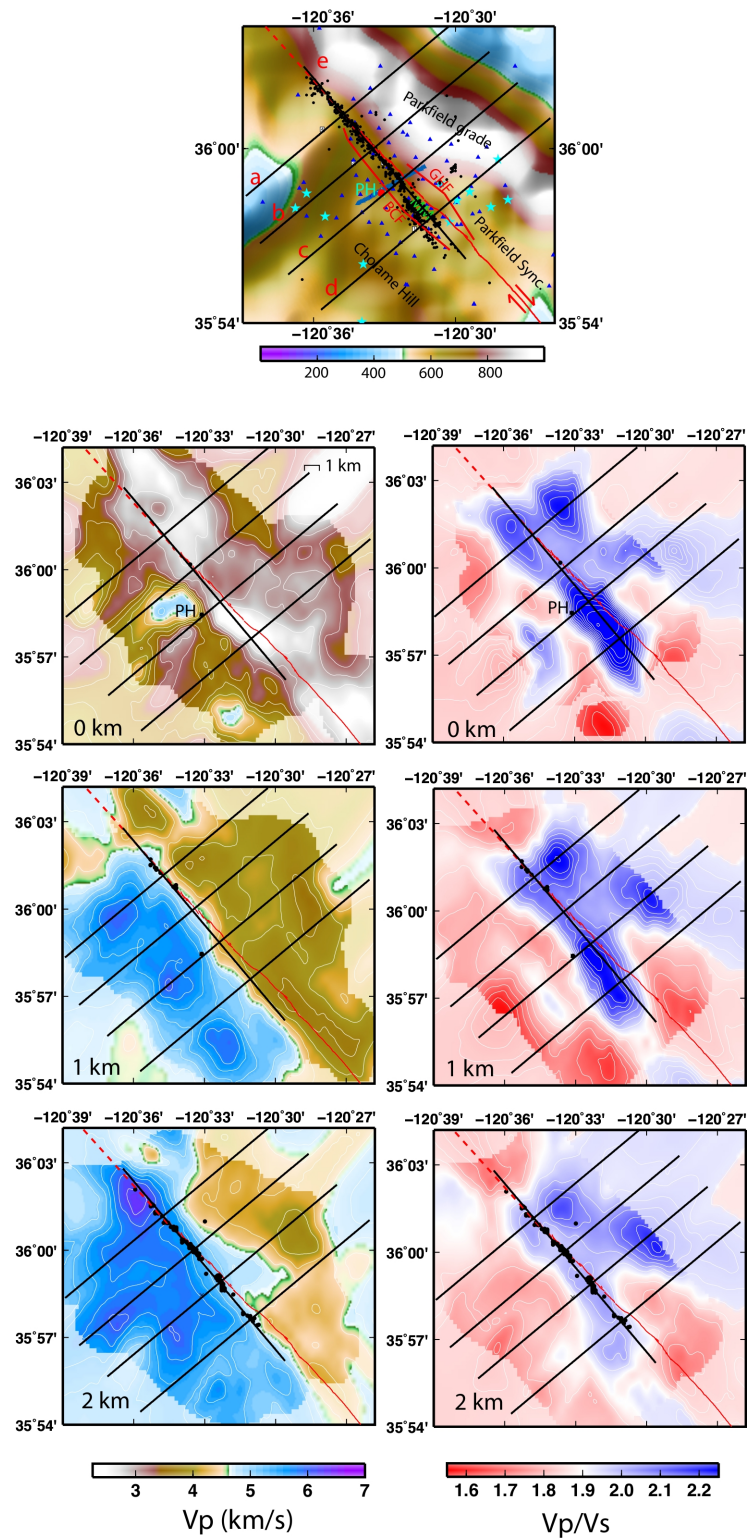


Figure 4.8:  $V_p$  (left panels) and  $V_p/V_s$  (right panels) on horizontal cross-sections at 0, 1 and 2 km depth. Full color marks regions where the posterior standard deviation is less than the prior standard deviation. BCF: Buzzard Canyon Fault, GHF; Gold Hills Fault.

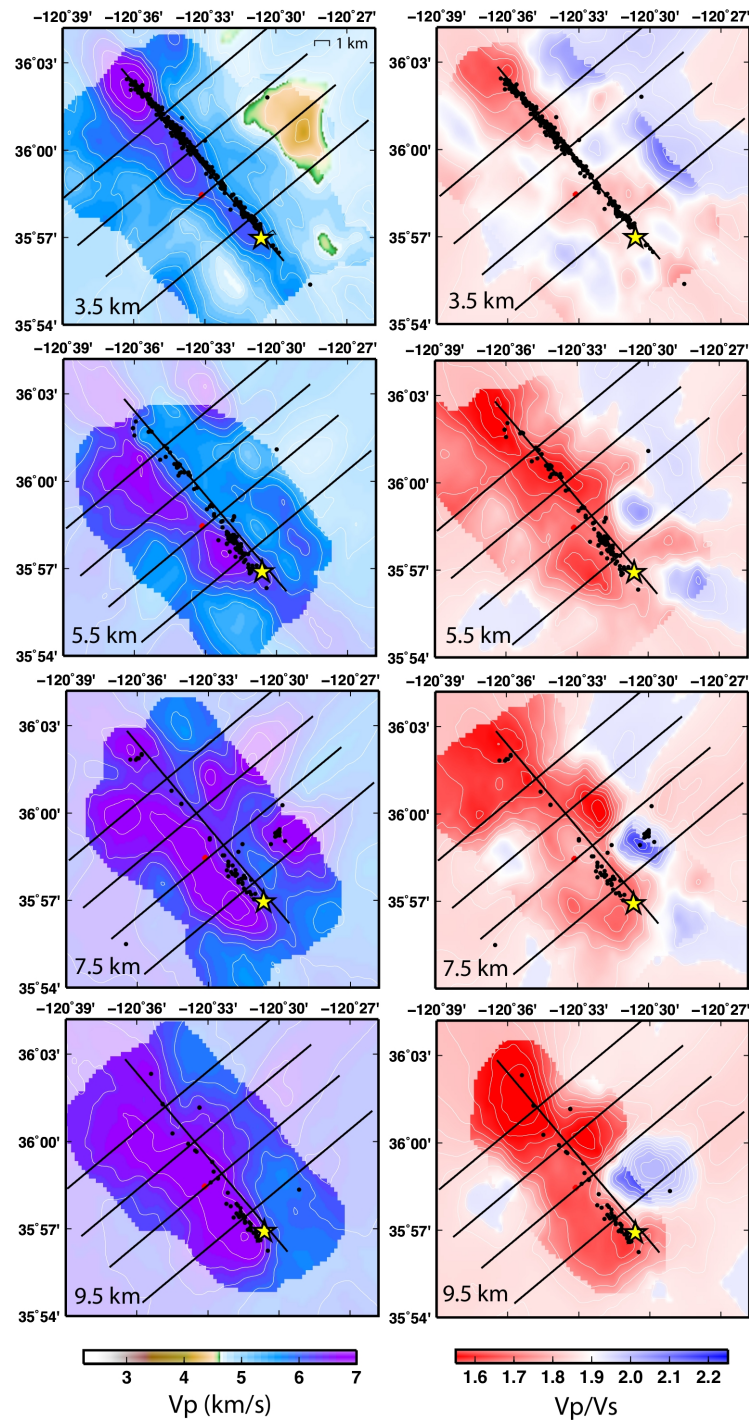


Figure 4.9: Same of Figure 4.8 for horizontal cross-sections between 3.5 and 9.5 km depth. See Figure 4.20 for the standard deviation values. The yellow star is the approximate location of the Mw6 1966 Parkfield earthquake. The red circle indicates the location of the SAFOD borehole.

**Deep layers (3-10 km, Figure 4.9)** The strong velocity contrast across the SAF is visible down to about 10 km depth and the steepest gradient is located along the seismic SAF.

To the southwest of, and parallel to the SAF there is a high Vp belt (6-7 km/s). More to the SW, lower Vp values are found (5-6 km/s). The Vp/Vs is almost everywhere less than 1.75, except for the layer at 3.5 km depth, where some relatively high Vp/Vs (up to 1.90) regions are visible. The standard deviation values in the region are on average 0.2-0.3 km/s, not sufficient to account for a 1 km/s of Vp difference. This suggests strong heterogeneities inside the Salinian composite terrane, because Vp in excess of 6.2 km/s is too high for granites or granodiorites. Both the higher Vp and the low Vp/Vs are consistent with some of the sedimentary rocks metamorphosed to upper amphibolite facies and locally granulite facies intruded by the Mesozoic granitic rocks (Compton, 1966).

To the east of the SAF the Vp sharply decreases to values of about 5.5 km/s. The lowermost Vp regions at depth greater than about 5 km forms a NW-SE-elongated belt localized just to the NE of the seismicity. It is associated with Vp/Vs >1.75, relatively higher than the Vp/Vs found in correspondence of the hypocenters. If the low Vp, higher Vp/Vs belt marks the broad damage zone, a strong asymmetry of the damage zone would be suggested, with the seismicity occurring only at its SW boundary.

Regions of high Vp (>6.5 km/s) are present also to the NE of the SAF, at depth greater than 5-6 km. Similar high Vp anomalies have been identified by Thurber et al. (2006) about 10 km more to the south, and are associated to the Permanente Terrane sequence (Brocher, 2005), an oceanic sequence of mafic rocks. We note that the high Vp regions in our model are not correlated with particular Vp/Vs anomalies, preventing us to infer the nature of these bodies.

Finally, notable differences are visible in both the Vp and Vp/Vs models between the creeping segment to the NW of the SAFOD borehole and the locked segment to the SE. To the NW the Vp contrast across the SAF is higher than to the SE down to 3.5 km depth, and lower at greater depth. More, the average Vp/Vs to the NW of SAFOD is lower in the entire depth range with respect to the SE. Here, a remarkable low Vp and high Vp/Vs volume is present, just to the north of the 1966 Parkfield hypocenter.

**Across-fault Vp and Vp/Vs cross sections** Vertical sections across the SAF (Figure 4.10) provide additional information on the velocity structure.

(i) The sediment-basement transition to the west of the SAFOD well occurs in correspondence of a steep velocity gradient at about 0-0.5 km depth, consistent with seismic refraction studies (e.g., Hole et al., 2001; 2006) and gravity-magnetic data modeling (McPhee et al., 2004). The high Vp, low Vp/Vs basement (Vp 5.8 km/s, Vp/Vs 1.75 on average) correlates with a relatively higher resistivity zone (Unsworth et al., 2000) and can be spatially associated to the slice of granitic basement encountered by the SAFOD borehole at about 0.1 km depth b.s.l. (e.g., Bradbury et al., 2007). The Vp/Vs is slightly too high for typical granites or granodiorites (1.7, Christensen, 1996), suggesting the presence of fluids.

(ii) A velocity reversal is clearly visible at about 5 km SW of the SAF in all the four cross sections. In between 2 and 5 km depth there is a lower Vp channel (Vp reaches a minimum of 5 km/s), slightly westward-dipping, characterized by higher Vp/Vs relative to the overlaying granites. The velocity reversal can be due to gradual differences in rocks structure and composition of the Salinian pluton, as also testified by the different reflectivity found by Bleibinhaus et al. (2007), who reported strong near-vertical reflectors in between 0.5-2 km depth, perhaps indicative of multiple intrusion cycles, overlying almost transparent rocks. The nature of the transparent low Vp, high Vp/Vs channel is uncertain. The velocity reversal encounters the SAFOD borehole near the BCF. Since the deep structure of the BCF is still unknown, we hypothesize that the velocity reversal can be located in correspondence of the SW-ward prolongation of this fault. Ryberg et al. (2012), on the base of correlation between Vp and Vp/Vs clusters and lithology, suggest a similar interpretation. These Authors found that the velocity structure is consistent with granitic Salinian rocks overlaying serpentinite near the SAFOD main hole. The Vp and Vp/Vs in our model are consistent with serpentinites. Moreover, the presence of a serpentinite body provides an alternative explanation to the magnetic and gravity anomaly analyzed by MCPhee et al. (2004), associated by the same Authors to the presence of an unusually magnetic granitic body. Finally, More and Rymer (2007), by analyzing SAFOD borehole cuttings, found evidence of interactions between silica-saturate hydrothermal fluids and serpentine minerals.

4 Rj-McMc LET at Parkfield

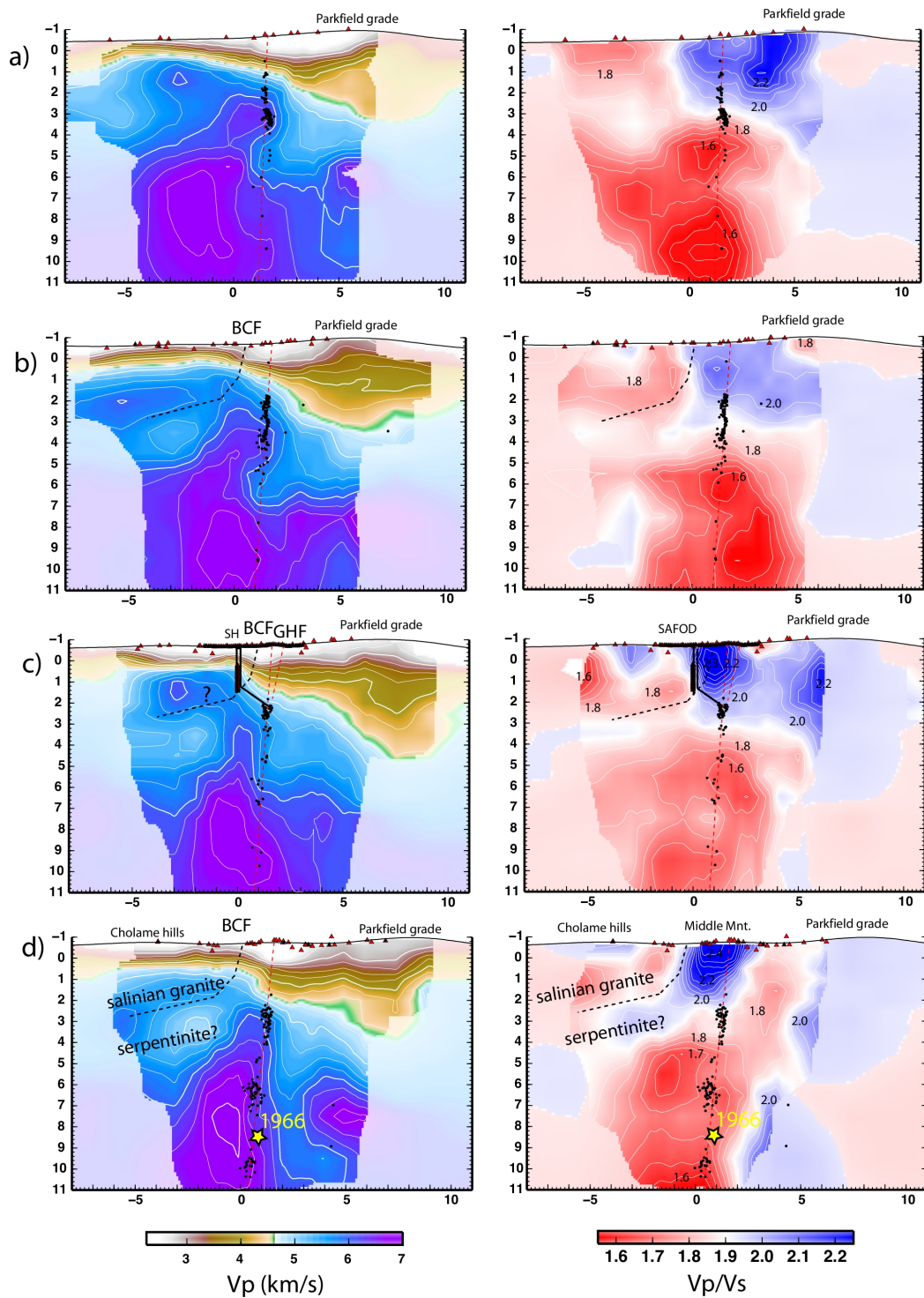


Figure 4.10: Mean  $V_p$  (left panels) and  $V_p/V_s$  models (right panels) plotted on vertical cross-sections. See Figure 4.8 for the locations. Full color regions are areas where the posterior standard deviation is less than the prior standard deviation.

(iii) A steep  $V_p$  and  $V_p/V_s$  discontinuity is visible just to the east of the SAFOD borehole. Here, a low  $V_p$ , very high  $V_p/V_s$  ( $V_p/V_s > 2.2$ ) region extends down to about 2 km between the SAFOD borehole and the GHF (more evident in sections c-d, see also Figure 4.12). Magnetotelluric data show a vertical zone of low-resistivity rocks (FZC: Unsworth et al., 2000; Unsworth and Bedrosian, 2004; Becken et al., 2008) associated with a combination of cracks, interconnected pore fluids and clay minerals existing in the damage zone of the SAF (Ritter et al., 2005). The high fluid content may account for the very high  $V_p/V_s$  value we have found. The most seismicity concentrates below the high  $V_p/V_s$  region, suggesting that microseismicity begins where the rocks have accumulated sufficient stress for brittle failure to occur (see also Nadeau and McEvilly, 1997; Waldhauser and Ellsworth, 1999).

(iv) To the east of the SAF, the low  $V_p$ , high  $V_p/V_s$  region ( $V_p < 5\text{km/s}$ ,  $V_p/V_s > 2$ ), deepens toward the Parkfield grade, reaching depth of about 3-4 km. This anomaly is spatially correlated with a low resistivity region, called eastern conductor (EC), found by MT investigations (Unsworth et al., 2000; Unsworth and Bedrosian, 2004; Becken et al., 2008). The EC has been inferred to be due to the high fluid content of the Franciscan melange. It has also been suggested (e.g. Becken et al., 2008) that fluids of the Franciscan complex enter from NE into the SAF damage zone at shallow depth. With the exception of section d, the high  $V_p/V_s$  region is laterally connected with the very high  $V_p/V_s$  region previously described, in agreement with this idea.

(vi) At depth greater than 3 km low  $V_p/V_s$  values are dominant and show no spatial correlation with the location of the SAF. Low  $V_p/V_s$  can result both in the case of dry rocks and gas-bearing rocks (Dvorkin et al. 1999). In the second hypothesis a low  $V_p$  is expected, because of the higher compressibility of the gas phase. Both the hypotheses are in agreement with the high resistivity found below 3 km depth (Unsworth et al., 2000; Unsworth and Bedrosian, 2004; Becken et al., 2008). Our model is not sufficient to distinguish between the two different hypotheses. Conversely, the low  $V_p/V_s$  is not consistent with the hypothesis of fluid overpressure along the SAF because in this case an increased  $V_p/V_s$  ratio is expected.

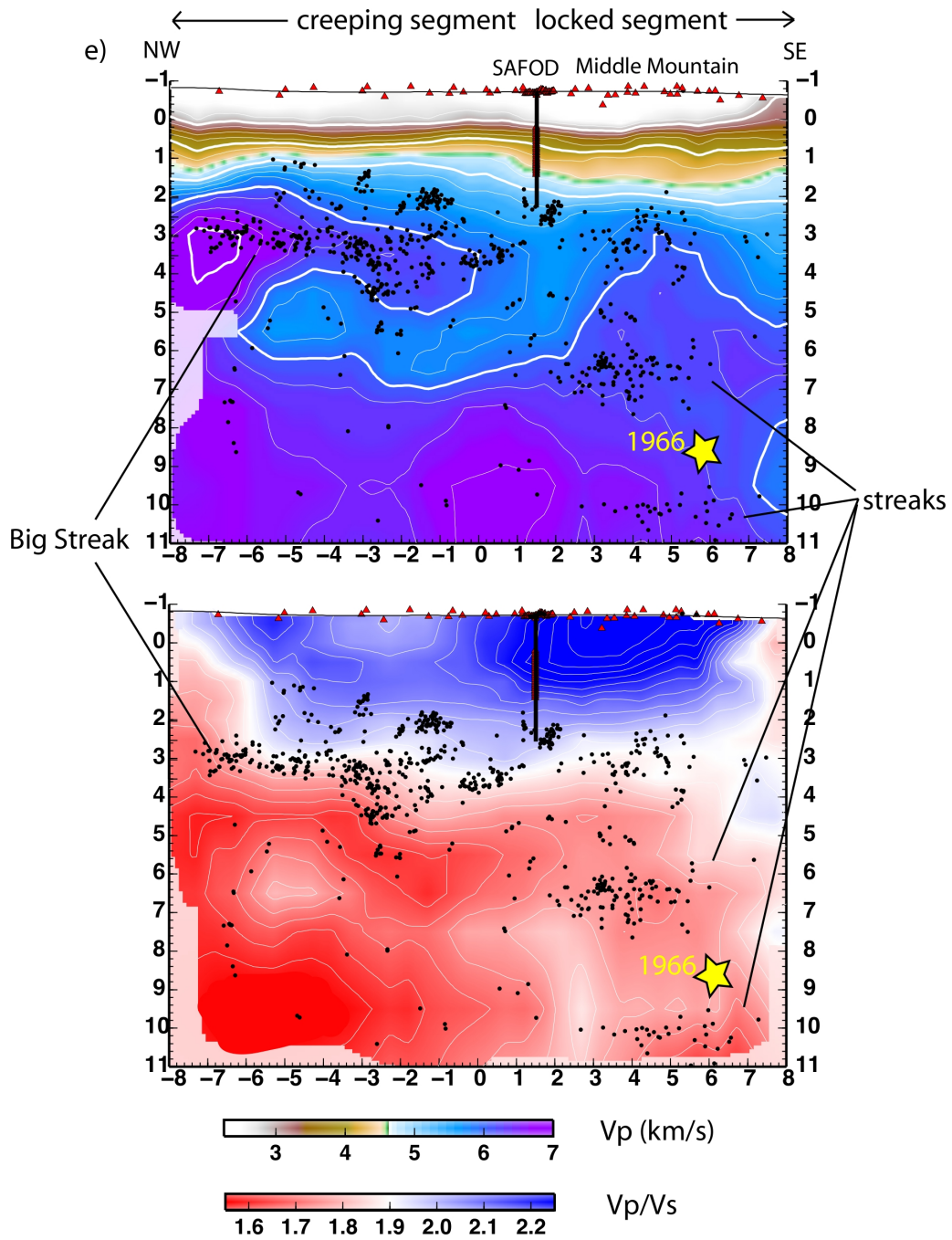


Figure 4.11: Mean posterior  $V_p$  (upper panel) and  $V_p/V_s$  models (bottom panel) plotted on a fault-parallel vertical cross-section e). See Figure 4.8 for the locations.

**Vp, Vp/Vs models and seismicity** The seismicity relocated in our velocity model and shown on a fault-parallel cross-section (Figure 4.11) forms the 'streaks' (horizontal alignments of hypocenters) and the 'holes' (regions devoid of earthquakes) found by Waldhauser et al. (2004) by relocating the whole 1969-2002 dataset. It is noteworthy that the background seismicity is similarly distributed during this time period. More, the moderate-size earthquakes occurred in 1966 and 2004 didn't change the overall distribution of earthquakes in the region (see also Thurber et al., 2006) with aftershocks of both the earthquakes following the distribution of the background seismicity. Thus, the highly organized structures of earthquakes shown in Figure 4.11, although limited to the period 2000-2002, can be considered as representative of the seismicity in the regions.

The 'Big Streak' is particularly evident along the creeping segment northwest of SAFOD. Here, the seismicity forms a slightly SE-dipping alignment of hypocenters at about 3-4 km depth. The 'Big Streak', characterized by frequent repeated events that occur in the same locations and with the same magnitude (e.g., Waldhauser et al., 2004), is located inside and atop a high Vp (6-7 km/s) with a similar SE-dipping geometry. It also corresponds to the transition at increasing depth from high ( $> 1.9$ ) to low ( $< 1.9$ ) Vp/Vs. This suggests that the seismicity occurs at the intersection between the SAF and transition between different rocks strata, as also suggested by Waldhauser et al. (2004) on the base of the active fault patches complexity. If this is true, the low Vp zone below the 'Big Streak', characterized by scarce seismicity, is not related to the damage zone of the SAF, but highlights a different rocks composition and rheology of rocks intersected by the SAF. As previously noted, the regions where the P-wave velocity exceeds 6.2-6.5 km/s are more consistent with amphibolitic or granulitic rocks than with granitic rocks.

To the SE of SAFOD, at the northwest end of the locked segment, the seismicity is deeper and the dip of the fault appears to decrease (see Figure 4.10). In addition to seismicity around 3 km depth, occurring at the transition from high to low Vp/Vs ratio, there are two well-defined streaks at about 7 and 10.5 km depth, interrupted by a region devoid of seismicity ('hole'). Both the streaks are spatially correlated with relatively higher Vp and lower Vp/Vs regions. The microseismicity of the two streaks is not characterized by multiples as the 'Big Streak' and are thought to concentrates at the transition between creeping ('streak') and locked ('hole') fault

patches, representing narrow zones of steep slip rate (Waldhauser et al., 2004). The Mw6 1966 and the 1934 earthquakes (e.g., Bakun and McEvilly, 1979; 1984) initiated beneath Middle Mountain approximately in the 'hole' and propagated toward SE with the main slip zone located outside of our resolved region. Trilateration and GPS data indicate that the 'hole' containing the 1966 event is the area of transition between the NE creeping segment and the SE locked segment of the SAF (Murray et al., 2001). More, the foreshocks of both the 1934 and 1966 events, some moderate size earthquakes ( $4 < M_w < 5$ ) occurred between 1992-1994 and two M5 aftershocks of the Mw6 2004 event nucleated within the "deep streak" and propagated in the 'hole'.

Another notable difference between the creeping and the partially locked SAF segments is found in the Vp/Vs structure. The creeping segment is characterized by relatively lower high Vp/Vs ratio in the shallow region (0-3 km) and strong low Vp/Vs ratio in the deeper region. Conversely, the locked segment has very high Vp/Vs ratio at shallow depth but the deeper low Vp/Vs region is less intense. The lower intensity is located in the correspondence of the seismic 'hole', site of the 1966 earthquake.

The physical relationship between the Vp and Vp/Vs variations and the seismicity is difficult to unravel. The creeping section is characterized by aseismic slip and microearthquakes. Since no great earthquakes occurred in the past in this region, the apparent weakness of this segment cannot be explained through some dynamic weakening process accompanying a major earthquake. The creeping section of the San Andreas fault located to the north of SAFOD is considered to be the best evidence for a weak fault embedded in a strong crust (e.g., Williams et al., 2004; Titus et al., 2006) and this is in agreement with the very low Vp/Vs found in our model. The fault zone weakening is either explained by an unusually low friction coefficient of the fault zone rocks, or by over pressured fluids, which can reduce the apparent shear stress (Hickman et al., 1995). Nevertheless, both the SAFOD data (e.g., Zoback et al., 2011) and the lack of high Vp/Vs anomalies in our velocity model provide no evidence of high pore-pressure along the SAF.

This suggests that the mode of deformation is primary controlled by the different rheology of the rocks intersected by the SAF with fluids perhaps playing a secondary role, especially at greater depth.

### 4.2.5 Comparison with borehole data

The  $V_p$  and  $V_p/V_s$  structures found around the SAFOD borehole are consistent with both geological and borehole data (Figures 4.12 and 4.13). The main  $V_p$  and  $V_p/V_s$  trends along the borehole are both well recovered. Standard deviations are in the ranges 0.15-0.25 km/s and 0.025-0.125 for the  $V_p$  and  $V_p/V_s$ , respectively.

More in detail, both the  $V_p$  and  $V_p/V_s$  in our models are slightly higher than the borehole measurements. Our model fails in detecting the velocity drop at the base of the borehole. Some discrepancy between velocity data and sonic log measurements is expected because of the different frequency of investigation and the occurring of velocity dispersion. Nevertheless, velocity dispersion usually occurs with seismic velocity lower than sonic-log velocity (Batzle et al., 2006 and references therein). Therefore, the more likely explanation for the higher  $V_p$  found around 2 km depth is in the lower spatial resolution of our model (the grid on which we project the Voronoi's tessellation has a inter-nodal spacing of 500 m). A finer grid is currently not practicable because it would require too much computation time. Otherwise we should re-compute the model in a smaller region. Of sure this would be interesting, but actually it goes beyond our purpose. What it is worthy to note is that the first-order correspondence between our velocity models and the sonic data confirms the capability of the newly developed code to resolve fine details of the velocity field, without the need to impose a-priori constraints like those often used in the previous tomographic investigations at Parkfield. Finally, the better correspondence with sonic log data of the  $V_p$  model by Zhang et al. (2009) is likely due to the huge amount of data used if compared with our study.

As regard the  $V_p/V_s$  values, the anisotropy of rocks encountered by the hole (Boness and Zoback, 2006) may be the cause of the general higher  $V_p/V_s$  of our model with respect to sonic log data. Moreover, near the borehole the resolution of the  $V_p$  and  $V_s$  models are quite different because both the shot and blast data provide only the P-wave arrival times.

4 Rj-McMc LET at Parkfield

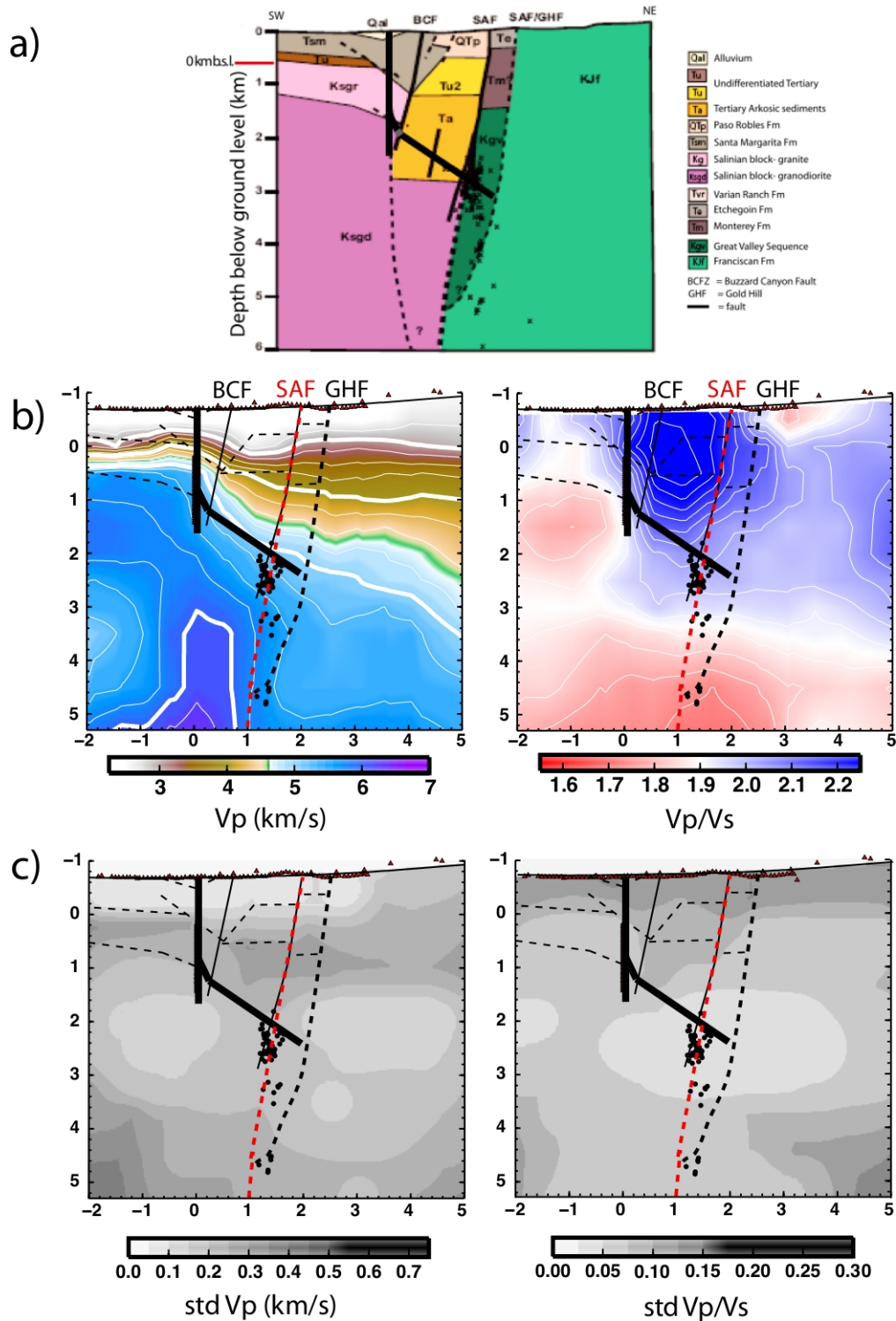


Figure 4.12: Comparison between  $V_p$ ,  $V_p/V_s$  models and geology around SAFOD; a) geological section by Bradbury et al. (2007); b) velocity structure; c) error maps.

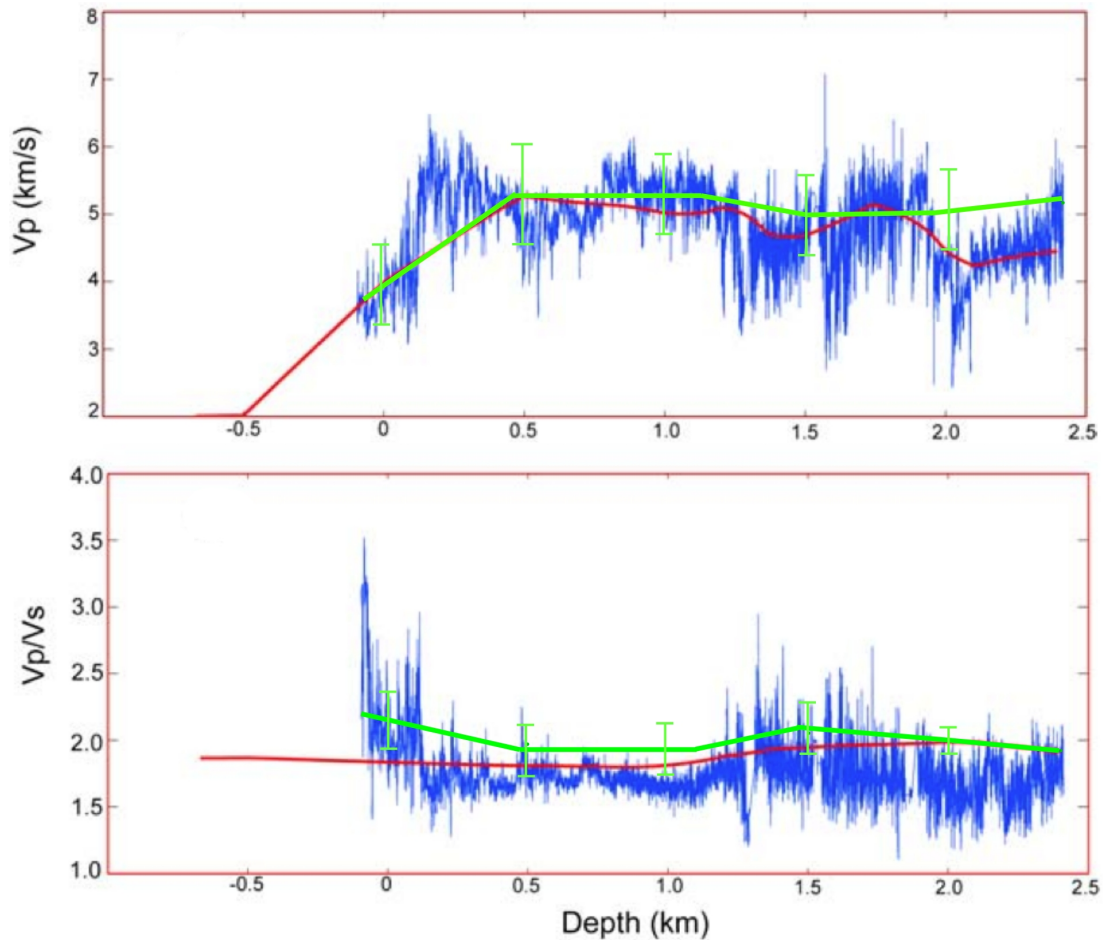


Figure 4.13: Borehole velocity logs in the main SAFOD hole (blue, modified from Zhang et al., 2009);  $V_p$  and  $V_p/V_s$  values derived from our model (green curves) with vertical error bars equal to  $\pm 3\sigma$ ; red curves and from models by Zhang et al. (2009) (red curves).

### 4.3 Comparison with previous models

**Previous LET models** Arrival-time data from local earthquakes in the Parkfield area have been inverted by employing different inversion techniques, different ray tracing algorithms and different parameterization of the Earth structure. Previous tomographic models were published by Lees and Malin (1990); Michelini and McEvelly (1991); Eberhart-Phillips and Michael (1993); Thurber et al. (2003).

Here we focus on the velocity models obtained with the same dataset used in the Rj-McMc tomography. Thurber et al. (2004) compared the results obtained with three different tomographic codes applied to the same dataset: Simul2000 (Thurber and Eberhart-Phillips, 1999), tomoDD (Zhang and Thurber, 2003) and tomoGRAD (Roecker et al., 2004; 2006). In all the tomographic codes the data inversion is carried out using a standard damped least squares technique and including the hypocenters in the inversion problem. Moreover, these models include a velocity contrast of about 0.6 km/s across the SAF in the starting Vp model and use borehole sonic-log measurements of Vp and Vs as strong or soft constraints on the inversion.

The Simul2000 inversion code (Thurber and Eberhart-Phillips, 1999) uses the approximate pseudo-bending ray tracer by Um and Thurber (1987).

The Double-Difference tomographic code (tomoDD) uses both absolute and differential arrival times and is able to produce more accurate event locations and velocity structure near the source region.

The tomoGRAD code jointly fits arrival time data and gravity residuals using a local velocity-density relationship. Since the gravity data were obtained at much more closely spaced points than the available seismic network, they provide additional constraints to the Vp model in areas with sparse seismic data. Moreover, the theoretical arrival times are computed with a different finite difference ray-tracing algorithm (Vidale, 1988; Hole and Zelt, 1995), which allows greater accuracy in strongly heterogeneous media.

Finally, Zhang et al. (2005) used an adaptive parameterization to improve the resolution of the velocity models. The last published model is that by Zhang et al. (2009), but it has been obtained with much more earthquakes and explosions than our model.

Despite the differences in ray-tracing, parameterization and treatment of earthquake locations, these models show no notable differences in the Vp structure. The main result is a sharp horizontal Vp contrast (up to 1km/s) across the SAF below 2-3 km depth that is the depth at which the seismicity begins. A relative low Vp region down 4-8 km is found to the NE of the SAF and a relative high Vp body is found adjacent to the seismicity to the SW of the SAF, showing an offset about 4 km on the SW side of the SAF. Substantial differences appear only in the joint gravity-velocity model by Roeckers et al. (2004; 2006), which shows a velocity re-

versal to the SW of the SAF in between 3 and 5 km depth. More, both the velocity contrast across the SAF and the low Vp region to the NE of the SAF extend to a significantly greater depth.

Conversely, notable differences are present in the Vp/Vs models, maybe because of the different S-wave data used and/or the different damping parameter used in the inversion. As previously noted, we are confident that the difference in multiple S-waves arrival times due to crustal anisotropy are inside the picking errors we have associated to the readings. Nevertheless, if the picking errors used in the inversion are smaller, the choice about which S-wave arrivals to use in the inversion can have a strong effect on the final Vp/Vs model. This could explain the main differences between the models by Thurber et al. (2004) and Roeckers et al. (2006).

In the Figures 4.14, 4.15 and 4.16 we compare our Vp and Vp/Vs models with those by Thurber et al. (2004). The models are derived by using the same starting earthquakes locations and ray-tracing parameters. In addition to the different inversion method, the main differences are the starting Vp model and the treatment of S-wave data. Thurber et al. (2004) use a 3D starting model with velocity fixed along the SAFOD pilot hole (Figure 4.14a). This prevents the comparison with sonic-log data. Concerning the S-wave data, they use the whole S-wave dataset and invert P-S arrivals instead of S-wave arrivals. Instead, we use the S-wave arrivals with the lower picking errors, an approach similar to Roeckers et al. (2004; 2006). This can only partially explain the strong and notable differences between our Vp/Vs model and the Thurber's one. Conversely, the Vp models are similar, testifying that our new method is able to recover the strong velocity contrast across the SAF without any a-priori information about it and that the 3D starting model used by Thurber et al. (2004) is reliable and close to the true model. The main differences between the two models are: (i) the velocity reversal to the SW of the SAF is more evident in our model, in agreement with gravity data (Roeckers et al., 2004), (ii) the adaptive parameterization allows us to better define the shallow Vp structure, which is very similar in both the shape and Vp values to those found by the high resolution refraction profile by Hole et al. (2006), (iii) the Vp to the NE of the SAF is generally lower in our model and (iv) the deeper high and low Vp anomalies are more evident in our model, likely because of the lack of damping regularization.

**Comparison between data fitting** Data misfit in our model is calculated by considering the mean posterior model for both the earthquake parameters and the velocity parameters. We use the simple least square data misfit ( $\phi = \sum_i ((d_i^{obs} - d_i^{calc})/\sigma_i)^2$ ) for the comparison because it doesn't depend on the data-weighting scheme, which is different between the two inversion methods. It depends only on data uncertainties, which have been defined on the base of the SAC weights: standard deviations of 0.025s (weight=0), 0.05s (weight=1), 0.1s (weight=2) and 0.3s (weight=3).

The histograms of P, S and P-S arrival-time residuals are shown for both the two different models in Figures 4.17 and 4.18. Surprisingly, the data misfit is on average 4 times higher for the model by Thurber et al. (2004) (our model:  $\phi_p = 51932$ ;  $\phi_s = 32468$ ;  $\phi_{s-p} = 34976$ ; Thurber et al. (2004) model;  $\phi_p = 166310$ ;  $\phi_s = 173470$ ;  $\phi_{s-p} = 205390$ ).

A huge difference in data fitting is found for the S-wave data. It is worthy to note that Thurber's model is derived by considering all the S-wave arrivals and by inverted S-P arrivals instead of S-wave arrivals. Nevertheless our model fits also the S-P data better than the simul2000 model. We also recompute the misfit for all the available S-phases and not only for those used in the inversion but the difference in data misfit is still very large. As previously shown, the affect of anisotropy on the S-wave arrival times is likely included in the reading uncertainties.

Finally, we note that our tomographic code and simul2000 use very different weighting schemes. Outliers in the Simul2000 code are down-weighted and the weights given to data with different uncertainties are different from those used in our code. Then, data misfit has been re-computed with only P-wave data characterized by residuals lower than 0.5s and SAC weights equals to 0. The difference in P-wave data misfit is still substantial (our model:  $\phi_P = 31026$ , simul2000 model:  $\phi_P = 97732$ ).

The analysis of the difference in data fit testifies that the fully non-linear approach to the LET tomography, the use of a parameterization directly determined by data and the lack of any damping regularization allow to extract more information from the overall time arrivals data.

### 4.3 Comparison with previous models

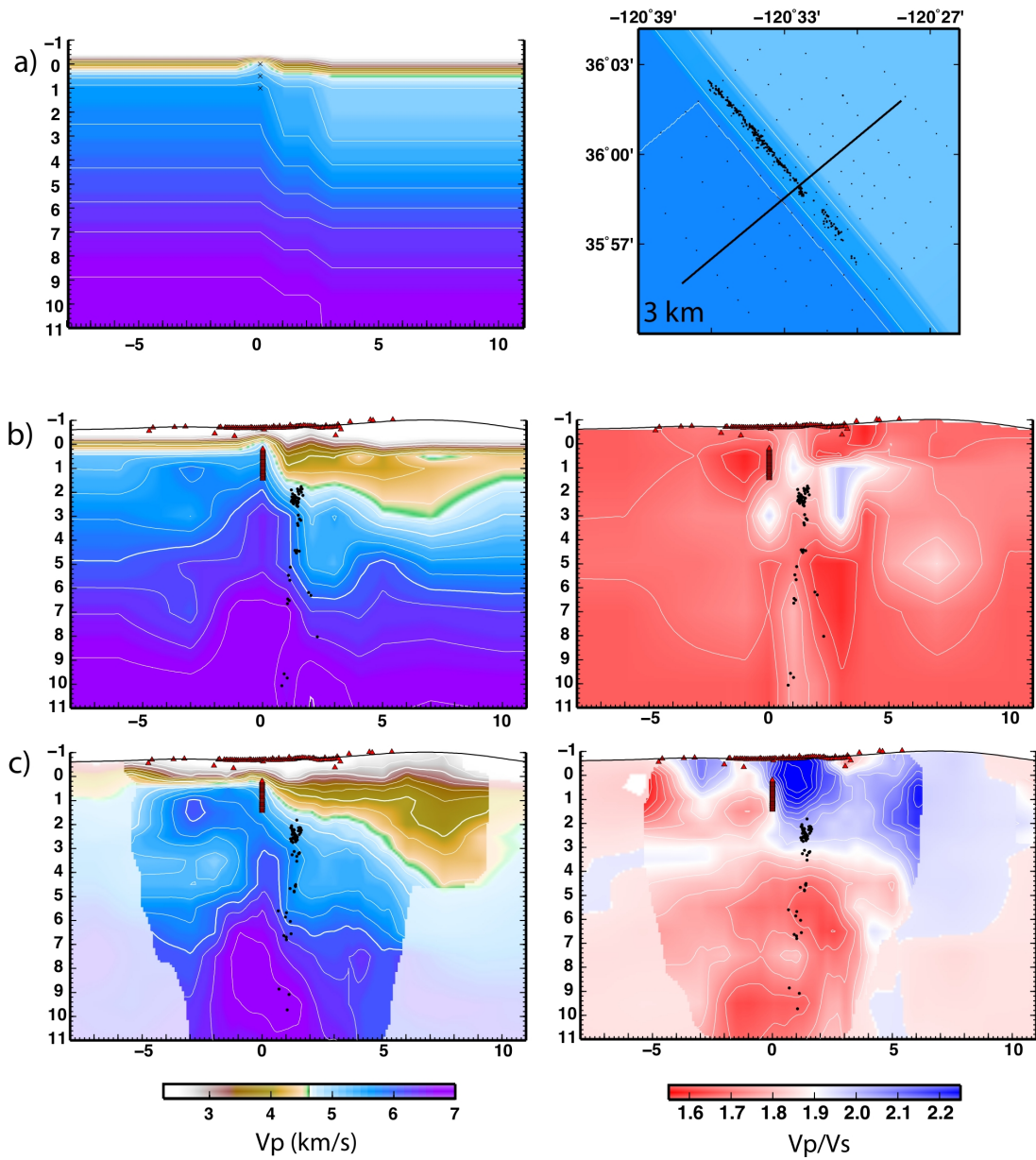


Figure 4.14: a) Starting Vp model by Thurber et al. (2004); b) Vp (left panel) and Vp/Vs (right panel) final models by Thurber et al. (2004); c) our Vp (left panel) and Vp/Vs (right panel).

4 Rj-McMc LET at Parkfield

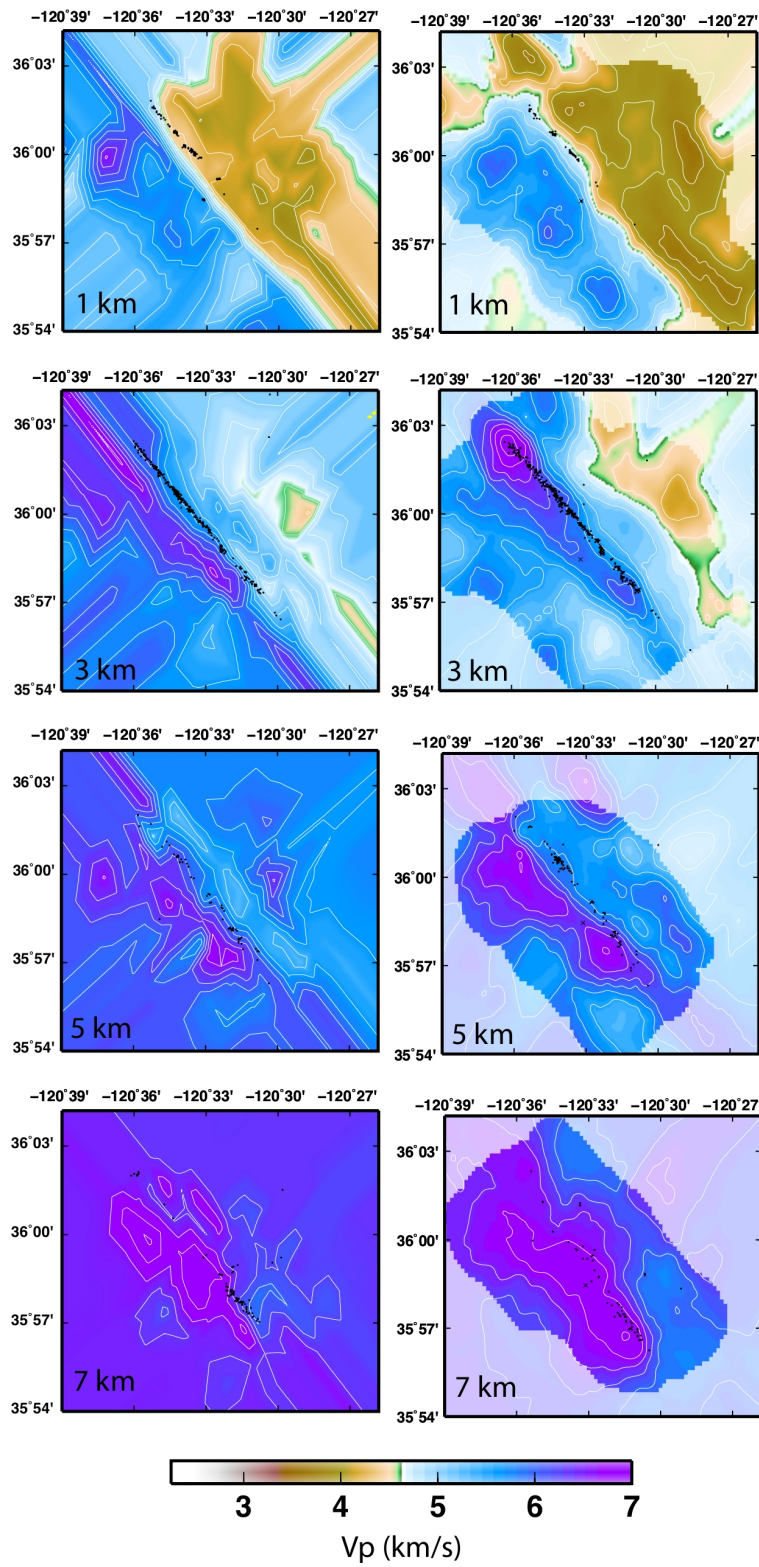


Figure 4.15:  $V_p$  model by Thurber et al. (2004) (left panels) and our model (right panels).

### 4.3 Comparison with previous models

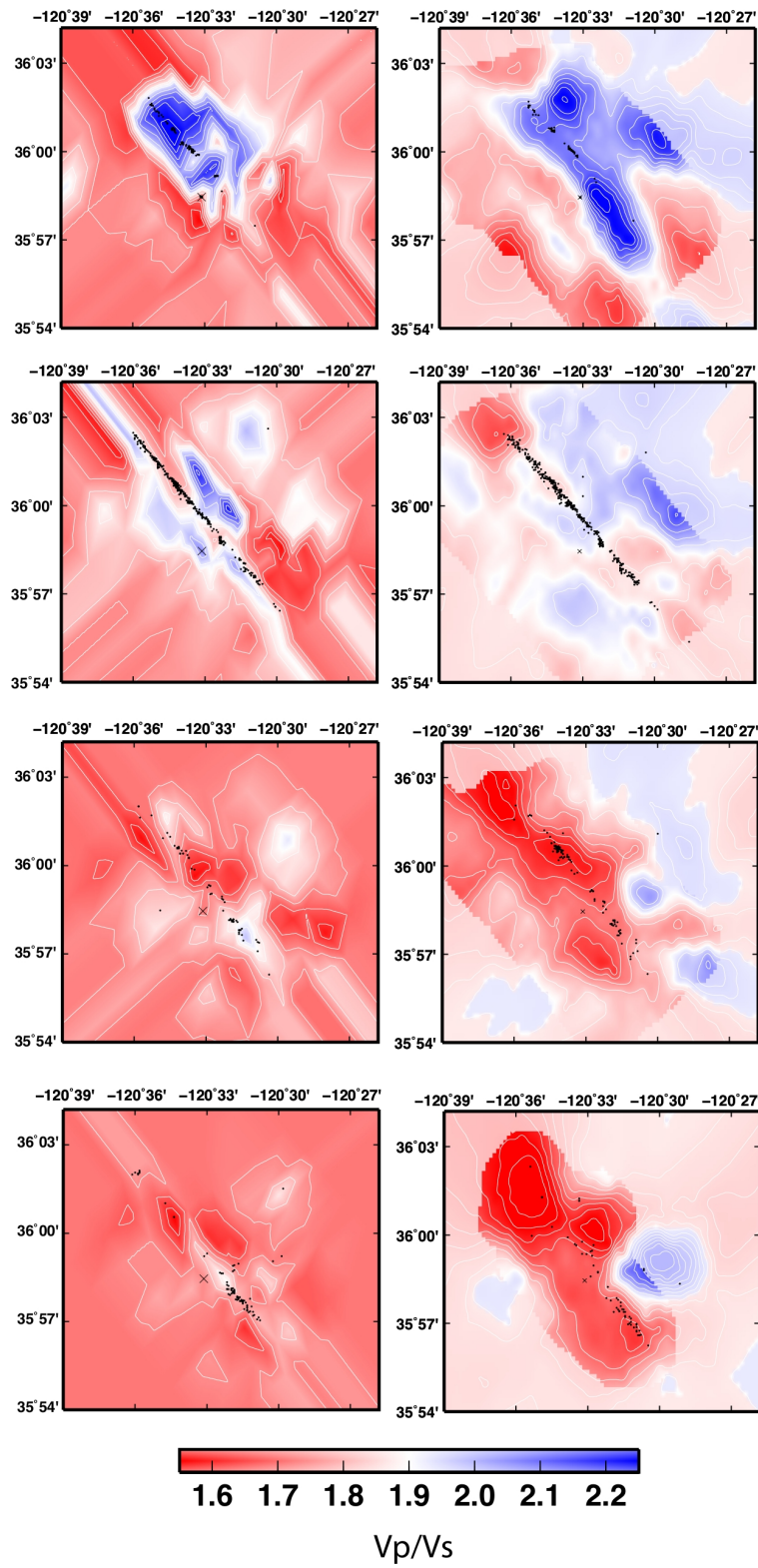


Figure 4.16: Vp/Vs model by Thurber et al. (2004) (left panels) and our model (right panels).

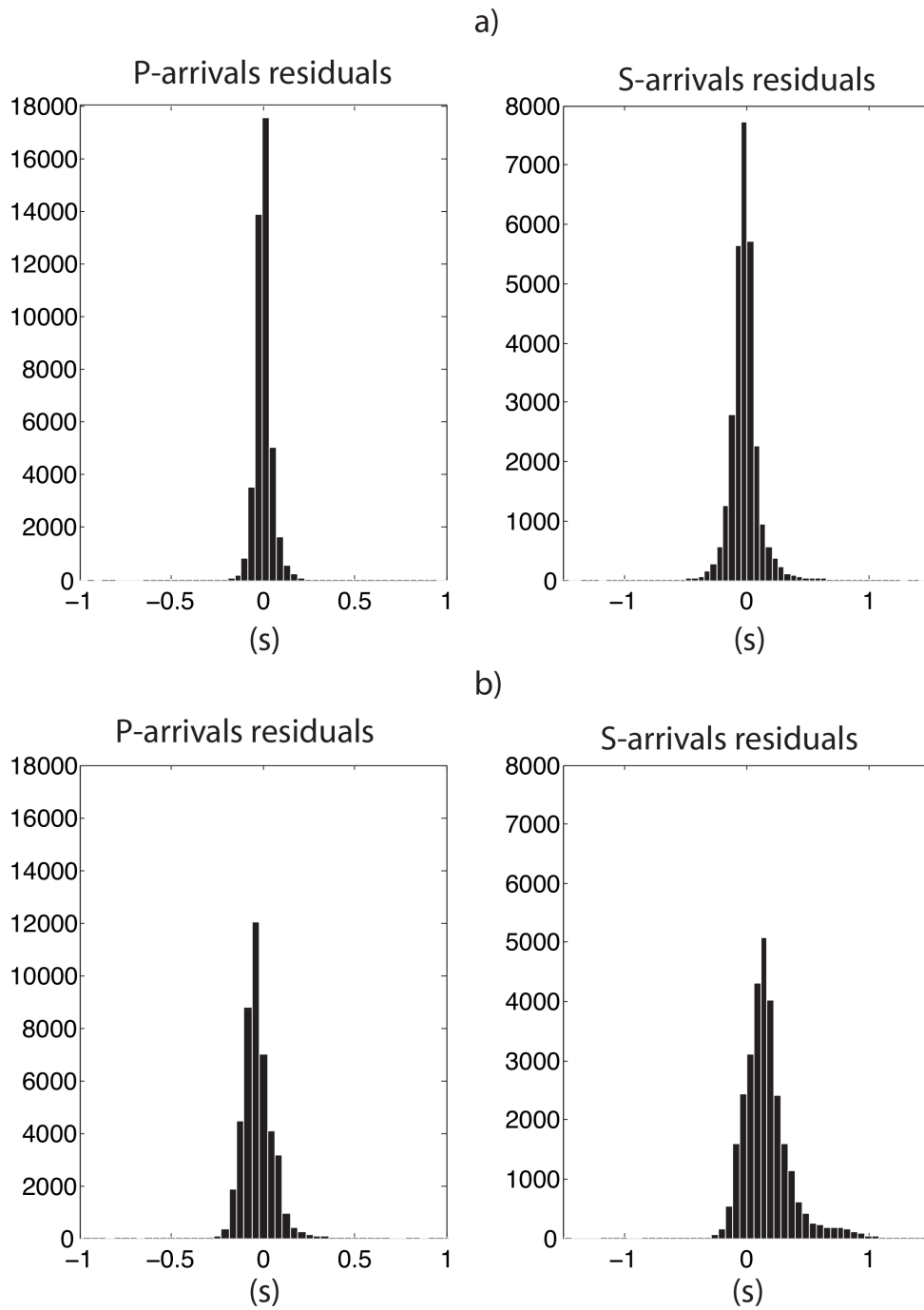


Figure 4.17: P- and S- residuals between observed and theoretical arrival times; a) theoretical arrival times computed in our model; b) theoretical arrival times computed in model by Thurber et al. (2004).

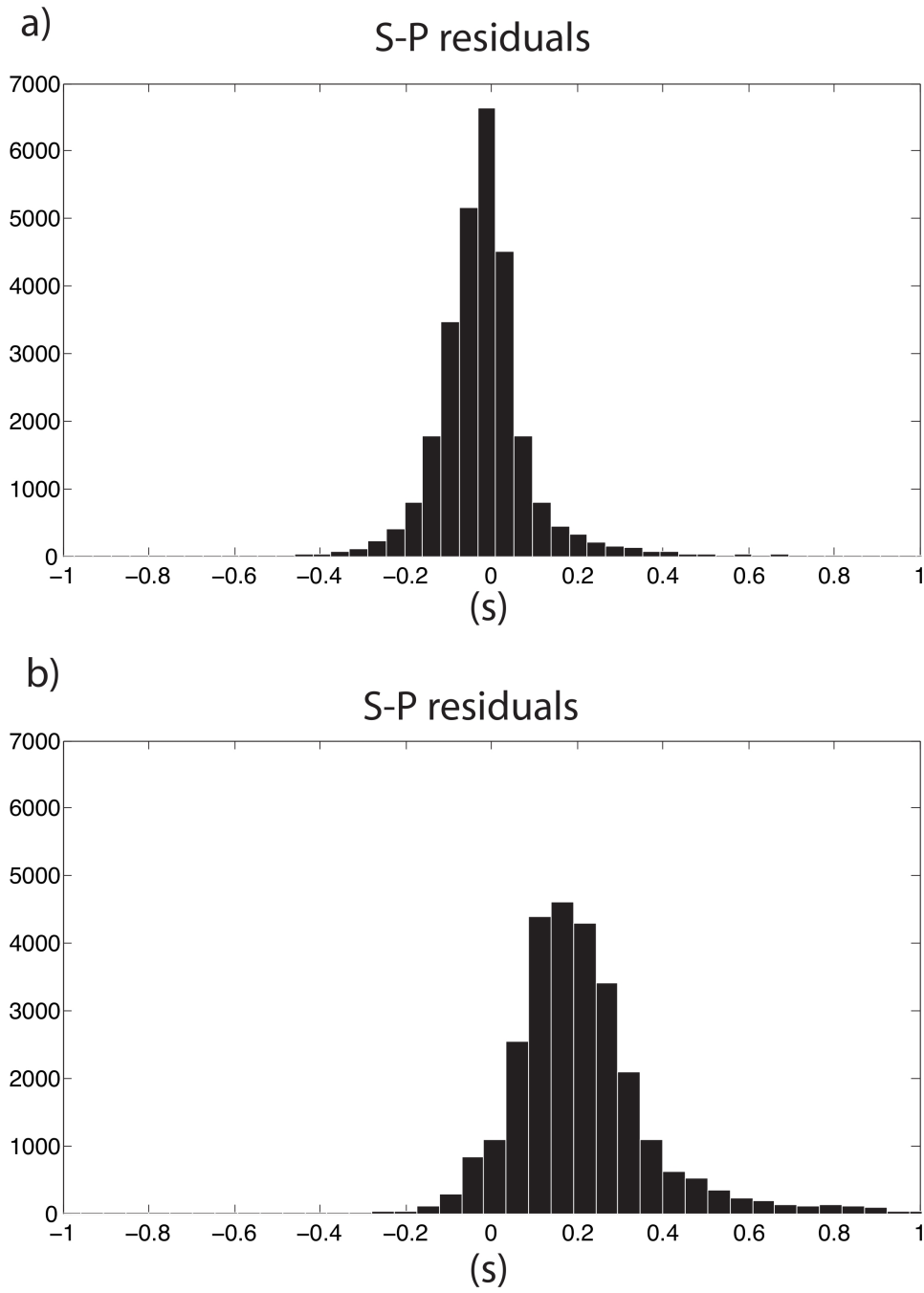


Figure 4.18: S-P residuals between observed and theoretical arrival times; a) theoretical arrival times computed in our model; b) theoretical arrival times computed in model by Thurber et al. (2004)

## Supplementary Figures

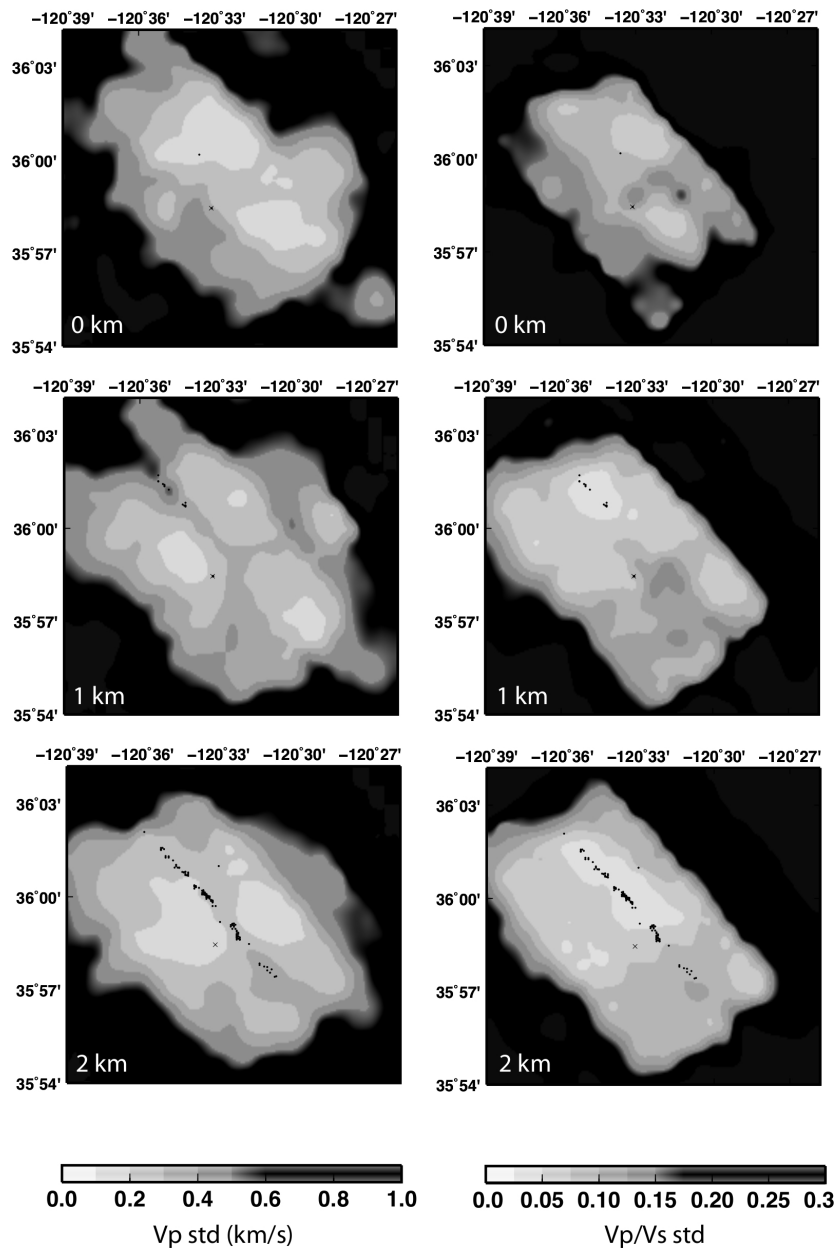


Figure 4.19: Standard deviations of the  $V_p$  (left panels) and  $V_p/V_s$  (right panels) at 0, 1 and 2 km depth.

### 4.3 Comparison with previous models

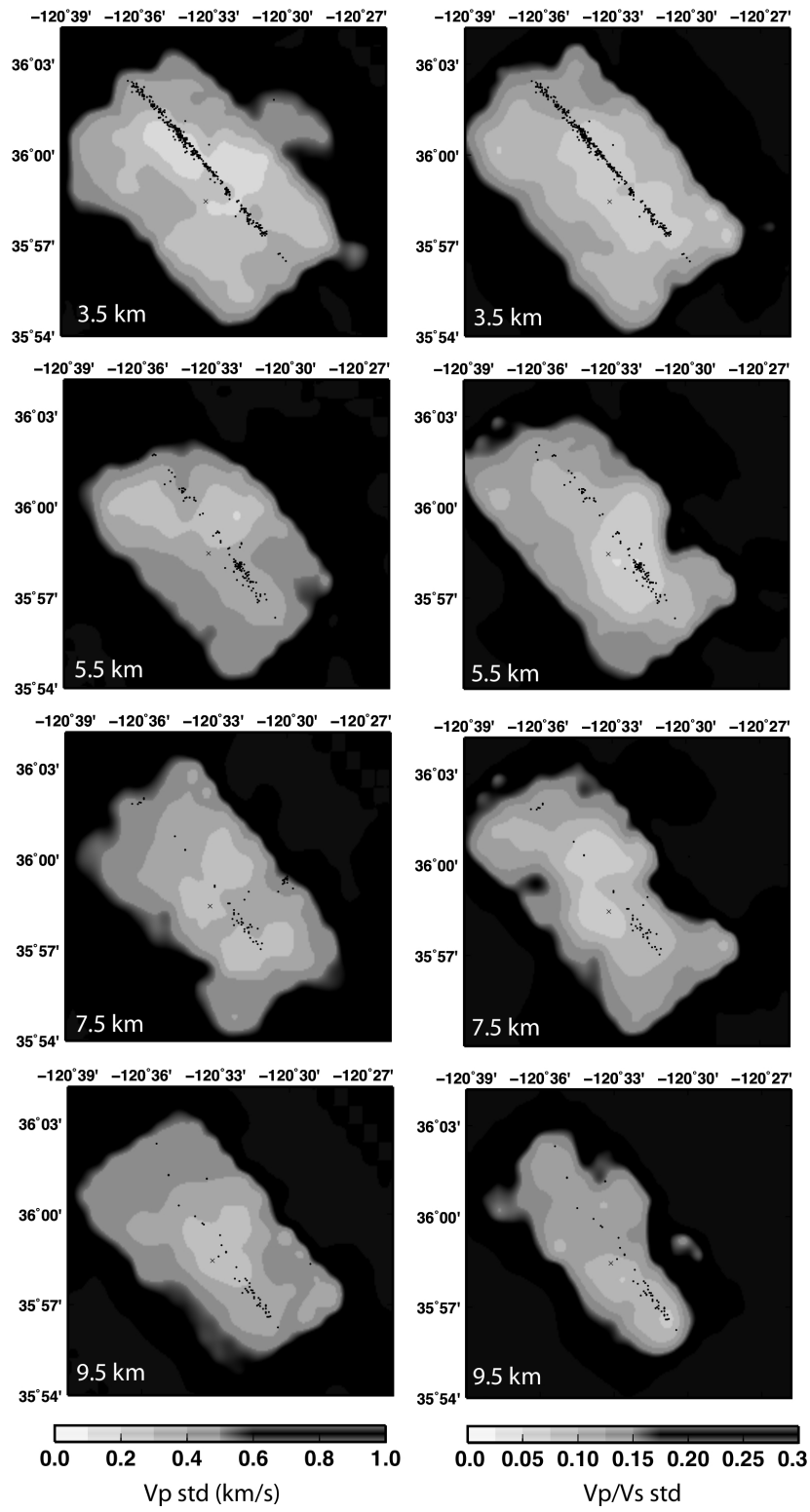


Figure 4.20: Standard deviations of the  $V_p$  (left panels) and  $V_p/V_s$  (right panels) between 3.5 and 9.5 km depth.



# Conclusions

This thesis aimed at presenting a new, fully non-linear, approach to Local Earthquake Tomography.

First, I described the trans-dimensional Monte Carlo sampling applied to seismic tomography. Synthetic tests demonstrated that our algorithm is able to produce a more robust and reliable tomography than standard linearized inversion codes, without the need to make subjective assumptions about starting models and parameterization. Moreover the Bayesian approach provides a more accurate estimate of uncertainties about the model parameters. Synthetic tests also revealed that the lack of any regularization constraints allows extracting more information from the observed data and that the velocity structure can be detected also in regions where the density of rays is low and standard linearized codes fails.

Because of the fully non-linear approach, our code is less dependent on available a-priori information over model parameters. Therefore, it is very suitable for investigating the velocity structure in regions that lack of accurate a-priori information.

Second, I produced high-resolution  $V_p$  and  $V_p/V_s$  models in two widespread investigated regions: the Parkfield segment of the San Andreas Fault (California, USA) and the area around the Alto Tiberina low angle normal fault (Umbria-Marche, Italy). In both the cases, the models obtained with our new code show a substantial improvement in the data fit, if compared with the models obtained from the same data set with the Simulps linearized inversion code. Because of the parameterization directly determined by data, the new code has revealed to be effective in detecting the very shallow velocity structure, where strong velocity heterogeneities and gradients are expected.

## *Conclusions*

Of sure, our code can be further improved:

(i) The ray-tracing algorithm can be substituted by a more accurate and versatile one; actually the ray-tracing is not able to properly compute ray-paths and travel-times of head-waves and this limits the use of data from active seismic investigations.

(ii) A spherical coordinates system can be replaced the Cartesian coordinates system, allowing an extension of the code to regional tomography.

(iii) The speediness of the code can be optimized. For both the Parkfield and the Alto Tiberina test sites, the Rj-McMc tomography required about a week of parallel computing time on a cluster of 250 CPUs. Up to date, the rasterization of the Voronoi's tessellation on the regular grid requires a lot of time. More, the maximum number of grid nodes in the three direction is limited to about 30 by restriction on memory allocation. Since the number of nodes affects the spatial resolution of the resulting velocity model, technical improvements of the code can further enhance the resolution of our models.

(iv) Data noise can be treated as unknown in the Rj-McMc sampling, as shown by Bodin et al. (2012). Absolute picking errors are difficult to estimate because usually the onset of the P- or S-wave is detected only one time. Moreover, picking errors are likely different from Gaussian type. When SAC weights are available, the estimate of absolute errors is arbitrary. It is worthy to note that the size of picking errors is important because it affects the smoothness of the misfit function, the sampling of the parameters space, the convergence achievement and also the posterior errors associated to model parameters.

Finally, our working group is also developing a fully 4D tomography, by allowing the change in time of the medium elastic properties.

# Acknowledgments

I would like to first thank Claudio Chiarabba for his leadership and enthusiastic advice during my Ph.D. study. His support and guidance throughout my graduate studies has helped me to attain a strikingly and amazing picture of the Earth Sciences.

I thank Nicola Piana Agostinetti, the main designer of the new LET code used in this study, for the stimulating discussions and for the opportunity to contribute to the code development. None of this work would be done without him.

I would also like to thank Clifford Thurber, who gently provided the SAFOD dataset and my advisor Andrea Morelli.

Last but not least, I thank Pasquale De Gori for his constant support.



# References

Anderson, E.M., 1951. *The Dynamics of Faulting*, 2nd edition. Oliver and Boyd, Edinburgh, p. 206.

Bakun, W. H., and T. V. McEvilly (1984). Recurrence models and the Parkfield, California, earthquakes, *J. Geophys. Res.* **89**, 3051–3058.

Bakun, W. H., and A. G. Lindh (1985). The Parkfield California earthquake prediction experiment, *Science* **229**, no. 4714, 619–624.

Barchi, M., R. Minelli, and G. Pialli (1998), The crop 03 profile: A synthesis of results on deep structures of the northern Apennines, *Mem. Soc. Geol. Ital.*, **52**, 383–400.

Barchi, M., S. Paolacci, C. Pauselli, G. Pialli, and S. Merlini (1999), Geometria delle deformazioni estensionali recenti nel bacino dell'Alta Val Tiberina fra S. Giustino Umbro e Perugia: Evidenze geofisiche e considerazioni geologiche, *Boll. Soc. Geol. Ital.*, **118**, 617–625.

Barchi, M., C. Pauselli, C. Chiarabba, R. Di Stefano, and C. Federico (2006), Crustal structure, tectonic evolution and seismogenesis in the Northern Apennines (Italy), *Boll. Geofis. Teor. Appl.*, **47** (3), 249–270.

Barchi, M., and M. Ciaccio (2009), Seismic images of an extensional basin, generated at the hangingwall of a low-angle normal fault: The case of the Sansepolcro basin (Central Italy), *Tectonophysics*, **479**, 285–293, doi:10.1016/j.tecto.2009.08.024.

Barth, A.P., Wooden, J.L., Grove, M., Jacobson, C.E. & Pedrick, J.N., 2003. U-Pb zircon geochronology of rocks in the Salinas Valley region of California: a reevaluation of the crustal structure and origin of the Salinian block, *Geology*, **31**, 517–520, doi:10.1130/0091.

## References

- Batzle, M.L., Han, D-H. and Hofmann, R., 2006. Fluid mobility and frequency-dependent seismic velocity - Direct measurements, *Geophysics*, **71** (1), doi: 10.1190/1.2159053.
- Bayes, T., 1763. *An Essay Towards Solving a Problem in the Doctrine of Chances*, ed. C. Davies, Royal Society of London.
- Becken, M., Ritter, O., Park, S. K., Bedrosian, P. A., Weckmann, U., Weber, M., 2008. A deep crustal fluid channel into the San Andreas Fault system near Parkfield, California. - *Geophys. J. Int.*, **173**, 2, 718-732.
- Billings, S.D., Kennett, L.N. and Sambridge, M.S., 1994. Hypocentre location: algorithms incorporating problem-specific information, *Geophys. J. Int.*, **118**, 693-706.
- Bleibinhaus, F., Hole, J.A., Ryberg, T. & Fuis, G.S., 2007. Structure of the California Coast Ranges and San Andreas Fault at SAFOD from seismic waveform inversion and reflection imaging, *J. geophys. Res.*, 112, doi:10.1029/2006JB004611.
- Bodin, T., Sambridge, M. and Gallagher, K., 2009a. A self-parameterising partition model approach to tomographic inverse problems, *Inverse Problems*, **25**, 05509.
- Bodin, T. and Sambridge, M., 2009b. Seismic tomography with the reversible jump algorithm, *Geophys. J. Int.*, **178**, 1411-1436.
- Bodin, T., Sambridge, M., Rawlinson, N. and Arroucan P., 2012. Transdimensional tomography with unknown data noise, *Geophys. J. Int.*, **189**, 1536-1556.
- Boncio, P., F. Brozzetti, and G. Lavecchia (2000), Architecture and seismotectonics of a regional low-angle normal fault zone in central Italy, *Tectonics*, **19**, 1038–1055, doi:10.1029/2000TC900023.
- Boncio, P., and G. Lavecchia (2000), A structural model for active extension in Central Italy, *J. Geodyn.*, **29**, 233–244, doi:10.1016/S0264-3707 (99)00050-2.
- Bonini, M., and C. Tanini (2009), Tectonics and Quaternary evolution of the Northern Apennines watershed area (upper course of Arno and Tiber rivers, Italy), *Geol. J.*, **44** (1), 2–29, doi:10.1002/gj.1122.

- Bradbury, K.K., Barton, D.C., Solum, J.G., Draper, S.D. & Evans, J.P., 2007. Mineralogic and textural analyses of drill cuttings from the San Andreas Fault Observatory at Depth (SAFOD) boreholes: initial interpretations of fault zone composition and constraints on geological models, *Geosphere*, **3**, 299–318.
- Brocher, T. M., 2005. Compressional and shear wave velocity versus depth in the San Francisco Bay Area, California: rules for USGS Bay Area velocity model 05.0.0, *U.S. Geol. Surv. Open-File Rept.* 05-1317, 58 pp.
- Brozzetti, F., P. Boncio, G. Lavecchia, and B. Pace (2009), Present activity and seismogenic potential of a low-angle normal fault system (Città di Castello, Italy): Constraints from surface geology, seismic reflection data and seismicity, *Tectonophysics*, **463**, 31–46, doi:10.1016/j.tecto.2008. 09.023.
- Catchings, R.D., Rymer, M.J., Goldman, M.R., Hole, J.A., Huggins, R. & Lippus, C., 2002. High-resolution seismic velocities and shallow structure of the San Andreas Fault zone at Middle Mountain, Parkfield, California, *Bull. seism. Soc. Am.*, **92**, 2493–2503.
- Cervený, V. and Brown, M., 2003. Seismic ray theory, *J. Acoust. Soc. Am.*, **113**, 14.
- Christensen, N.I., 1996. Poisson's ratio and crustal seismology, *J. Geophys. Res.*, **101** (B3), 3139-3156.
- Chiarabba, C., Amato, A., 2003. Vp and Vp/Vs images in the Mw 6.0 Col\_orito fault region (central Italy): a contribution to the understanding of seismotectonic and seismogenic processes. *Journal of Geophysical Research* **108** (B5), 2248.
- Chiarabba, C., De Gori, P., Boschi, E., 2009. Pore-pressure migration along a normal-fault system resolved by time-repeated seismic tomography. *Geology* **37** (1), 67–70.
- Chiaraluce, L., Ellsworth, W.L., Chiarabba, C., Cocco, M., 2003. Imaging the complexity of an active complex normal fault system: the 1997 Colforito (central Italy) case study. *Journal of Geophysical Research* **108** (B6), 2294. doi:10.1029/2002JB002166.
- Chiaraluce, L., Chiarabba, C., Collettini, C., Piccinini, D. & Cocco, M., 2007. Architecture and mechanics of an active low-angle normal fault: Alto Tiberina

## References

Fault, northern Apennines, Italy, *J. Geophys. Res.*, **112** (B10310), doi:10.1029/2007JB005015.

Chiadini, G., C. Cardellini, A. Amato, E. Boschi, S. Caliro, F. Frondini, and G. Ventura (2004), Carbon dioxide Earth degassing and seismogenesis in central and southern Italy, *Geophys. Res. Lett.*, **31**, L07615, doi:10.1029/2004GL019480.

Cocco, M., Montone, P., Barchi, M.R., Dresen, G., and Zoback, M.D., 2009. MOLE: A multidisciplinary Observatory and Laboratory of Experiments in Central Italy, Scientific Drilling Workshop Report, doi: 10.2204/iodp.sd.7.10.2009.

Coleman, R. G., 1996, New Idria serpentinite: A land management dilemma, *Environmental & Engineering Geoscience* **2**, 9–22.

Collettini, C., and Sibson, R.H., 2001, Normal faults, normal friction?, *Geology*, **29**, 927–930.

Collettini, C., and M. Barchi (2002), A low angle normal fault in the Umbria region (central Italy): A mechanical model for the related micro-seismicity, *Tectonophysics*, **359**, 97–115, doi:10.1016/S0040-1951(02)00441-9.

Collettini, C., and R. E. Holdsworth (2004), Fault zone weakening processes along low-angle normal faults: insights from the Zuccale Fault, Isle of Elba, Italy, *J. Geol. Soc.*, **161**, 1039–1051.

Collettini, C. and M. R. Barchi (2004), A comparison of structural data and seismic images for low-angle normal faults in the northern Apennines (central Italy): Constraints on Activity, in *Flow Processes in Faults and Shear Zones*, edited by G. I. Alsop and R. E. Holdsworth, *Geol. Soc. Spec. Publ.*, **224**, 95–112.

Collettini, C., 2011. The mechanical paradox of low-angle normal faults: Current understanding and open questions, *Tectonophysics* **510**, 253-268.

Compton, R. R., 1966, Analysis of Pliocene–Pleistocene deformation and stresses in northern Santa Lucia Range, California: *Geological Society of America Bulletin*, **77**, 1361–1380.

D’Agostino, N., S. Mantenuto, E. D’Anastasio, A. Avallone, G. Selvaggi, M. Barchi, C. Collettini, F. Radicioni, A. Stoppini, and F. Fastellini (2009), Contemporary crustal extension in the Umbria-Marche Apennines from regional CGPS net-

works and comparison between geodetic and seismic deformation, *Tectonophysics*, **476**, 3–12, doi:10.1016/j. tecto.2008.09.033.

Debski W., 2010. Seismic tomography bt Monte Carlo Sampling. *Pure Appl. Geophys.* **167**, 131-152.

Dibblee T.W., Jr., 1980. *Geology along the San Andreas fault from Gilroy to Parkfield, in Studies of the San Andreas Fault Zone in Northern California*, Special Report 140, pp. 3–18, eds Streitz, R. & Sherburne, R., California Division of Mines and Geology, Sacramento, CA.

Dickinson, W.R., 1966. Structural relationships of San Andreas fault system, Cholame Valley and Castle Mountain Range, California, *Geol. Soc. Am. Bull.*, **77**, 707–726.

Dvorkin, J., Mavko, G. & Nur, A., 1999. Overpressure detection from compressional and shear wave data, *Geophys. Res. Lett.*, **26**, 3417–3420.

Eberhart-Phillips, D., 1986. Three-dimensional velocity structure in northern California Coast ranges from inversion of local earthquake arrival times, *Bull. seism. Soc. Am.*, **76**, 1025–1052.

Eberhart-Phillips, D., 1993. *Local earthquake tomography: earthquake source regions, in Seismic Tomography: Theory and Practice*, pp. 613– 643, eds Iyer, H.M. & Hirahara, K.K., Chapman and Hall, New York.

Eberhart-Phillips, D., and A. J. Michael (1993), Three-dimensional velocity structure, seismicity, and fault structure in the Parkfield region, central CA, *J. Geophys. Res.*, **98**, 15,737–15,758, doi:10.1029/93JB01029.

Eberhart-Phillips, D. & Reyners, M., 1997. Continental subduction and three-dimensional crustal structure: the northern South Island, New Zealand, *J. Geophys. Res.*, **102**, 11 843—11 861.

Eberhart-Phillips, D. & Reyners, M., 1999. Plate interface properties in the northeast Hikurangi subduction zone, New Zealand, from converted seismic waves, *Geophys. Res. Lett.*, **26**, 2565–2568.

Gallagher, K., Charvin, K., Nielsen, S., Sambrige, M. and Stephenson, J., 2009. markov chain Monte Carlo (MCMC) sampling methods to determine optimal mod-

## References

els, model resolution and model choice for Earth science problems, *Marine Petroleum Geol.*, **26**, 525-535.

Gandhok, G., R. D. Catchings, M. R. Goldman, E. Horta, M. J. Rymer, A. Christensen, and P. Martin (1999). High-resolution seismic reflection/ refraction imaging from I-10 to Cherry Valley Blvd., Cherry Valley, Riverside County, California: implications for water resources and earthquake hazards, *U.S. Geol Surv. Open-File Rept.* 99-320, 56 pp.

Green, P., 1995. Reversible jump MCMC computation and Bayesian model selection, *Biometrika*, **82**, 711-732.

Green, P., 2003. Trans-dimensional Markov chain Monte Carlo, *High. Struct. Stoch. Syst.*, **27**, 179-198.

Grove, M., Jacobson, C.E., Barth, A.P. & Vucic, A., 2003. Temporal and spatial trends of Late Cretaceous-early Tertiary underplating of Pelona and related schist beneath southern California and southwestern Arizona, in Tectonic Evolution of Northwestern Mexico and the Southwestern USA, *Geol. Soc. Am. Special Paper* **374**, pp. 381–406, eds Johnson, S.E., Fletcher, S.R.P.J.M., Girty, G.H., Kimbrough, D.L. & Martin-Barajas, A., Geological Society of America, Boulder, CO.

Hastings, W., 1970. Monte Carlo simulation methods using Markov chain and their applications, *Biometrika*, **57**, 97-109.

Heinicke, J., Braun, T., Burgassi, P., Italiano, F. & Martinelli, G., 2006. Gas flow anomalies in seismogenic zones in the Upper Tiber Valley, Central Italy, *Geophys. J. Int.*, **167**(2), 794–806, doi:10.1111/j.1365- 246X.2006.03134.x.

Hole, J.A., Catchings, R.D., St. Clair, K.C., Rymer, M.J., Okaya, D.A., & Carney, B.J., 2001. Steep-dip seismic imaging of the San Andreas fault near Parkfield, *Science*, **294**, 1513–1515.

Hole, J., Ryberg, T., Fuis, G., Bleibinhaus, F. & Sharma, A.K., 2006. Structure of the San Andreas fault zone at SAFOD from a seismic refraction survey, *Geophys. Res. Lett.*, **33**, L07312, doi:10.1029/2005GL025194.

Holdsworth, R. E. (2004), Weak faults-rotten cores, *Science*, **303**, 181 – 182.

Hopcroft, P., Gallagher, K. and Pain, C., 2007. Inference of past climate from borehole temperature data using Bayesian Reversible Jump Markov chain Monte Carlo, *Geophys. J. Int.*, **171**, 1430-1439.

Hreinsdottir, S. and Bennett, A., 2009. Active aseismic creep on the Alto Tiberina low-angle normal fault, Italy, *Geology*, **37**, 683-686.

Irwin, W.P., 1990. Geology and plate-tectonic development, in The San Andreas Fault System, California, *U.S. Geol. Surv. Open Prof. Paper* 1515 pp. 51–80, ed. Wallace, R., U.S. Geological Survey, Washington, DC.

Hopcroft, P.P., Gallagher, K. and Pain C.C., 2007. Inference of past climate form borehole temperature data using Bayesian reversible jump Markov Chain Monte Carlo, *Geophys. J. Int.*, **171**(3), 1430-1439.

Li, Y.-G., W. L. Ellsworth, C. H. Thurber, P. Malin, and K. Aki (1997), Fault zone guided waves from explosions in the San Andreas fault at Parkfield and Cienega Valley, California, *Bull. Seismol. Soc. Am.*, **87**, 210–221.

Li, Y.-G., and P. E. Malin (2008), San Andreas Fault damage at SAFOD viewed with fault-guided waves, *Geophys. Res. Lett.*, **35**, L08304, doi:10.1029/2007GL032924.

Malinverno, A. and Leaney, W., 2000. A Monte Carlo method to quantify uncertainty in the inversion of zero-offset VSP data, in *SEG 70th Annual Meeting*, Calgary, Alberta, The Society of Exploration Geophysicists (Expanded Abstracts).

Malinverno, A., 2002. Parsimonious Bayesian Markov chain Monte Carlo inversion in a nonlinear geophysical problem, *Geophys. J. Int.*, **151**(3), 675-688.

Malinverno, A. and Leaney, W., 2005. Monte-Carlo Bayesian look-ahead inversion of walkaway vertical seismic profiles, *Geophys. Prospect.*, **53**(5), 689-703.

Mariucci, M.T., Montone, P., and Pierdominici, S., 2008. Active stress field in central Italy: a revision of deep well data in the Umbria region. *Ann. Geophys.*, **51**.

McPhee, D.K., Jachens, R.C. & Wentworth, C.M., 2004. Crustal structure across the San Andreas Fault at the SAFOD site from potential field and geologic studies, *Geophys. Res. Lett.*, **31**, doi:10.1029/2003GL019363.

Menke, W., 1989. *Geophysical Data Analysis: Discrete Inverse Theory*, Academic Press, New York, NY, USA.

## References

- Metropolis, N. et al., 1953. Equations of state calculations by fast computational machine, *J. Chem. Phys.*, **21**(6), 1087-1091.
- Michelini, A. & McEvelly, T.V., 1991. Seismological studies at Park- field I: simultaneous inversion for velocity structure and hypocenters using B-splines parameterization, *Bull. seism. Soc. Am.*, **81**, 524– 552.
- Miller, S.A., Collettini, C., Chiaraluce, L., Cocco, M., Barchi, M.R., Kaus, B., 2004. Aftershocks driven by a high pressure CO2 source at depth. *Nature* **27**, 724–727.
- Mirabella, F., M. Ciaccio, M. Barchi, and S. Merlini (2004), The Gubbio normal fault (central Italy): Geometry, displacement distribution and tectonic evolution, *J. Struct. Geol.*, **26**, 2233–2249, doi:10.1016/j.jsg. 2004.06.009.
- Mirabella, F., M. Barchi, and A. Lupattelli (2008), Seismic reflection data in the Umbria-Marche region: Limits and capabilities to unravel the subsurface structure in a seismically active area, *Ann. Geophys.*, **51**(2/3), 383–396.
- Mirabella, F., and Brozzetti, F., Lupattelli, A., and Barchi, M.R., 2011. Tectonic evolution of a low-angle extensional fault system from restored cross-sections in the Northern Apennines (Italy), *Tectonics* **30**, doi:10.1029/2011TC002890.
- Moretti, M., De Gori, P., and Chiarabba, C. Earthquake relocation and three-dimensional Vp and Vp/Vs models along the low angle Alto Tiberina Fault (Central Italy): evidence for fluid overpressure, *Geophys. J. Int.*, **176**, 833-846.
- Mosegaard, K. and Tarantola A., 1995. Monte Carlo sampling of solutions to inverse problems, *J. Geophys. Res.*, **100**(B7), 12-431.
- Mosegaard, K., 2006. *Monte Carlo analysis of inverse problem*, PhD thesis, Copenhagen University.
- Nadeau, R., Foxall, W. and McEvelly, T.V., 1995. Clustering and periodic recurrence of microearthquakes on the San Andreas fault at Parfield, California, *Science* **267**, 503-507.
- Okabe, A., Boots, B., and Sugihara, K., 1992. *Spatial Tessellations: Concept and Applications of Voronoi Diagrams*, John Wiley & Sons, Inc., New York, NY, USA.

- Page, B.M., Thompson, A. and Coleman, R.G., 1998. Late Cenozoic tectonics of the central and southern Coast Ranges of California, *GSA Bulletin* **119** (7), 846-876.
- Pialli, G., Barchi, M. & Minelli, G., 1998. Results of the CROP 03 deep seismic reflection profile, *Mem. Soc. Geol. Ital.*, **52**, 657 pp.
- Piana Agostinetti, N. and Malinverno A., 2010. Receiver function inversion by trans-dimensional Monte Carlo sampling, *Geophys. J. Int.*, **181**(3), 858-872.
- Piccinini, D., et al. (2003), Microseismic study in a low seismicity area of Italy: The Citta' di Castello 2000–2001 experiment, *Ann. Geophys.*, **46** (6), 1315–1324.
- Ponziani, F., De Franco, A, Minelli, G., Biella, G., Federico, C., and Pialli, G., 1995. Crustal shortening and duplication of the Moho in the Northern Apennines: a view from seismic refraction data, *Tectonophysics*, **252**, 391-418.
- Powell, R.E., and Weldon, R.J., 1992, Evolution of the San Andreas fault: *Annual Reviews of Earth and Planetary Science*, **20**, p. 431–468.
- Rosenthal, J.S., 2009. *Optimal proposal distribution and adaptive MCMC*, in MCMC Handbook. Chapman and Hall/CRC Press.
- Roecker, S., C. Thurber, and D. McPhee (2004), Joint inversion of gravity and arrival time data from Parkfield: New constraints on structure and hypocenter locations near the SAFOD drill site, *Geophys. Res. Lett.*, **31**, L12S04, doi:10.1029/2003GL019396.
- Roecker, S., C. Thurber, K. Roberts, and L. Powell (2006), Refining the image of the San Andreas Fault near Parkfield, California using a finite difference travel time computation technique, *Tectonophysics*, **426**, 189 – 205, doi:10.1016/j.tecto.2006.02.026.
- Ross, D.C., 1978, The Salinian block: A Mesozoic granitic orphan in the California coast ranges, in Howell, D.G., and McDougall, K.A, eds., Mesozoic paleogeography of the western United States: Society of Economic Paleontologists and Mineralogists, Pacific Coast Section Symposium, p. 371–380.
- Ross, D.C., 1984. Possible correlations of basement rocks across the San Andreas, San Gregorio-Hosgri, and Rinconada Reliz-King City faults, California, *U.S. Geol. Surv. Paper* 1317, p. 37, U.S. Geological Survey.

## References

Ryberg, T., Hole, J.A., Fuis, G.S., Rymer, M.J., Bleibinhaus, F., Stromeyer, D. and Bauer, K., 2012. Tomographic Vp and Vs structure of the California Central Coast Ranges, in the vicinity of SAFOD, from controlled-source seismic data, *Geophys. J. Int.* **190**, 1341-1360.

Rymer, M.J., Catchings, R.D., and Goldman, M.R., 2003, Structure of the San Andreas fault zone as revealed by surface geologic mapping and high-resolution seismic profiling near Parkfield, California: *Geophysical Research Abstracts* **5**, p. 13523.

Rymer, M.J. et al., 2006. Surface fault slip associated with the 2004 Parkfield, California, earthquake, *Bull. Seism. Soc. Am.*, **96**, 11–27, doi:10.1785/0120050830.

Sambridge, M., Braun, J., and McQueen, H., 1995. Geophysical parameterization and interpolation of irregular data using natural neighbours, *Geophys. J. Int.*, **122**(3), 837-857.

Sambridge, M., and Rawlinson, N., 2005. Seismic tomography with irregular meshes, *Geophys. Monogr.*, **157**, 49-65.

Sani, F., M. Bonini, L. Piccardi, G. Vannucci, D. Delle Donne, M. Benvenuti, G. Moratti, G. Corti, D. Montanari, L. Sedda, and C. Tanini (2009) Late Pliocene – Quaternary evolution of outermost hinterland basins of the Northern Apennines (Italy), and their relevance to active tectonics, *Tectonophysics*, **476**, 336–356, doi: 10.1016/j.tecto.2008.12.012.

Sisson, S., 2005. Transdimensional Markov Chains: a decade of progress and future perspectives, *J. Am. Stat. Assoc.*, **100**, 1077-1090.

Smith, A., 1991. Bayesian computational methods, *Philos. Trans. Phys. Sci. Eng.*, **337**, 369-386.

Solum, J. G. et al. Mineralogical characterization of protolith and fault rocks from the SAFOD main hole. *Geophys. Res. Lett.* **33**, L21314, doi:10.1029/2006GL027285 (2006).

Tarantola, A., and Valette, B., 1982. Inverse problem = quest for information, *J. Geophys.*, **50**(3), 150-170.

- Thayer, M.R., 2006. *Structural geology of the San Andreas fault zone at Middle Mountain, near Parkfield, central California*, MSc thesis, Arizona State University, Tempe, AZ.
- Tavani, S., Storti, F., Salvini, F. and Toscano, C., 2008. Stratigraphic versus structural control on the deformation pattern associated with the evolution of the Mt. Catria anticline, Itali, *J. Struct. Geol.*, **30**, 664-681.
- Trippetta, F., Collettini, C., Vinciguerra, S., and Meredith, P.G., 2010. Laboratory measurements of the physical properties of Triassic Evaporites from Central Italy and correlation with geophysical data, *Tectonophysics*, **492**, 121-132.
- Um, J., and C. H. Thurber (1987), A fast algorithm for two-point seismic ray tracing, *Bull. Seismol. Soc. Am.*, **77**, 972–986.
- Unsworth, M., Bedrosian, P., Eisel, M., Egbert G. and Siripunvaraporn W., 2000. Along strike variations in the electrical structure of the San Andreas Fault at Parkfield, California, *Geophys. Res. Lett.* **27**, 3021-3024.
- Unsworth, M. & Bedrosian, P.A., 2004. Electrical resistivity structure at the SAFOD site from magnetotelluric exploration, *Geophysical Research Letter*, **31**, doi:10.1029 /2003GL019405.
- Takei, Y., 2002. Effect of pore geometry on  $V_p/V_s$ : from equilibrium geometry to crack, *J. Geophys. Res.*, **107**(B2), 2043, doi:10.1029/2001JB000522.
- Toomey, D.R & Foulger, G.R., 1989. Tomographic inversion of local earthquake data from the Hengill-Greindalur Central Volcano Complex, Iceland, *J. Geophys. Res.*, **94**, 17 497–17 510.
- Thurber, C., 1983. Earthquake locations and three-dimensional crustal structure in the Coyote Lake area, central California. *J. Geophys. Res.* **88**, 8226–8236.
- Thurber, C.H., 1993. *Local earthquake tomography: velocities and  $V_p/V_s$ - theory*, in *Seismic Tomography: Theory and Practice*, pp. 563–583, eds Iyer, H. M. & Hirahara, K., Chapman and Hall, London.
- Thurber, C.H., Atré, S.R. & Eberhart-Phillips, D., 1995. Three-dimensional  $V_p$  and  $V_p/V_s$  structure of the Loma Prieta, California, from local earthquake tomography, *Geophys. Res. Lett.*, **22**, 3079–3082.

## References

Thurber, C., S. Roecker, K. Roberts, M. Gold, L. Powell, and K. Rittger (2003), Earthquake locations and three-dimensional fault zone structure along the creeping section of the San Andreas fault near Parkfield, CA: Preparing for SAFOD, *Geophys. Res. Lett.*, **30**(3), 1112, doi:10.1029/2002GL016004.

Thurber, C., S. Roecker, H. Zhang, S. Baher, and W. Ellsworth (2004), Fine-scale structure of the San Andreas fault zone and location of the SAFOD target earthquakes, *Geophys. Res. Lett.*, **31**, L12S02, doi:10.1029/2003GL019398.

Thurber, C., H. Zhang, F. Waldhauser, J. Hardebeck, A. Michael, and D. Eberhart-Phillips (2006), Three-dimensional compressional wavespeed model, earthquake relocations, and focal mechanisms for the Parkfield, California, region, *Bull. Seismol. Soc. Am.*, **96**, S38–S49, doi:10.1785/0120050825.

Titus, S. J., DeMets, C. & Tikoff, B. Thirty-five-year creep rates for the creeping segment of the San Andreas fault and the effects of the 2004 Parkfield earthquake: Constraints from alignment arrays, continuous global positioning system, and creepmeters. *Bull. Seismol. Soc. Am.* **96** (4B), S250–S268 (2006).

Waldhauser, F., Ellsworth, W.L., Schaff, D.P., and Cole, A., 2004. Streaks, multiplets, and holes: High-resolution spatio-temporal behavior of Parkfield seismicity, *USGS Staff – Published Research*. Paper 379.

Wang, X.-Q., Schubnel, A., Fortin, J., David, E.C., Gueguen, Y. and Ge, H.-K., 2012. High  $V_p/V_s$  ratio: Saturated cracks or anisotropy effects?, *Geophys. Res. Lett.* **39**, L11307, doi:10.1029/2012GL051742.

Wernicke, B., 1995. Low-angle normal faults and global seismicity: a review, *J. Geophys. Res.*, **100**, 20 159–20 174.

Williams, C. F., Grubb, F. V. & Galanis, S. P. Jr. Heat flow in the SAFOD pilot hole and implications for the strength of the San Andreas Fault. *Geophys. Res. Lett.* **31**, L15S14, doi:10.1029/2003GL019352 (2004).

Wilkins, R., Simmons, G. and Caruso, L., 1994. The ratio  $V_p/V_s$  as a discriminant of composition for siliceous limestone, *Geophysics*, **49**, 1850-1860.

Vinnik, L.P., Reigber, C., Aleshin, I.M., Kosarev, G.L., Kaban, M.K., Oreshin, S.I. and Roecker, S. W., 2004. Receiver function tomography of the central Tien Shan, *Earth. planet. Sci. Lett.*, **255**(1-2), 131-146.

Zhang, H. and Thurber, C., 2005. Adaptive mesh seismic tomography based on tetrahedral and Voronoi diagrams: application to Parkfield, California, *J.Geophys. Res.*, **110**, B04303, doi:10.1029/2004JB003186.

Zhang, H., Thurber, C. and Bedrosian, P., 2009. Joint inversion for  $V_p$ ,  $V_s$  and  $V_p/V_s$  at SAFOD, Parkfield, California.